STUDIES OF OXYGEN REDUCTION ELECTROCATALYSTS ENHANCED BY DEALLOYING

by

Gary Chih-Kang Liu

Submitted in partial fulfilment of the requirements
for the degree of Doctor of Philosophy

at

Dalhousie University
Halifax, Nova Scotia
August 2011

DALHOUSIE UNIVERSITY

DEPARTMENT OF PHYSICS AND ATMOSPHERIC SCIENCE

The undersigned hereby certify that they have read and recommend to the Faculty of Graduate Studies for acceptance a thesis entitled "STUDIES OF OXYGEN REDUCTION ELECTROCATALYSTS ENHANCED BY DEALLOYING" by Gary Chih-Kang Liu in partial fulfilment of the requirements for the degree of Doctor of Philosophy.

Dated: August 22nd 2011

External Examiner: _____

Research Supervisor: _____

Examining Committee: _____

_____

Departmental Representative: _____

DALHOUSIE UNIVERSITY

DATE: August 22, 2011

AUTHOR: Gary Chih-Kang Liu

TITLE: STUDIES OF OXYGEN REDUCTION ELECTROCATALYSTS ENHANCED BY DEALLOYING

DEPARTMENT OR SCHOOL: Department of Physics and Atmospheric Science

DEGREE: Ph.D. CONVOCATION: October YEAR: 2011

_____

Signature of Author

to Mom and Dad

Table of Content

List of Tables

List of Figures

Abstract

Dealloying refers to the partial, selective dissolution of the less noble component(s) of a binary or ternary alloy precursor, resulting in a noble-rich, porous structure that has high surface area. Such surface structure is beneficial for fuel cells (FC) because FC uses platinum (Pt), a scarce metal, to catalyze the oxygen reduction reaction (ORR) at the cathode surface.

In order to characterize the benefit of the dealloying process in FC ORR catalysts with the rotating disk electrode (RDE) technique, a high surface area catalyst support, namely 3M Co's nanostructured thin film (NSTF), was incorporated into the RDE measurements. NSTF-coated glassy carbon (GC) disks were used in RDE experiments on a $Pt/Pt_{1-x}Ir_x$ ($0.05 < x < 0.3$) composition spread. ORR measurements using NSTF-coated GC disks measure the catalytic properties with the same morphology, composition and surface structure as would be found in a fuel cell.

A series of $Pt_{1-x}Co_x$ and $Pt_{1-x}Ni_x$ ($0.5 < x < 0.8$) dealloy catalyst precursor films were tested using NSTF-coated GC disks in RDE studies. The value of x in $Pt_{1-x}M_x$ (M = Ni, Co) was selected to be high in order to examine the dealloying process. The catalyst films were examined by a RDE test protocol that tracked the surface enhancement factor (SEF) and ORR current densities over a large number of test cycles. The aim was to measure the catalytic performance of the Pt-M materials as dealloying took place. The SEF of the PtCo and PtNi materials increased rapidly at the beginning and reached a plateau as high as 50 cm^2/cm^2 while the specific ORR activities increased as the initial M content in the catalyst precursor increased.

The impact of the dealloying process on morphology was examined by completely dealloying a Pt_3Ni_7 precursor, deposited on mirror-polished GC disks, at a constant potential. As the dealloying process continued, the SEF of the material increased from about 1 cm^2/cm^2 to > 30 cm^2/cm^2 and resulted in the formation of whisker-like structures.

List of Abbreviations Used

CE	counter electrode
DMFC	direct methanol fuel cell
EMP	electron microprobe
FC	fuel cell
HOR	hydrogen oxidation reaction
MEA	membrane electrode assembly
NSTF	nano-structured thin film
OCV	open circuit voltage
ORR	oxygen reduction reaction
PEFC	polymer electrolyte fuel cell
PEMFC	proton exchange membrane fuel cell
RDE	rotating disk electrode
RE	reference electrode
RRDE	rotating ring disk electrode
RTP	rapid thermal processor
SEF	surface enhancement factor
SEM	scanning electron microscope
TEM	transmission electron microscope
WE	working electrode
XRD	X-ray diffraction

Acknowledgements

First of all, this thesis would not have been possible without the amazing guidance of my supervisor, Professor Jeff Dahn. Thank you, thank you for your leadership, support and, in many cases, patience and tolerance. I would also like to thank Dr. David Stevens for his day-to-day technical and scientific support plus, of course, lessons in sarcasm. Other notable Dalhousie Physics Department staff and Dahn lab members who played key roles and made physical contributions to this thesis include Dr. Robbie Sanderson, Dr. Tim Hatchard, Dr. Stephen Payne, Barbara Guvin, Simon Trussler, Stephen Wang, Chris Burns, and Jessie Harlow. Thank you for your fantastic work, discussions, and (sometimes harsh but well-deserved) comments.

On a personal note, several good friends have helped me through the ups and downs in my life in the past years, Gavin Heverly-Coulson, Dr. Arman Bonakdarpour, Jean-Marc Samson, Lauren Hughes, Link and Julia Chen Simpson, Roger and Cheryl Chen Tulsie, Eric and Alexia Stack Hunter. Thank you for being there for me and giving me hopes for a wonderful life after grad school. Thank you.

Last but not least, Mom and Dad, thank you for your decision to bring me and Ted to Canada in 1993 and thank you for all of your tears and sacrifices in the past 32 years that is my life. Thank you.

Chapter 1 Introduction

This chapter provides an introduction to fuel cells, in particular proton exchange membrane fuel cells (PEMFC). A brief overview of PEMFC reaction kinetics and the theoretical framework is also examined.

1.1 Fuel Cells – A Background

A fuel cell (FC) is a device that converts energy stored in chemical bonds of the fuel into electrical energy [1-3]. In general, fuel cells have lower (or zero) greenhouse gas emission than internal combustion engines per electrical energy output and are a candidate for automotive power applications. However, the durability and cost of the materials used in fuel cells, as well as fuel production and storage are some of the major issues hindering the successful commercialization of fuel cells. There are five major categories of fuel cells that have received tremendous research efforts in both the academia and industry [1-3]. They are listed in Table 1-1.

Table 1-1: *Different Types of Fuel Cells.*

FC type	Electrolyte	Operating temperature	Overall reaction	Application
Polymer Electrolyte Membrane FC (PEFC)	Solid polymer (Nafion)	40 ~ 100°C	$H_2 + ½\ O_2 \rightarrow H_2O$ or $CH_3OH + 3/2\ O_2 \rightarrow CO_2 + 2H_2O$ (DMFC)	Portable electronic equipment energy storage, vehicle-sized power source
Alkaline FC	KOH	60 ~ 120°C	$H_2 + ½\ O_2 \rightarrow H_2O$	
Phosphoric Acid FC (PAFC)	H_3PO_4	150 ~ 220°C		
Molten Carbonate FC (MCFC)	Li/K carbonate	600 ~ 700°C		Stationary power generator / back-up power generator
Solid Oxide FC (SOFC)	Metal oxide (ZrO_2)	600 ~ 1000°C		

Polymer Electrolyte fuel cells (PEFC) use a polymer electrolyte membrane (typically Nafion) as the proton conductor and platinum (Pt)-based materials as catalysts. PEFCs are being considered for small vehicle transportation power sources because of their low operating temperature and high power density. The two main types of PEFC are: 1.) The Proton Exchange Membrane Fuel Cell (PEMFC) which uses H_2 gas as fuel and 2.) The Direct Methanol Fuel Cell (DMFC) that uses methanol.

Nearly all major car manufacturers have developed and demonstrated fuel cell vehicles (FCV) such as: GM Hydrogen 1, Ford Demo 11A, DaimlerChrysler NeCar4A, Toyota FCHV, Nissan XTERRA FCV and Honda FCX Clarity… just to name a few [4-7]. The most recent example of a PEMFC-powered vehicle is the FCX Clarity, made by Honda Motors Corporation [8, 9]. The FCX Clarity has a FC stack system that generates 100 kW (135.9 hp) and has similar performance to a standard Honda Civic. The Honda FCX Clarity uses hydrogen gas from an on-board storage tank that stores a maximum amount of 4 kg H_2, compressed at 400 atm. maximum, and is able to travel about 400 km on a full tank [9, 10].

The FCX Clarity is a concept vehicle with limited distribution in Japan and California. World-wide commercialization of PEMFC vehicles, as of 2011, has not yet realized [9, 11, 12]. The main challenge, with factors such as power output, durability, mass-production…etc. under consideration, is cost. Fuel cell cost has been reduced from $275/kW in 2002, $108/kW in 2006, $94/kW in 2007, to $73/kW in 2008 [12-14]. Even

at $73/kW, an 80kW system would cost ~ $6000, more than an internal combustion engine of the same size. In 2009, the cost was further brought down to $61/kW and, by 2010, $45/kW. Figure 1-1 shows some FC system cost break-downs and the U.S. Department of Energy (DOE) benchmarks for the 2010 and 2015 fiscal years [13]. One major part of the fuel cell cost is the membrane electrode assembly (MEA) that consists of a Nafion membrane and catalyst (usually Pt-based) layers [3]. The Pt loading has been reduced in the past decade by high surface area catalyst supports and alloying [15-18] but there is still room for further improvement. Mass commercialization of fuel cell vehicles requires a H_2 distribution network that complements FCV distribution. This is also a current focus of the DOE efforts under the topics of H_2 production, storage and distribution [19].

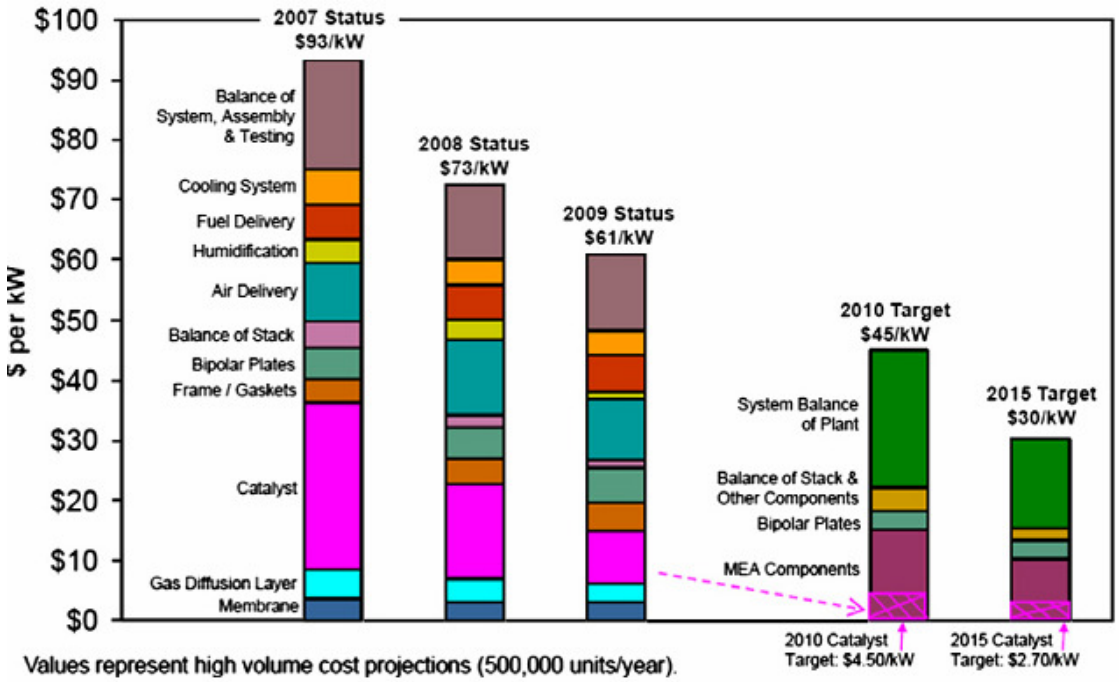

Figure 1-1 Cost break-down of fuel cell systems over the years and the future US DOE cost projections (from [13]).

1.1.1 Fuel Cell System and Stack

Figure 1-2 shows a schematic diagram of a functioning PEMFC system for vehicle applications circa 2006. Most direct hydrogen fuel cell systems share common functionalities and components. The heart of the system is the fuel cell stack, which operates between 60 and 80°C at a pressure from near ambient to over 3 bar (~ 43.5 psig). The 2010 US DOE targets for an integrated fuel cell system operating under these conditions requires the system to generate maximum continuous system output of 50 kW (67.05 hp) with 5,000 hours of service life at a cost of $45/ kW ($2,250 for the 50kW system) [12]. The 2010 US DOE benchmark also restrains FC system size and mass. The same 50 kW system, excluding H_2 storage, also needs to have a system mass less than 80 kg (or 650 W/kg) and be smaller than 80 L (or 650 W/L).

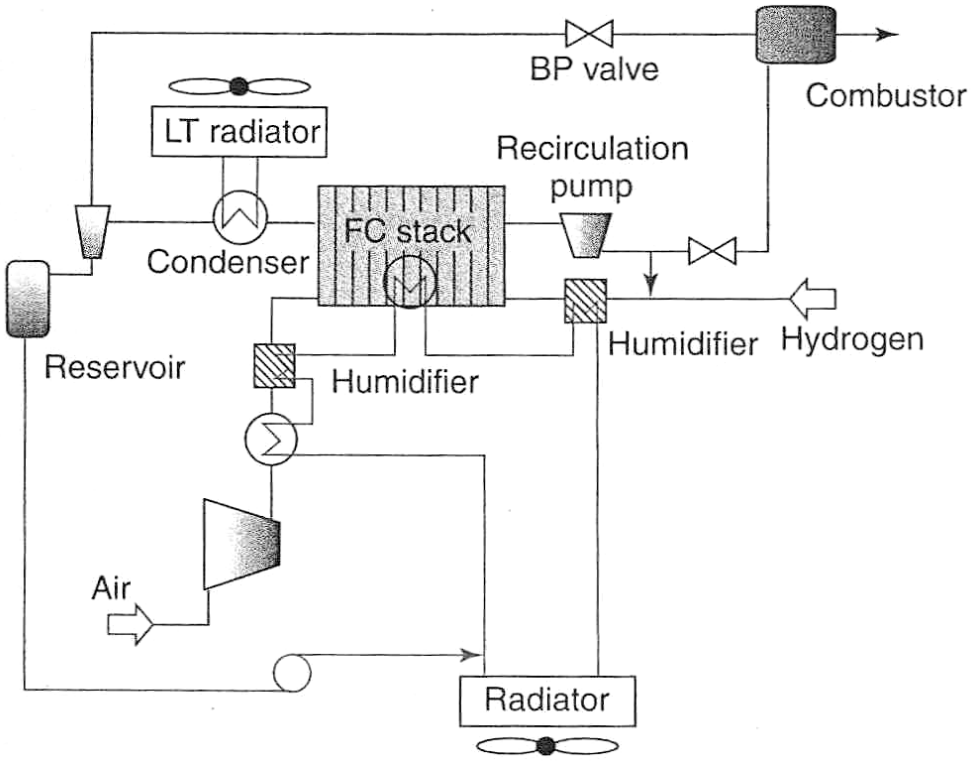

Figure 1-2 Schematic diagram of a functioning PEMFC system (from [3])

As shown in Figure 1-2, the fuel (H_2) is delivered from the source (a tank or an on-board reformer) to the anode. A compressor or a blower delivers oxygen (from air) in excess to the cathode. The H_2 and O_2 gas streams are often externally humidified (by de-ionized water) and temperature pre-conditioned to the optimum PEMFC reaction requirements before entering the stack. In a preferred design, the system can forego an external humidifier and rely on the PEMFC reaction product (H_2O) as the source of membrane humidification. The self-humidification system requires a very thin membrane (> 30 μm) and is currently a focus of DOE 2015 FC research targets [12].

During PEMFC operation, Hydrogen is either re-circulated back into the stack or the stack can be operated 'dead-ended' where there is no continuous exhaust flow. A typical system feeds the air exhaust into a tail-gas combustor, serving as the oxidant. Although a fuel cell system is an efficient means of converting fuel to energy on-board a vehicle, it still produces a considerable amount of waste thermal energy through the electrochemical conversion of hydrogen. The amount of waste thermal energy generated is of the same magnitude as in conventional automotive systems but at lower temperatures [2], therefore the heat exchangers are used for several purposes: to reject waste heat from the FC to ambient temperature; to condition inlet gases to the stack temperature; to assist humidification and condensation of gas streams and, potentially, to enhance energy recovery of the system.

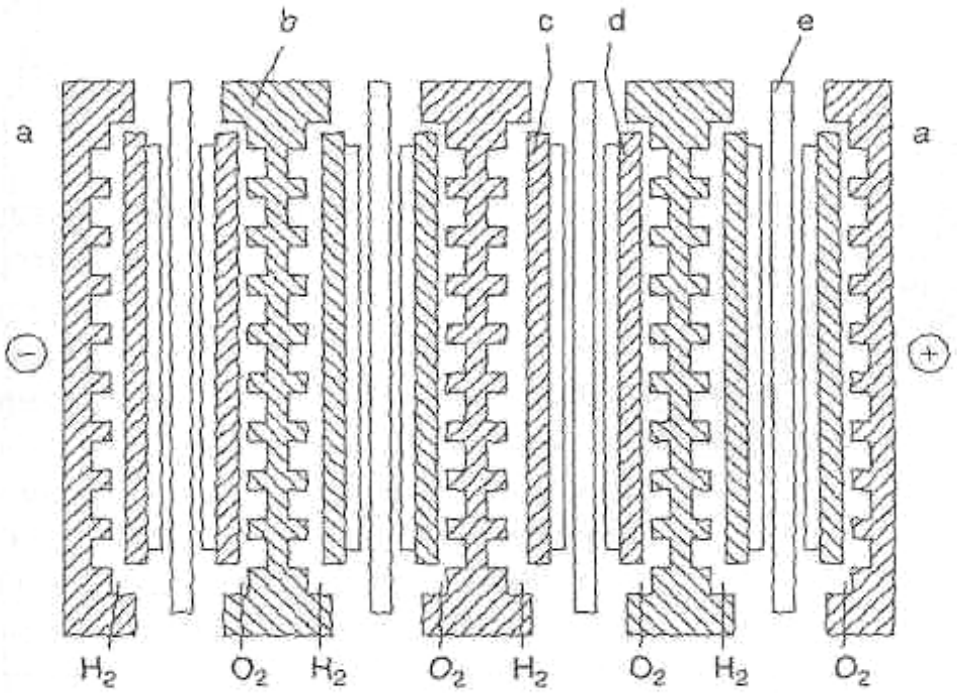

Figure 1-3 Cross sectional view of a bi-polar PEMFC stack with a.) anode flow field b.) cathode flow field c.) anode and GDL d.) cathode and GDL and e.) membrane (from [3]).

Figure 1-3 shows a bi-polar current collector FC stack. The FC stack is the heart of a FC system. The bi-polar current collection design (Figure 1-3) is a logical consequence of the stacking up of many cells in series to obtain a high stack voltage. The industry benchmark for single FC MEA performance is about 1 A/cm^2 at 0.6V. With a typical fuel cell size of 10 cm by 10 cm, a 50 kW stack would include hundreds of single fuel cells stacked in series. Each individual cell is several mm thick. Bi-polar cells are not limited in size because the current flows perpendicular to the electrode surface and current is collected over the whole area of the electrode. A disadvantage of this design is that a single cell failure leads to stack failure. The stack construction depends on the size and output requirement of the system [3].

1.1.2 Proton Exchange Membrane Fuel Cells (PEMFC)

The heart of the PEMFC is a polymer membrane, typically Nafion, which has very low gas permeability. Once hydrated, the Nafion membrane conducts protons and acts as the electrolyte [2]. The electrodes are at the two sides of the membrane. They are typically made out of carbon cloth or another porous material to disperse incoming H_2 and O_2 gases. At each interface between the porous electrodes and the polymer membrane is a layer of catalyst particles, typically Pt-based materials on a high surface area support [3, 20, 21]. Electrochemical reactions occur at the surface of the catalyst at the electrode-membrane interface. The carbon cloth gas dispersion layers (GDL), catalyst layers and the membrane together often are referred to as membrane electrode assembly, or MEA, as shown in Figure 1-4.

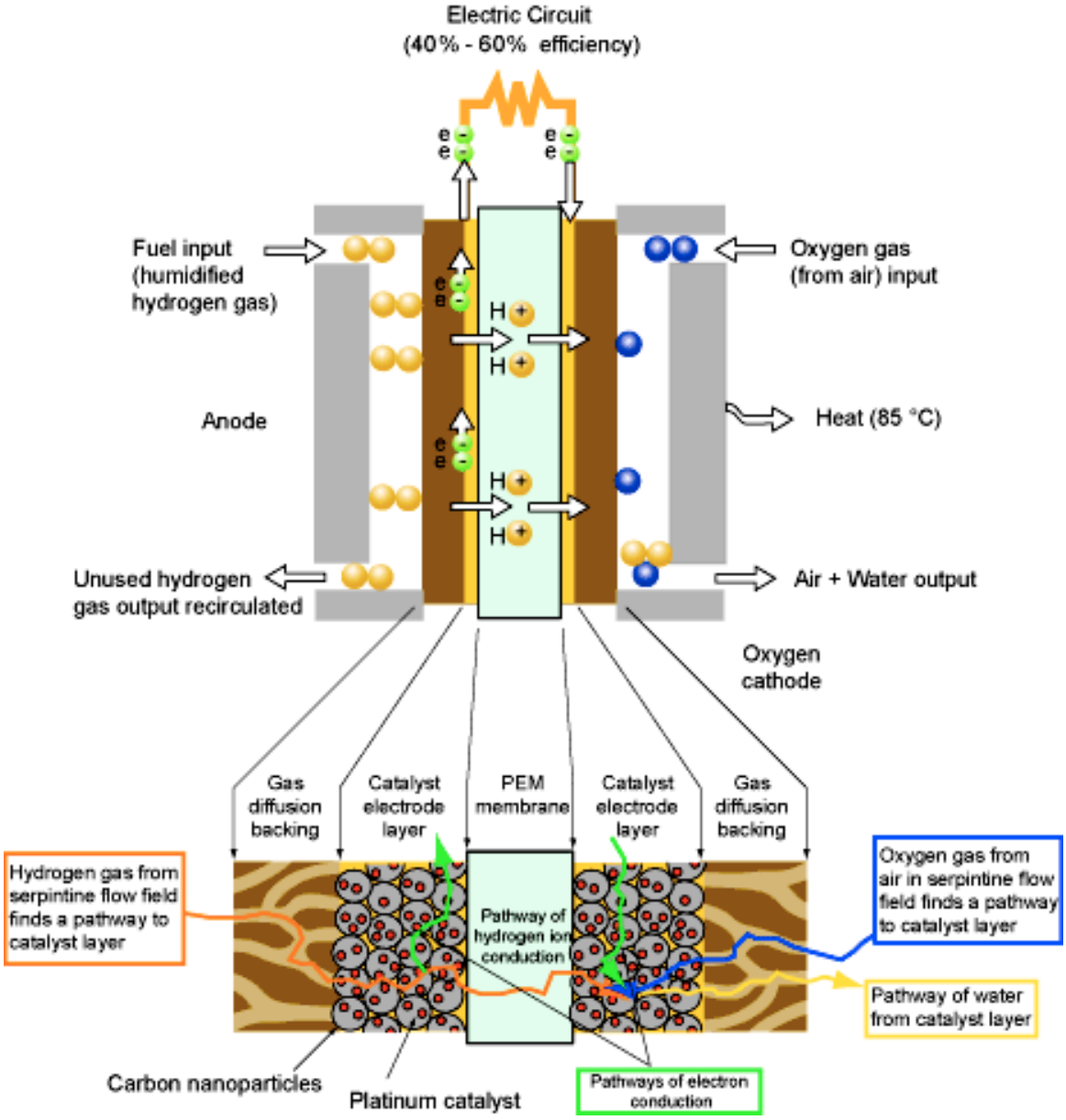

Figure 1-4 Details of a fuel cell MEA (from [13])

Figure 1-4 shows that the anode and cathode electrodes of the cell are fed hydrogen and oxygen (or air), respectively. Hydrogen is oxidized at the anode to provide electrons that power the external load, and the protons are transferred through the membrane to the cathode. The membrane is the electrolyte of the cell, composed of Nafion (sulphonated

fluoroethylene, or perfluorosulphonic acid PFTE copolymer). Oxygen is reduced at the cathode to water or H_2O_2. H_2O_2 is a potentially harmful species to nearby fuel cell components. The overall reaction of the PEMFC is the combustion of hydrogen ($O_2 + 2H_2 \rightarrow H_2O$) and the reaction is thermodynamically spontaneous. However, at FC operating conditions (0 ~ 43.5 psig, < 100°C, humidified), the hydrogen and oxygen gases are kinetically stable and do not react by themselves. The presence of a catalyst at the two electrodes provides alternative thermodynamic pathways for the reactions to proceed (lower activation energy).

1.2 Basic PEMFC Electrochemistry

This section explains some of the basic electrochemical concepts in fuel cell operations. The material and examples shown below are taken primarily from *Fuel Cell Systems Explained* [2], *Fuel Cell Fundamentals* [1] and sections in *The Handbook of Fuel Cells* [3].

1.2.1 Free Energy, Equilibrium Potential and Thermodynamic Factors

The electrochemical reactions in the fuel cell happen simultaneously on both sides of the membrane. The basic fuel cell reactions are:

Anode:	$H_2 \rightarrow 2H^+ + 2e^-$	(Eqn. 1-1)
Cathode:	$½\ O_2 + 2H^+ + 2e^- \rightarrow H_2O$	(Eqn. 1-2)
Overall:	$H_2 + ½\ O_2 \rightarrow H_2O$	(Eqn. 1-3)

The FC electrochemical reactions shown above require the transfer of charge (electrons transferred from anode to cathode) to chemical species through the electrodes and the external load (shown in Figure 1-4). This distinguishes electrochemical reactions (Eqns. 1-1 and 1-2) from chemical reactions (i.e. Eqn. 1-3 by itself). In chemical reactions, charge transfer occurs directly between chemical species without the liberation of free electrons.

The theoretical maximum electrical energy output, $W_{electrochem}$, in a fuel cell corresponds to the Gibbs free energy change, ΔG, of Eqn. 1-3,

$$W_{electrochem} = -\Delta G = -237\,{}^{kJ}\!/_{mol} \qquad \text{(Eqn. 1-4)}$$

The theoretical potential of the fuel cell, E, is:

$$E^0 = \frac{-\Delta G}{nF}, \qquad \text{(Eqn. 1-5)}$$

where n is the number of electrons involved in the reaction shown in Eqn. 1-3 (n = 2) and F is Faraday's constant (F = 96485 coulombs/electron-mol). The theoretical hydrogen/oxygen fuel cell potential, E^0, can be calculated:

$$E^0 = \frac{-\Delta G}{nF} = -\frac{-\left(237\,{}^{kJ}\!/_{mol}\right)}{(2)(96485\,{}^{C}\!/_{mol})} = 1.23\ V\ . \qquad \text{(Eqn. 1-6)}$$

Therefore, the cell's equilibrium potential under ambient conditions (1 atm., 25 °C) is 1.23 V, also known as open circuit voltage (OCV). The equilibrium potential of the reaction depends on the product / reactant concentrations (expressed as partial pressures in the case of the hydrogen-oxygen PEMFC) via the Nerst Equation:

$$E = E^0 + \frac{RT}{nF} \ln \left(\frac{P_{H_2} \times P_{O_2}^{\frac{1}{2}}}{P_{H_2O}} \right) \qquad \text{(Eqn. 1-7)}$$

The theoretical OCV of a hydrogen fuel cell, i.e. 1.23 V at 25 °C, is not measured in a fuel cell. This is because adsorbed species on the electrode surface hinders catalyst function and cause corrosion of the Pt catalysts. A different experimental setup other than a fuel cell MEA is required to observe the equilibrium potential of the oxygen reduction reaction. Larminie and Dicks [2] provide the expressions for enthalpy and entropy of H_2, O_2 and water at different temperatures and show how they impact the fuel cell OCV and theoretical maximum efficiency, ε_{thermo}. They show that

$$\varepsilon_{thermo} = \frac{Energy_{useful}}{Energy_{total}} = \frac{\Delta G}{\Delta H}, \qquad \text{(Eqn. 1-8)}$$

where ΔH is change in enthalpy of the reaction. Some results are listed in Table 1-2 below. The values are derived from the OCV, where the FC cell is in a state of equilibrium, with no current delivered.

Table 1-2 *ΔG, OCV_{max} and Efficiency of Fuel Cell at Different Temperature*

Water	Temp (°C)	ΔG (kJ/mol)	OCV (V)	Max. efficiency
Liquid	25	-237.2	1.23	83%
Liquid	80	-228.2	1.18	80%
Gas	100	-225.3	1.17	79%
Gas	200	-220.4	1.14	77%
Gas	400	-210.3	1.09	74%
Gas	600	-199.6	1.04	70%
Gas	1000	-177.4	0.92	62%

(Adapted from [2])

Figure 1-5 shows a comparison between hydrogen-oxygen FC efficiency and that of an ideal heat engine (Carnot cycle) as functions of reactant temperature [2]. The efficiency of the Carnot cycles were calculated using a rejection temperature of 50 °C. The FC efficiency was calculated using Eqn. 1-8 with reaction products (H_2O) having the same temperature as the reactants. The FC holds a significant thermodynamic efficiency advantage at low temperature but loses this advantage at higher temperatures.

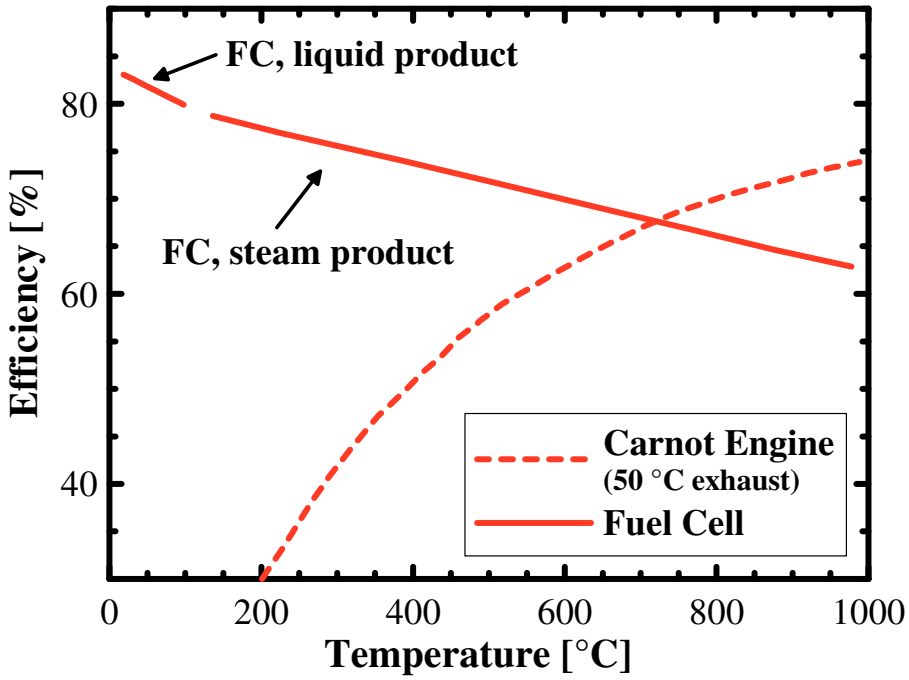

Figure 1-5 Theoretical FC efficiency as a function of reactant temperature compared to that of an ideal heat engine (Carnot cycle, with rejection temperature of 50 °C). The break in the FC efficiency curve at 100 °C arises from the entropy difference between liquid and gaseous water (from [2])

The real efficiency of a fuel cell must always be less than the thermodynamic efficiency shown in Figure 1-5. Two major factors that have negative impact on the FC efficiency

are 1) Voltage loss and 2) Fuel utilization loss. So the real FC efficiency ε_{real}, may be written as [1]:

$$\varepsilon_{real} = \varepsilon_{thermo} \times \varepsilon_{voltage} \times \varepsilon_{fuel}\,, \qquad \text{(Eqn. 1-9)}$$

where $\varepsilon_{voltage}$ is the voltage efficiency of the fuel cell and ε_{fuel} is the fuel utilization efficiency. The voltage efficiency is the ratio of the operating voltage ($V_{operating}$) to the thermodynamically reversible voltage of the fuel cell (E):

$$\varepsilon_{voltage} = \frac{V_{operating}}{E}\,. \qquad \text{(Eqn. 1-10)}$$

The operating voltage of the fuel cell depends on the current drawn from the fuel cell, as given by the *i*-vs.-V curve (also known as the polarization curve) that will be discussed in later sections. The fuel utilization efficiency, ε_{fuel}, accounts for the fact that not all of the fuel provided to a fuel cell will participate in the designated reaction (Eqn. 1-3). Some of the fuel may undergo side reactions and create H_2O_2, other portions may simply flow through without ever reacting. The fuel utilization efficiency, then, is the ratio of fuel used by the cell to generate electric current, versus the total fuel provided. During FC operation, the fuel (H_2 and O_2 gas) is pumped into the fuel cell at a flux v_{fuel} (in mol/sec) and electrical current, i (in Ampere), is generated. The fuel utilization efficiency, ε_{fuel}, is defined as:

$$\varepsilon_{fuel} = \frac{i \diagup nF}{v_{fuel}}\,, \qquad \text{(Eqn. 1-11)}$$

Combining Eqns 1-9, 1-10 and 1-11, the real efficiency of an operating fuel cell, is then:

$$\varepsilon_{real} = \left(\frac{\Delta G}{\Delta H}\right) \times \left(\frac{V_{operating}}{E}\right) \times \left(\frac{i \diagup nF}{v_{fuel}}\right). \qquad \text{(Eqn. 1-12)}$$

1.2.2 An Overview on Fuel Cell Reaction Kinetics and Electrocatalysis

The previous section showed that the total change in the Gibb's free energy of the PEMFC reaction, $H_2 + O_2 \rightarrow H_2O$ is negative, meaning energy is released and the reaction is thermodynamically spontaneous. However, the reaction is said to be ***kinetically-activated***, that is, it does not occur spontaneously fast enough. In other words, a mixture of hydrogen and oxygen gases at ambient condition (20 °C, 1 atm.) is stable and will not spontaneously combust. The presence of catalyst layers at the two electrodes provides alternative paths (lower activation energy) for the reactions to proceed. This section briefly explains the concept of "activation energy barrier" and the role of catalysts, which leads to the notions of "overpotential" and "activation loss" in the fuel cell polarization curve and to the Butler-Volmer (B-V) relation. In the end, a simpler form of B-V analysis, namely the Tafel equation, is introduced.

1.2.2.1 Activation Energy Barriers, Catalysis and Finite Reaction Rate

It is apparent that an electrochemical reaction, or any chemical reaction, proceeds at a limited rate in a given environment (temperature, pressure…etc.) and with a fixed rate of reactant supply / product removal. Reaction rates are finite even if the reactions are "energetically downhill" (release energy). This is because an energy barrier (shown in Figure 1-6), or "activation energy", normally impedes the conversion of reactants into products. The probability that the reactant species can make it over the barrier at a given average energetic level determines the reaction rate. A higher activation energy barrier likely results in a slower reaction rate.

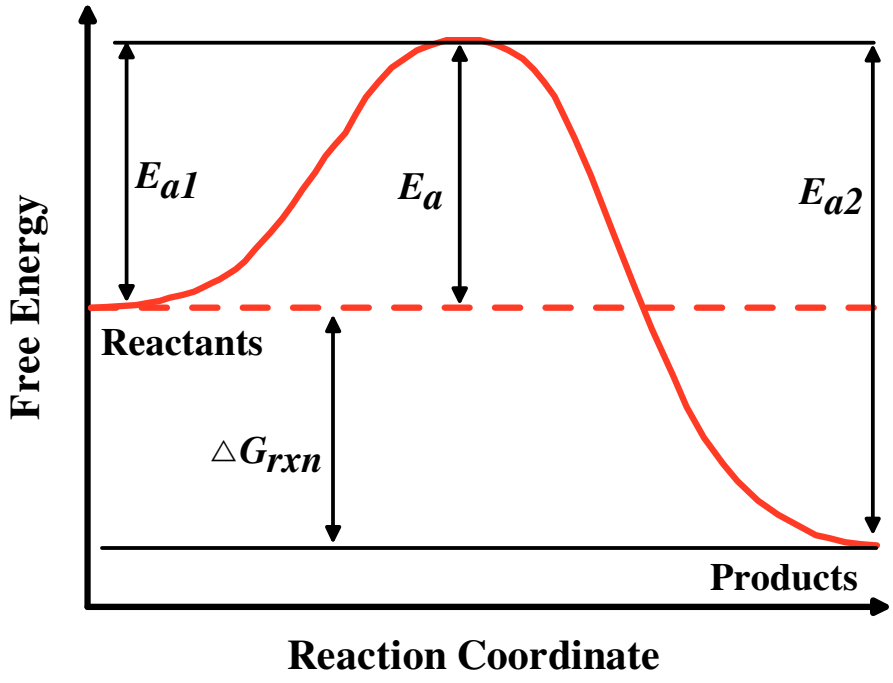

Figure 1-6 An activation barrier (E_a) impedes the conversion of reactants to products. E_{a1} is the forward activation barrier while E_{a2} is the reverse activation energy barrier

A suitable example to further understand the concept of activation energy is the hydrogen oxidation reaction (HOR, $H_{2(g)} \rightarrow 2H^+ + 2e^-$) at the electrolyte-metal electrode interface (from [1]). The reaction occurs by a series of basic steps:

1) Transport of $H_{2(g)}$ to the metal electrode (deliver reactant).
2) Adsorption of H_2 on the metal electrode surface
3) Separation of the H_2 molecule into chemisorbed hydrogen atoms on the electrode surface,
4) Transfer of an electron from chemisorbed hydrogen atoms to the electrode, releasing H^+ ions into the electrolyte.
5) Transport of H^+ ions away (remove product).

The overall reaction rate is limited by the slowest step in the series, which is step #4 in this example:

$$Etd(M)-H \rightarrow (Etd(M)+e^{-})+H^{+} \qquad \text{(Eqn. 1-13)}$$

Where "*Etd(M)–H*" represents a hydrogen atom chemisorbed on the metal electrode surface, "*(Etd(M) + e⁻)*" represents a liberated electrode surface site and a free electron passed into the electrode. Figure 1-7a shows a pictorial representation of Eqn. 1-13 while Figure 1-7b shows the energy levels of Eqn. 1-13 as a function of distance from the electrode surface. The axes in Figure 1-7b were drawn with arbitrary scale.

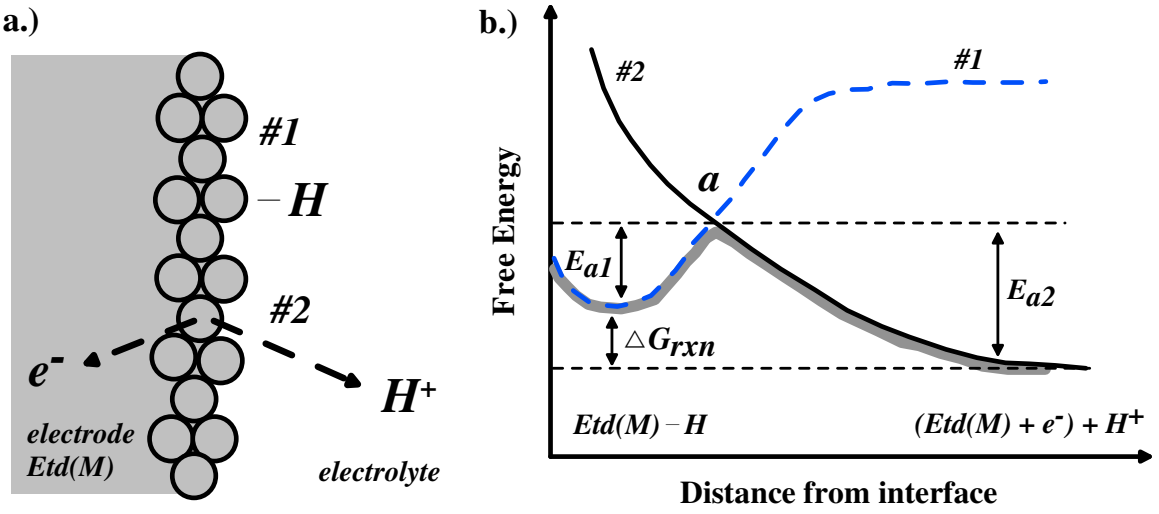

Figure 1-7 A schematic of the chemisorbed hydrogen charge transfer reaction is shown in (a). The chemisorbed hydrogen atom is shown as #1 while the charge transfer reaction is shown as #2. The free energy diagram of the reaction is shown in (b). E_{a1} is the forward activation barrier while E_{a2} is the reverse activation energy barrier (from [1]).

Curve #1 in Figure 1-7b shows the free energy level of atomic hydrogen, H, which increases with distance from electrode surface. This is because the stability of atomic

hydrogen (reactant) improves with chemisorption to the metal electrode surface. Curve #2 shows the free energy of an H^+ ion (product) in the electrolyte. The free energy of the H^+ ion increases as it is brought near the electrode surface due to repulsive forces from other adsorbed species. The thick gray solid line in Figure 1-7b shows the lowest energy path for the conversion of chemisorbed hydrogen to H^+. It is apparent that the minimum energy path of the reaction requires overcoming a peak, or an activation barrier. Conceptually, this means that the reactant is first converted into an ***activated state***, at the peak of the energy diagram (at the point marked "a"), before it can be converted into products. A catalyst, in terms of energy diagram described here, provides an alternative path that has a lower activation energy barrier than the uncatalyzed reaction (shown in Figure 1-8). Unlike reactants, a catalyst may participate in multiple steps in the reaction but is not consumed.

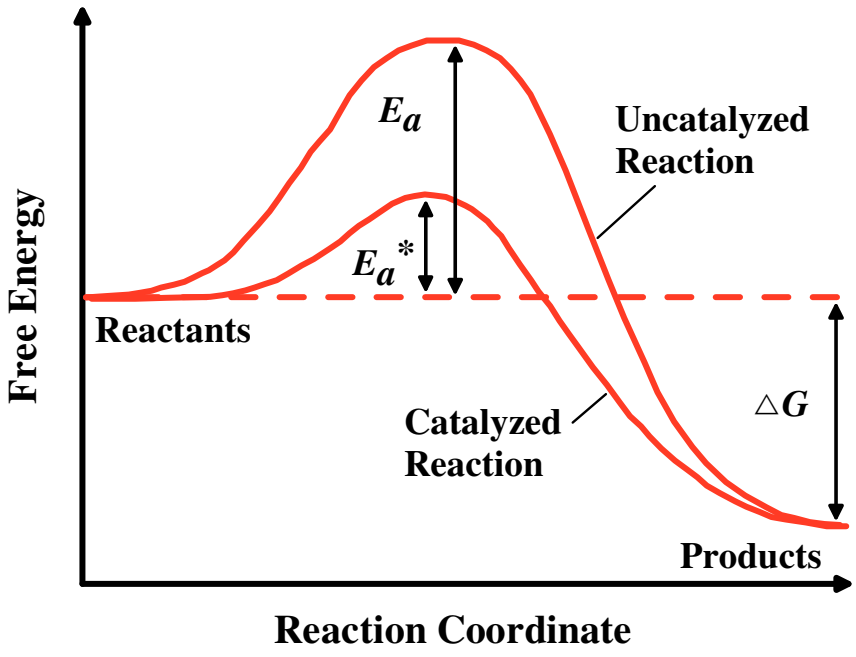

Figure 1-8 A catalyzed reaction has lower activation energy barrier (E_a^*).

During the reaction, the reactant is transformed into an activated state in order to undergo the transition to form the product. The conversion rate of reactants to products depends on the probability that a reactant will undergo activation. While it is beyond the scope of this thesis to motivate theoretical derivations, statistical mechanics arguments indicated that the probability of finding a species in the activated state is exponentially dependent on the activation barrier:

$$p = \exp\left(\frac{-E_a}{RT}\right), \qquad \text{(Eqn. 1-14)}$$

where p is the probability of finding a reactant species in the activated state, E_a is the energy barrier between the reactant and the activated state, R is the gas constant and T is the temperature (K). The reaction rate, r, is then written as the product of the probability p, the reactant concentration, c, and the reaction attempt frequency, f (also known as "frequency factor" or "decay rate product" [1]). The rate of forward reaction (subscript "1") is then:

$$r_1 = c \times f \times p = c_1 f_1 \exp\left(\frac{-E_{a1}}{RT}\right), \qquad \text{(Eqn. 1-15)}$$

where r_1 is the reaction rate (mol/sec/cm^2) in the forward direction, ($H_{2(g)ads} \rightarrow 2H^+ + 2e^-$, for an example), c_1 is the reactant surface concentration ([H_{ads}], in mol/cm^2) and f_1 is the frequency (Hz) associated with the reaction[1].

When evaluating the overall rate of a reaction, both the forward ($H_{2(g)ads} \rightarrow 2H^+ + 2e^-$) and reverse ($2e^- + 2H^+ \rightarrow H_{2(g)ads}$) directions of the reaction must be considered. With corresponding forward (r_1) and reverse (r_2) rates, the net reaction rate, r_{net}, is defined as:

$$r_{net} = r_1 - r_2 \qquad \text{(Eqn. 1-16)}$$

The reaction rate, r, expressed above, has unit of mol/sec/cm^2. For fuel cells, the measurement unit is typically the current density, j, with units of Ampere/cm^2. The conversion from reaction rate to current density is:

$$j = nFr \qquad \text{(Eqn. 1-17)}$$

where n is the number of electrons involved ($n = 2$). Combining Eqns. 1-15, 1-16 and 1-17, the overall current density of the reaction can be written as:

$$j_{net} = nF\left[c_1 f_1 \exp\left(\frac{-E_{a1}}{RT}\right) - c_2 f_2 \exp\left(\frac{-E_{a2}}{RT}\right)\right], \qquad \text{(Eqn. 1-18)}$$

where subscripts "1" and "2" denote the forward and reverse reactions, respectively. Eqn. 1-18 states that the net current of a reaction is given by the difference between the forward and reverse reaction rates, which are exponentially dependent on the activation barriers E_{a1} and E_{a2}.

1.2.2.2 Equilibrium, Overpotential and the Butler-Volmer Equation

The rates for the forward and reverse reactions may not be equal. For the $H_{2(g)ads} \rightarrow 2H^+ + 2e^-$ example discussed earlier in Figure 1-7 and Eqn. 1-18, the forward reaction has a smaller activation barrier and will proceed at a faster rate. However, at thermodynamic equilibrium, the forward and reverse current densities must balance so the net current density is zero. The current density at equilibrium is also known as the exchange current density, j_0. O'Hayre and Cha [1] provide a useful depiction of the equilibrium condition, the exchange current density and the Galvani potential (equilibrium potential), shown in Figure 1-9.

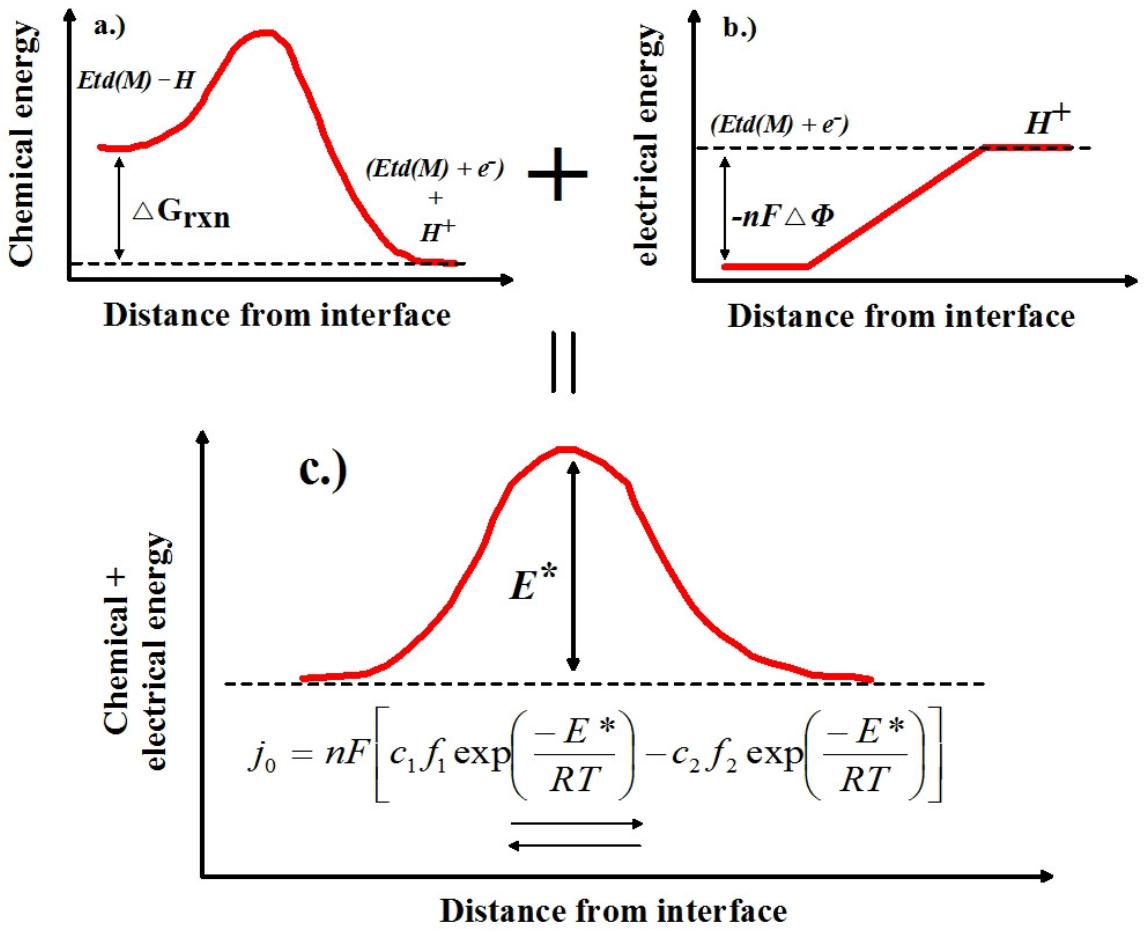

Figure 1-9 At equilibrium, the chemical free-energy difference across a reaction interface (a) is balanced by an electrical potential difference (b), resulting in a zero net reaction rate (c). (from [1])

Using the HOR example, Figure 1-9a shows the free-energy of the chemisorbed hydrogen (M---H) is higher than the product state (H^+). The unequal activation barrier between the forward and reverse reaction results in a net forward reaction as discussed earlier. However, the net forward reaction creates a build-up of electrons in the electrode and equal amount of H^+ ions accumulation in the electrolyte. The separation of charges creates a potential difference ($\Delta\Phi$) across the reaction interface, shown in Figure 1-9b. The separation of charges and ions continues until the resultant potential difference

counterbalances the chemical free-energy difference between the reactants and products. The combined effect of the chemical and electrical potentials is shown in Figure 1-9c. The balance results in an equal activation barrier ($\boldsymbol{E}^*$) for the forward and reverse reactions, leading to identical forward and reverses rates (Eqn. 1-15), and the system is in equilibrium. The equilibrium current density, j_0, is then defined as:

$$j_0 = nF\left[c_1 f_1 \exp\left(\frac{-E^*}{RT}\right) - c_2 f_2 \exp\left(\frac{-E^*}{RT}\right)\right]. \qquad \text{(Eqn. 1-19)}$$

The equilibrium condition described above results in a measurable potential difference across the electrode-electrolyte interface. The potential difference is caused by separation and accumulation of charges (in electrode) and H^+ ions (in electrolyte) across the interface. In other words, at the equilibrium condition described above, a potential difference is created because charges and ions accumulate at opposite sides of the interface. The electrons are not transferred to an external load and the ions are not consumed in further reactions. This concept can be applied to a full electrochemical cell with zero net electrical current flow (open circuit). The anode and cathode each have unequal chemical free energy between the reactant and product states (as in Figure 1-9a). The unequal free energy at each electrode results in a net forward reaction that leads to a potential difference (as in Figure 1-9b). The measurable potential difference across the positive and the negative electrodes of an electrochemical cell under the equilibrium conditions described above is known as the ***Galvani potential***, or Open Circuit Voltage (OCV) mentioned earlier.

At equilibrium, the potential of an electrochemical cell remains at OCV and no current flows through the external circuit. The cell potential can be changed by an external

potential / current source (a potentiostat) or by applying an electrical "load" (current flow). For an example, an "electrical short", or an extremely high load, is a direct electrical connection (zero resistance) between the positive and the negative electrode that allows up to an infinite amount of electrical current. During an "electrical short" between two electrodes, the electrical potential across the electrodes is zero.

A change in cell voltage can affect the magnitude of activation barrier. By biasing the system to favour the forward reaction, some of the thermodynamically available cell potential is lost and a net positive electric current can be drawn from the electrochemical cell. This concept is illustrated in Figure 1-10. The free-energy for the forward and reverse reactions, shown in Figure 1-10a, does not change (compare with Figure 1-9a) and the unequal activation barrier favours the forward reaction. Figure 1-10b shows the electrical potential is decreased by η due to an external bias. The change in electrical potential upsets the balance between the forward and reverse activation barriers, shown in Figure 1-10c. A decrease in the potential by η reduces the forward activation barrier by $\alpha nF\eta$ and increases the reverse activation barrier by $(1 - \alpha)nF\eta$. The value of α depends on the symmetry of the activation barrier. α is known as the transfer coefficient ($0 < \alpha < 1$). A reaction with $\alpha = 0.5$ is said to be "symmetric". The deviation of the cell potential due to the external bias, η, is known as the ***overpotential***. It is a term used by electrochemists and is often mistaken as a "higher potential". In fact, the term ***overpotential*** describes a "potential difference", as a result of an external load or an applied potential (via a potentiostat), "over" the reversible (equilibrium) voltage level, E°.

For an example: an electrochemical system with E° = 1.20 V_{RHE} that is held at 0.8 V_{RHE} via an external source (a potentiostat or a load) can be described as "η = - 0.4 V".

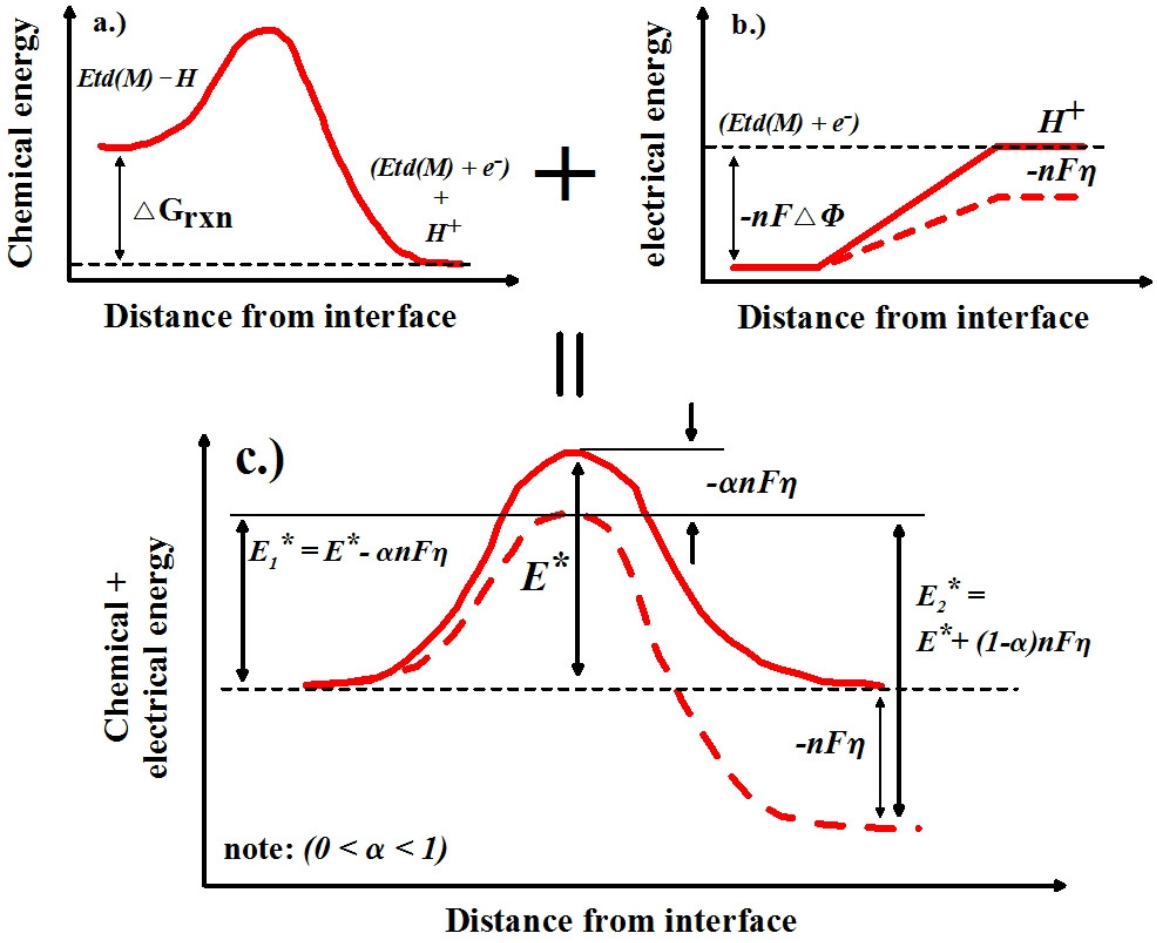

Figure 1-10 With an external bias, η, the forward reaction is favoured over the reverse reaction. The chemical energy (a) of the reaction is the same as before. The external bias changes the electrical potential (b) and upsets the balance between the forward and reverse activation energy barriers (c). (from [1])

Theoretically, overpotential is the potential applied to the electrode-electrolyte interface to direct the net reaction away from equilibrium. The term "overpotential" is sometimes confusing because it tends to imply an "increase" in the cell voltage, whereas in an electrochemical cell (a cell that produces useful electrical work) the overpotential reduces

the cell potential from the reversible voltage to a lower value. In an electrolytic cell, a positive overpotential is applied to the cell in order to reverse the electrochemical reaction. In other words, the potential of an electrolytic cell is kept at a higher value than the reversible level in order to "drive the cell in reverse". Examples of electrochemical cells include the electrolysis of water and the charging of a rechargeable battery.

As discussed earlier, at equilibrium (Figure 1-9), current densities for the forward and reverse reactions are both given by j_0. With an overpotential, the system moves away from equilibrium (Figure 1-10) and produces a measureable net current. The net current of an electrochemical cell is the sum of the forward and reverse current density (as in the style of Eqn. 1-18), written as a function of j_0 (Eqn. 1-19), and taking into account the changes in the activation energy barriers:

$$j_{net} = j_0\left[\exp\left(\frac{\alpha n F \eta}{RT}\right) - \exp\left(\frac{-(1-\alpha) n F \eta}{RT}\right)\right]. \qquad \text{(Eqn. 1-20)}$$

This equation is known as the ***Butler-Volmer Equation*** (B-V Eqn.), developed by John Alfred Valentine Butler (1899 ~ 1977), a British physical chemist, and Max Volmer (1885 ~ 1965), a German surface chemist. The B-V Eqn. is considered the cornerstone of electrochemical kinetics. It is used as the foundation for the relationship between current and voltage in most electrochemical systems. The B-V Eqn. states that the current produced by an electrochemical reaction, within the reaction kinetics limit, increases exponentially as a function of the overpotential, η.

1.2.2.3 Simplified FC Kinetics: Tafel Equation and Tafel-style analysis

When dealing with fuel cell reaction kinetics, B-V Eqn. is often unnecessarily complicated because a fuel cell typically operates at a potential far away from equilibrium. As stated in earlier sections, the industry benchmark for a single FC MEA performance is 1 A/cm^2 at 0.6 V. This is ~ 600 mV away from the FC equilibrium potential. Typically, when $\eta > 50$ mV at room temperature, the second exponential term in the B-V Eqn. becomes negligible. In other words, the forward-direction reaction dominates, akin to an *irreversible* process, thus the B-V Eqn. can be simplified to:

$$j_{net} = j_0 \exp\left(\frac{\alpha n F \eta}{RT}\right). \qquad \text{(Eqn. 1-21)}$$

Solving this equation for the overpotential, η, yields:

$$\eta = \frac{-RT}{\alpha n F}\ln(j_0) + \frac{RT}{\alpha n F}\ln(j_{net}). \qquad \text{(Eqn. 1-22)}$$

Since the transfer coefficient, α, and the exchange current density, j_0, are both constant for a given reaction, Eqn. 1-21 can be further simplified into:

$$\eta = a + b\ln(j_{net}) \qquad \text{(Eqn. 1-23)}$$

This is known as the ***Tafel Equation***, developed by Julius Tafel (1862 ~ 1918), a Swiss chemist. The Tafel Equation allows the exchange current density (j_0) and the transfer coefficient (α) to be determined by experiments via plotting the cell potential as a function of current density in a semi-log graph. This is known as ***Tafel-style analysis*** and such graph is referred to as a ***"Tafel-plot"*** throughout this thesis. Also, it is interesting to note that the Tafel equation predates the B-V Eqn. because it was first developed as an empirical law based on electrochemical observations! Figure 1-11 shows an example of Tafel-style analysis.

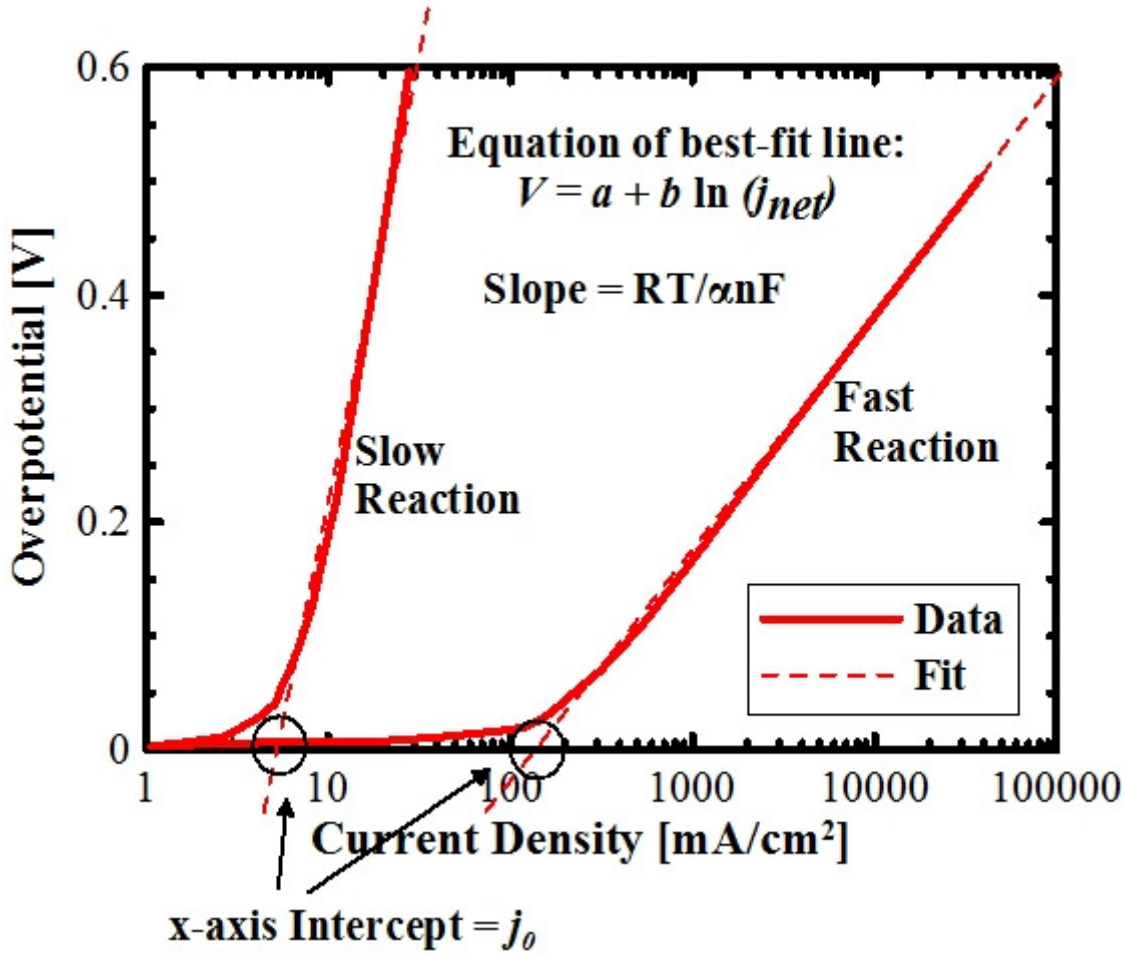

Figure 1-11 Tafel plots for slow and fast electrochemical reactions are used to determine j_0 and α. (from [1])

The B-V Eqn. and its simplified form, the Tafel Equation, indicate a "delay in potential" in the onset of a reaction from its equilibrium potential. In other words, in order to extract electrical energy from the cell, certain amount of potential is "sacrificed" from the equilibrium potential. This is known as ***activation loss***. It is one of the irreversible loss mechanisms in fuel cells and will be discussed in detail next.

1.3 An Overview on Irreversible Losses in Fuel Cell Reactions

The potential of a fuel cell decreases when current is drawn and the amount of potential loss depends on the current. In general there are three or four types of losses associated with fuel cell operation. Figure 1-12 shows a typical potential versus current density graph, also known as a ***polarization graph*** of a typical fuel cell highlighting different types of losses.

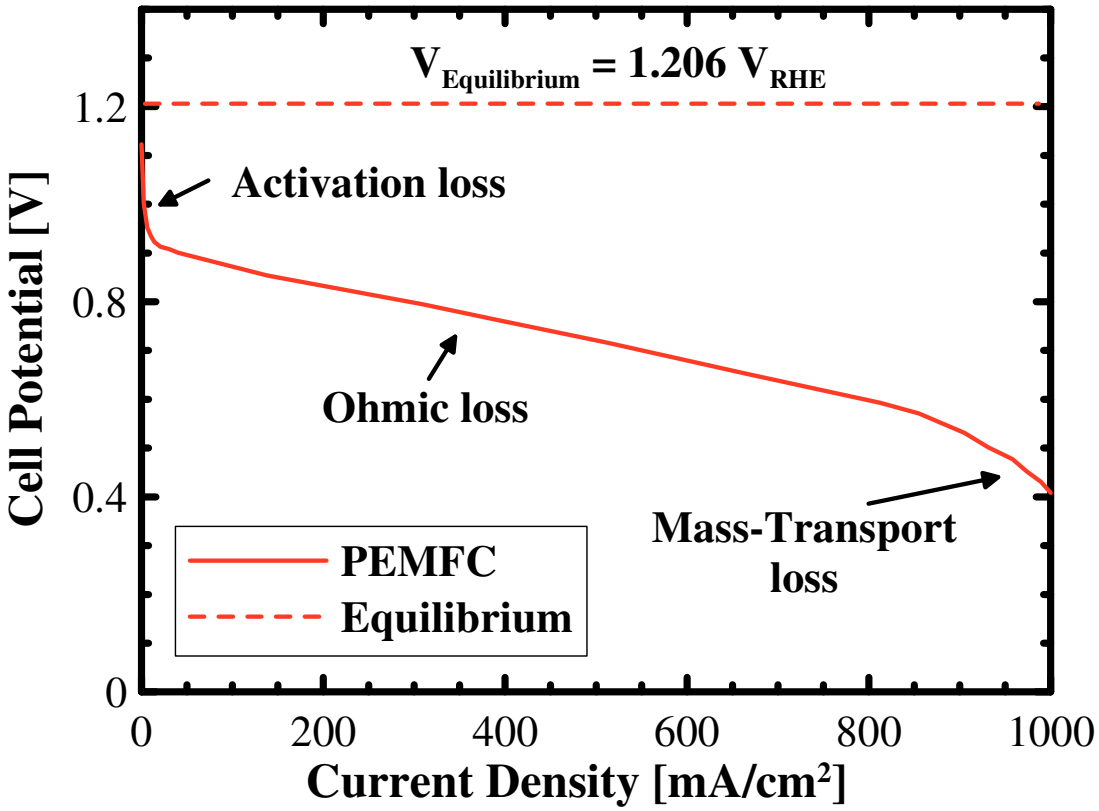

Figure 1-12 A typical PEMFC polarization curve shows three major types of irreversible loss mechanisms: activation, ohmic and mass-transport (from [2]).

The irreversible potential losses from the FC reaction equilibrium potential are identified in the following format:

$$V_{cell} = E^0 - \eta^{Activation} - \eta^{Ohmic} - \eta^{Mass-Transport} \qquad \text{(Eqn. 1-24)}$$

1.3.1 Activation Loss

As discussed earlier, the activation loss is caused by the slowness of the reaction taking place on the surface of the electrodes due to activation energy barriers of the reactions. In the FC reaction, a certain amount of overpotential, or potential beyond the equilibrium level, is sacrificed to drive the chemical reaction that transfers the electron to/from the electrode. The activation loss is described by the Tafel Equation (Eqns. 1-22 and 1-23):

$$\eta^{Activation} = A \ln\left(\frac{j_{net}}{j_0}\right) \qquad \text{(Eqn. 1-25)}$$

Activation loss contributes significantly to the overall output power loss of a FC because it shifts the entire polarization curve to a lower potential. In a fuel cell catalysis reaction, different catalysts have different exchange current densities. For an example, Table 1-3 shows several exchange current densities for catalyzing $H_2 \rightarrow 2H^+ + 2e^-$ at the surface:

Table 1-3 *j_0 for Surface Hydrogen Oxidation/Reduction in Acidic Electrolyte*

Metal	j_0 [A/cm^2]
Pb	2.5E-13
Zn	3E-11
Pt	5E-4
Ni	6E-6
Pd	4E-3

The impact of j_0 on a polarization curve is shown in Figure 1-13. It is apparent that increasing the exchange current density lowers the activation losses because activation loss is the primary potential loss at low current density.

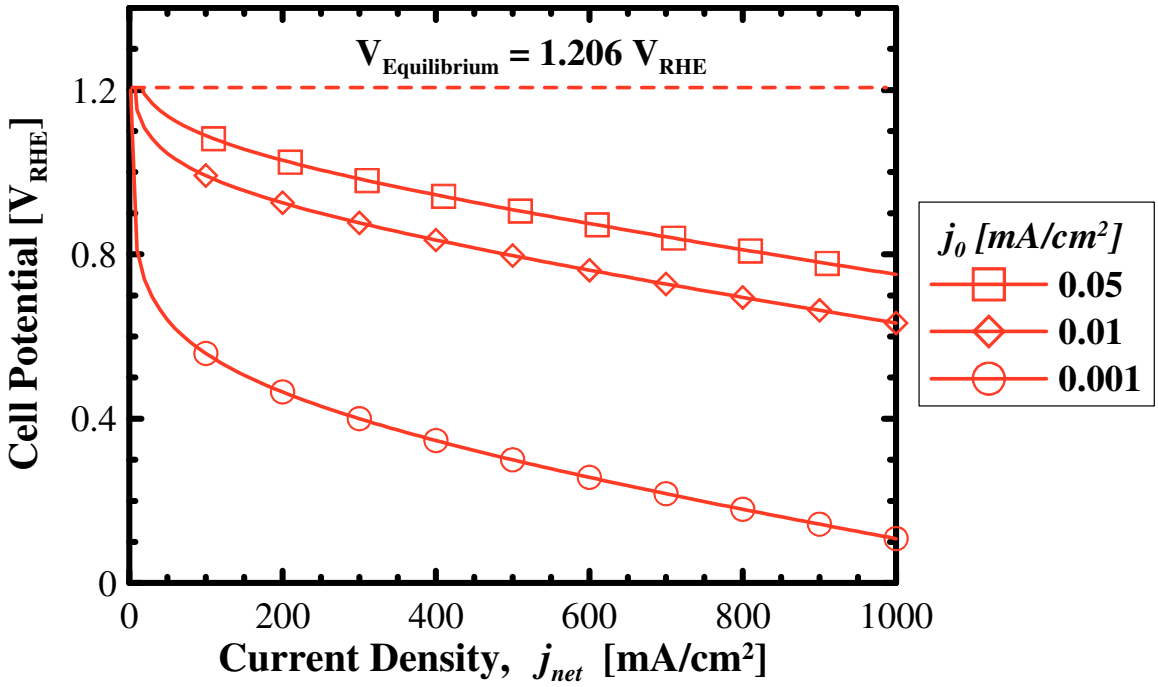

Figure 1-13 The impact of different exchange current densities on polarization curves. Calculated with Eqn. 1-31 (from [2])

Different methods that can increase exchange current density and reduce the activation loss for a PEMFC reaction include:

1. Increase the cell temperature
2. Increase the catalyst activity
3. Increase the roughness of the electrode.
4. Increase the gas pressures in the FC.

As shown in Figure 1-13, an increase in j_0 has the effect of increasing cell potential by a constant amount for all current levels and is one of the main research focuses in academic and industrial labs.

1.3.2 Ohmic Loss

Electronic resistance in the fuel cell components and the membrane (electrolyte) resistance are the two main sources of the ohmic loss. The ohmic potential loss is given by Ohm's law:

$$\eta^{Ohmic} = j_{net} r , \qquad \text{(Eqn. 1-26)}$$

where r is the area-specific resistance.

1.3.3 Mass Transport Losses

During FC operation, the partial pressures of fuel ($H_{2(g)}$) and oxygen gradually decreases as the current increases. A pressure drop of the reactants at the electrode, from P_1 to P_2, impacts the overall cell potential by ΔV. This can be approximated by the Nernst equation:

$$\Delta V = \frac{RT}{nF} \ln\left(\frac{P_2}{P_1}\right). \qquad \text{(Eqn. 1-27)}$$

Consider a FC operating with a fixed reactant gas flow rate and inlet pressure, P_1. There exists a maximum current density, j_{lim}, at which the reactant gas is consumed at the same rate as the supply. It is apparent that the current density output of this "fixed-supply FC" cannot exceed j_{lim}. It is also apparent that if no current is flowing (open circuit), the reactant gas pressure anywhere inside the FC would be P_1. However, once the current, j_{net}, starts to flow, reactant gas is consumed inside the FC and the pressure would decrease by the same proportion, to P_2. The relationship between P_1, P_2, j_{net} and j_{lim}, is given by:

$$P_2 = P_1\left(1 - \frac{j_{net}}{j_{\lim}}\right). \qquad \text{(Eqn. 1-28)}$$

Combining Eqns. 1-27 and 1-28, one gets:

$$\Delta V = \frac{RT}{nF}\ln\left(1-\frac{j_{net}}{j_{\lim}}\right). \qquad \text{(Eqn. 1-29)}$$

The mass-transport potential loss thus becomes:

$$\eta^{Mass-Transport} = B\ln\left(1-\frac{j_{net}}{j_{\lim}}\right), \text{ where } B = \frac{RT}{nF}. \qquad \text{(Eqn. 1-30)}$$

Considering Eqns. 1-24, 1-25, 1-26 and 1-30, a general equation for the different impacts of irreversible FC reaction losses on the polarization curve (Figure 1-12) is:

$$V_{cell} = E^0 - A\ln\left(\frac{j_{net}}{j_0}\right) - j_{net}r - B\ln\left(\frac{j_{net}}{j_{\lim}}\right). \qquad \text{(Eqn. 1-31)}$$

Table 1-4 shows values of parameters used in Eqn. 1-30 for a PEMFC operating at 70 °C. These values were used to calculate the polarization curve shown in Figure 1-13.

Table 1-4 *Common Values Used in Eqn. 1-31*

Constant (unit)	Value
E^0 (V)	1.201
r (kΩ cm^2)	2.45E-4
j_0 (mA/cm^2)	(various)
A (V)	0.06
B (V)	0.05
j_{lim} (mA/cm^2)	900

The model presented here is a very simple approach for qualitatively understanding PEMFC polarization curves. Larger systems such as FC stacks are considerably more complex with many more parameters describing the effects of the catalyst layer (catalyst support corrosion at various temperature/electrochemical conditions) and water management (drying and flooding of the membrane effecting proton conductivity) [2].

1.4 Fuel Cell Research Focus at Dalhousie University

At Dalhousie University, FC research focuses on improving catalyst efficiency. This includes lowering the overall Pt content, lowering the cathode ORR overpotential, improving electrochemical stability, reducing poisoning effects, improving catalyst supports…etc. On-going research approaches for reducing the Pt content include developing non-noble metal catalysts, novel catalyst structures such as those described by the core-shell model and alloying Pt with non-noble metals. Alloying Pt with other transition metals, in addition to lowering the Pt content, can improve the oxygen reduction kinetics relative to Pt.

1.5 Structure of Thesis

This thesis discusses investigations of Pt-based dealloying catalysts for the oxygen reduction reaction. Chapter 2 presents background to a new high surface area catalyst support, namely the nano-structured thin film (NSTF) support made by the 3M Company, and to the dealloying phenomenon. Chapter 3 explains the experimental techniques used. Chapters 4, 5 and 6 presents the results of this investigation in order, from a new catalyst screening technique (Chapter 4) to the physical impact of the dealloying catalysts (Chapter 5) and to a coulometric examination of the dealloying process (Chapter 6).

Chapter 2 NSTF Catalyst Support and Dealloying Catalysts

One of the key focuses in PEMFC research is to improve the efficiency of noble metal (typically Pt) based catalysts. There are two main approaches to this goal: 1.) reduce the use of Pt by using a high surface area catalyst support and ensure that the Pt itself has extremely high surface area, and 2.) increase the activity of the Pt catalysts. A common catalyst support is carbon black that has advantages of high surface area, good conductivity and low cost. However, it has been proven that carbon black is susceptible to corrosion during PEMFC operation [22, 23]. A possible solution to this is to use the Nano-Structured Thin Film (NSTF) as catalyst support [18]. In order to reduce Pt usage, a common scheme is to use Pt alloys. Many Pt alloys were also found to have better-than-Pt activity. Traditionally, researchers have focused on relatively low M-content alloys, e.g. Pt_3Ni and Pt_3Co, [24] which are quite stable in the fuel cell environment.

Alloying of Pt with different transition metals was explored (and is now used) for the cathode ORR of phosphoric acid fuel cells [25], [26]. In recent years, Norskov et al. provided a theoretical framework via the "d-band center theory of heterogeneous catalysis" and applied it to Pt alloy ORR electrocatalysts [27], [28]. The study focused on calculating the adsorption energies of two adsorbed species: O and OH on the Pt (111) surface in the presence of adsorbed water and an electric field. This approach avoids complicated pathways that may include many transition states and allows a simpler understanding of the activation overpotential of the ORR reaction.

After the successful introduction of the d-band center theory, Adzic and Mavrikakis et al. used the same concept calculated the activity of single-crystal nanoparticle surfaces of various metals (Au, Ag, Pd, Rh, Ir, and Ru) and compared the results with the activity of Pt monolayers on the same type of single crystal surfaces [29], [30]. The data indicated that for high catalytic activity of the ORR in alkaline media, the catalytic surface should exhibit the optimum balance between the kinetics of O–O bonding breaking and the electroreduction of the oxygenated intermediates or O–H formation. The results correlated well with the metal's d-band center for the ORR in alkaline solutions. Plots of the kinetic currents of the ORR on these types of electrode surfaces also showed a volcano-type dependency on the d-band center of the metal catalyst, with Pt_3Ni, Pt_3Co and Pt_3Fe having the highest activities [31]. Although the studies showed that alloying Pt with Co resulted in kinetic activity gain, the long term stability of the alloy under PEMFC operating conditions is still a focus of research [32].

Other than the successes reported by various researchers on the low M-content Pt alloys, recent results from other groups that examined high M-content Pt alloys have been very encouraging, showing good ORR activities [33-39]. The high M content alloy precursors underwent a physical change known as "dealloying". At the beginning of life, M atoms in the Pt-M catalyst precursor dealloy and a highly porous Pt-rich outer layer is formed. There can be an inner core that has the same composition as the precursor. This chapter presents a collection of background information on the two topics mentioned above that is the main focus of this thesis

2.1 Nano-Structured Thin Film (NSTF) as Fuel Cell Catalyst Support

There are two basic types of catalyst structures generally known and commonly used in proton exchange membrane fuel cells: Pt metallic fines (for example, Pt black) [40], [40-43] or catalysts dispersed on carbon blacks (Pt/C) [21], [21], [44-49]. Pt black is a fine powder of platinum with good catalytic properties. The powder particles are typically micrometers in diameter with an overall specific surface area of 5 ~ 10 m^2/g. The name "platinum black" is due to the black color of the powder. Pt black is widely used as a thin film covering Pt foil or Pt electrode mesh, forming a Pt electrode for laboratory electrochemistry experiments [50], [51]. The process of covering Pt electrodes with a fresh layer of Pt black is called the "platinization of platinum". The platinized Pt has a true surface area that is higher than the geometric surface area of the electrode and, therefore, has superior catalytic activity than that of a smooth Pt surface [52]. The use of pure un-supported Pt black powder as a fuel cell electrode catalyst, although effective, requires a large amount of Pt, about 2~4 mg/cm^2, and is considered an overuse Pt by recent standards (< 0.4 mg/cm^2, set by the U.S. Department of Energy as of 2010).

2.1.1 Pt Nanoparticles Supported on Carbon Black

Instead of using Pt black, a supported catalyst structure is typically used in fuel cell catalyst layers today [47], [49]. Pt catalyst is deposited as nanoparticles on high surface area supports made of carbon black. The support provides a large area reaction zone that gives access to the reactants and space for removal of the products. It also provides a good conductive pathway to carry the electric current from the reaction site to the gas diffusion layer (GDL). The supported catalyst has a high surface area to volume ratio and

the carbon-supported catalyst powder is then blended into the ionomer ink to be coated onto the membrane of the MEA.

Carbon black is a form of disordered carbon that has an extremely high surface area to volume ratio. Typical carbon black has a grain size range between 20 ~ 300 nm and is commercially available in large quantities. Figure 2-1 shows a TEM image of a commercially available Pt/C catalyst (20% wt./Pt from E-Tek Inc.) [53]. The Pt nanoparticles shown in Fig. 3-1 are 6 ~ 8 nm in diameter and the carbon black support is made of particles 100 ~ 200 nm in diameter. The carbon black particles are joined, forming filaments, much like a pearl necklace, and provide good conducting pathways between the Pt catalyst and the electrode.

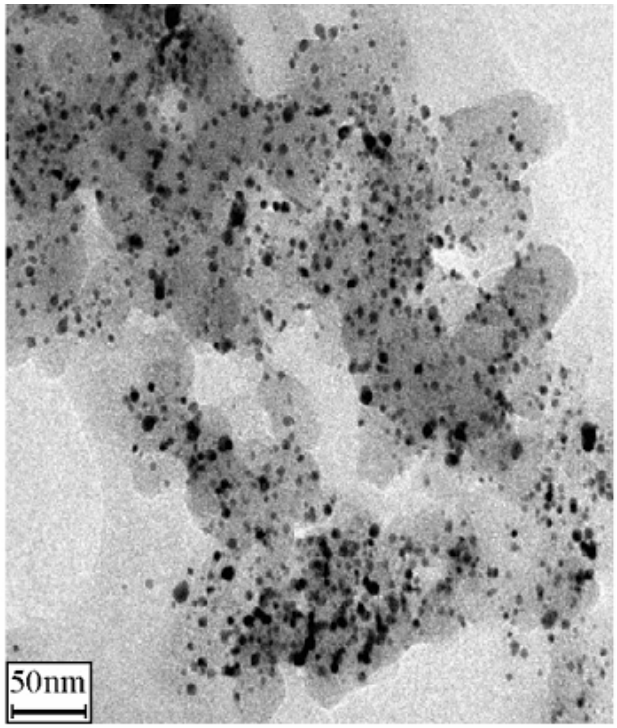

Figure 2-1 TEM image of Pt/C supported catalyst (from [53]).

The use of carbon black as a Pt catalyst support was reported as early as 1992 by Wilson et al. [49]. Since then, Pt/C has become a commonly used fuel cell catalyst for several reasons:

1. The surface area of the catalyst is greatly increased by using a carbon support. For example, Vulcan XC72 carbon black has specific surface area of 250 m^2/g.
2. It is relatively easy to get uniformly and highly dispersed catalyst even when the catalyst loading is more than 30 wt% (in general, higher catalyst loading leads to better FC performance)
3. Carbon has sufficient electronic conductivity and chemical stability under most FC operating conditions.
4. Carbon supported catalysts are more stable than non-supported catalysts against catalyst agglomeration under FC operating conditions.

2.1.2 Carbon Corrosion and the "Start-up/Shut down" Problem

The Pt/C catalyst-support for FC MEAs has been tested extensively by many researchers focusing on the commercialization of FC vehicles. Issues such as the optimum Pt-carbon-ionomer ratio for peak power output, sustained power output and durability over long periods of time have been investigated. It was found that the Pt/C catalyst, under constant power output, has good durability and was able to meet the initial DOE benchmarks [13], [14], [54]. However, when the same stack, which had just passed a constant load durability test, was field-tested in a prototype vehicle, it failed after several days without exception [22]. During postmortem autopsies of failed stacks, it was found that the

cathodes of the stacks were corroded away while the anode layers were in pristine condition.

This un-anticipated failure of the FC stacks became an important research topic because of the commercial investments involved. In 2005, Reiser et. al. [22] proposed the mechanism for this type of failure that is now called "Start-up / Shut-down failure", "start-stop failure", or "reverse-current" failure (Figure 2-2). As the name implies, this type of stack failure happens during the start-up and shut-down period of the FC stack and therefore was not detected during constant-load tests.

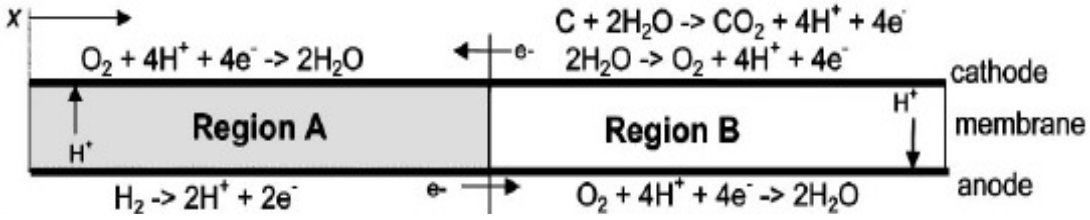

Figure 2-2 "Start-up / Shut-down" carbon corrosion mechanism (from [22])

This corrosion mechanism does not only apply to the FC stack during start-up and shut-down periods but also during normal fuel cell operation when fuel is starved locally [55-58]. There are many proposed solutions to this problem, including shorting out all of the MEAs in the stack or keeping an active H_2 flow in the anode after shut off. Such engineering methods do not protect the cells from local fuel starvation during normal operation, so a materials science approach is favored. The aim for FC material scientists is to find a cathode catalyst support that has better corrosion resistance and a corrosion

potential higher than that of oxygen evolution. Then, when reverse current occurs during fuel starvation, O_2 evolution is the favored reaction and is less damaging to the stack.

In addition to the "Start-up / Shut-down failure" corrosion during regular fuel cell operation, Stevens et al. suggested that the Pt/C catalyst is likely to corrode when the fuel cell is idle [23]. In Stevens et al.'s report, different Pt/C catalysts were placed in a 150°C isothermal oven at 50% RH in air. The masses of the Pt/C catalysts were measured over long periods of time (up to 2000 hours). The Pt/C mass decreased over time (shown in Figure 2-3) because the carbon support underwent Pt-catalyzed combustion. The Pt-catalyzed reaction was accelerated when the humidity was high. Stevens et al. also showed that a carbon support that had a higher degree of graphitization had better resistance to Pt-catalyzed combustion.

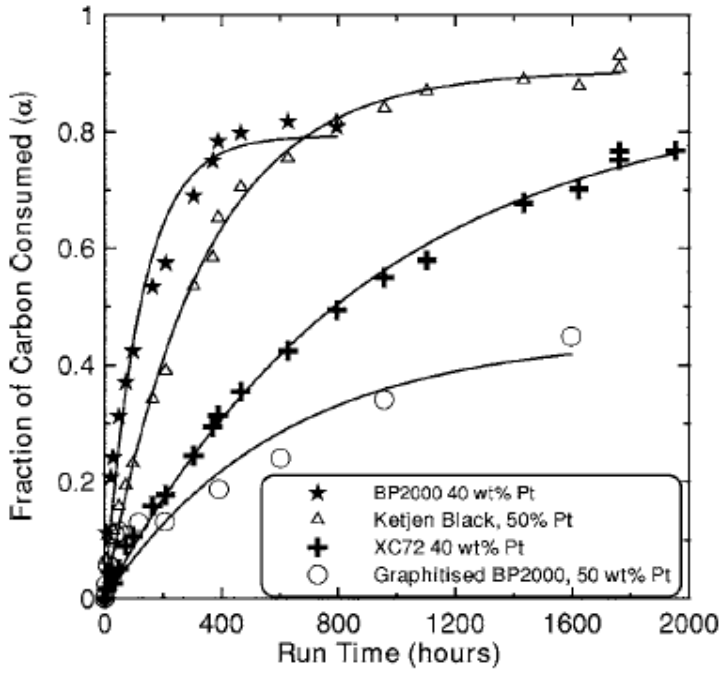

Figure 2-3 Pt/C catalyst mass-loss versus time (from [23])

It is therefore clear that carbonaceous materials are not ideal for fuel cell catalyst supports. The durability of the catalyst and support is one of the key factors required for the success of PEMFCs. An alternate support is the Nano-Structured Thin Film (NSTF) material made by the 3M Company.

2.1.3 3M Company's Nano-Structured Thin Film (NSTF)

The start-up / shut-down corrosion of the disordered carbon-based catalyst support poses a challenge for fuel cell researchers. One of the solutions is to use non-carbon catalyst supports. An example of a non-carbon catalyst support that has gained much attention is the vertically aligned nano-structured thin film (NSTF) support. In 1994, Debe et. al. reported the growth of a highly oriented NSTF of an organic pigment [60]. The nanostructured film consists of a dense array of uniformly oriented crystalline whiskers as shown in Figure 2-4.

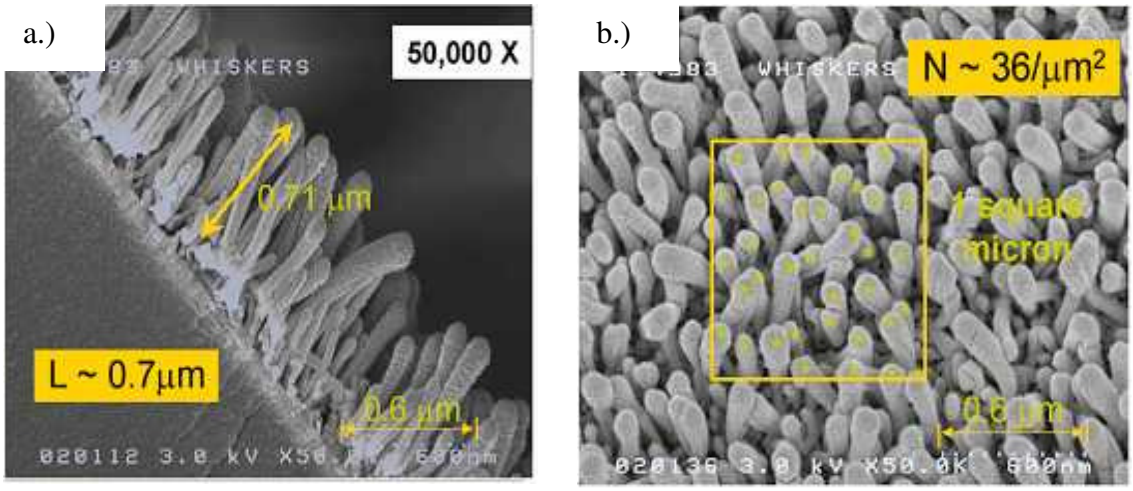

Figure 2-4 SEM images of catalyst-coated organic NSTF 'whiskers': a.) side view of the oriented NSTF and b.) top view of the NSTF bundles

The mean-cross-sectional widths and thickness of the NSTF whiskers are 50 ± 10 and 27 ± 8 nm, respectively. The height of the whiskers is between 1 ~ 2 μm. The whiskers have an areal number density of 30~50 / μm^2 (corresponding to 3 ~ 5 billion / cm^2) and have a geometric surface enhancement factor (SEF) of 10 ~ 15 cm^2_{actual} / $cm^2_{geometric}$. The material used to form the film is the organic pigment N, N-di(3,5-xylyl)perylene-3, 4 : 9, 10 bis(dicarboximide), called perylene red or PR149. It is deposited in vacuum (< 1 Torr) and annealed at 220°C for 20 minutes. During the annealing process, the deposited polycrystalline film self assembles into vertically oriented nano-scale "whisker" structures. The electron diffraction of a selected region on a single NSTF whisker showed that NSTF whiskers are crystalline [60-62]. The NSTF material reported is normally grown on an organic film substrate. Then the catalyst (Pt or Pt alloy) is vacuum deposited (by sputtering or vaporization) onto the NSTF, much like snow falls on a collection of posts. The Pt-NSTF is then readily applied to the membrane by hot-roll lamination. When NSTF was used as the catalyst support, it was very stable and had good surface area enhancement properties with the same US DOE catalyst loading benchmarks [63], [64].

In recent years, researchers at Dalhousie University have used the NSTF support for sputter-deposited thin film catalysts in fuel cell MEAs [65-68]. Bonakdarpour et al. deposited different Pt binary and ternary alloy films (with Ni, Co and Fe) onto the NSTF support for corrosion tests [69], [70]. The $Pt_{1-x}Ni_x$ ($0 < x < 1$) material was deposited onto a 76 mm long by 6 mm wide NSTF strip. The composition spread library was then soaked in 1M H_2SO_4 at 80 °C for 10 days. The studies showed a limited amount of

transition metal dissolution from the surface when the transition metal content of the alloy was low. Once the transition metal content in the alloy was greater than 60 %, the amount dissolved during the corrosion test increased and it was shown that transition metals dissolved from the bulk as well as from the surface (see Figure 2-5).

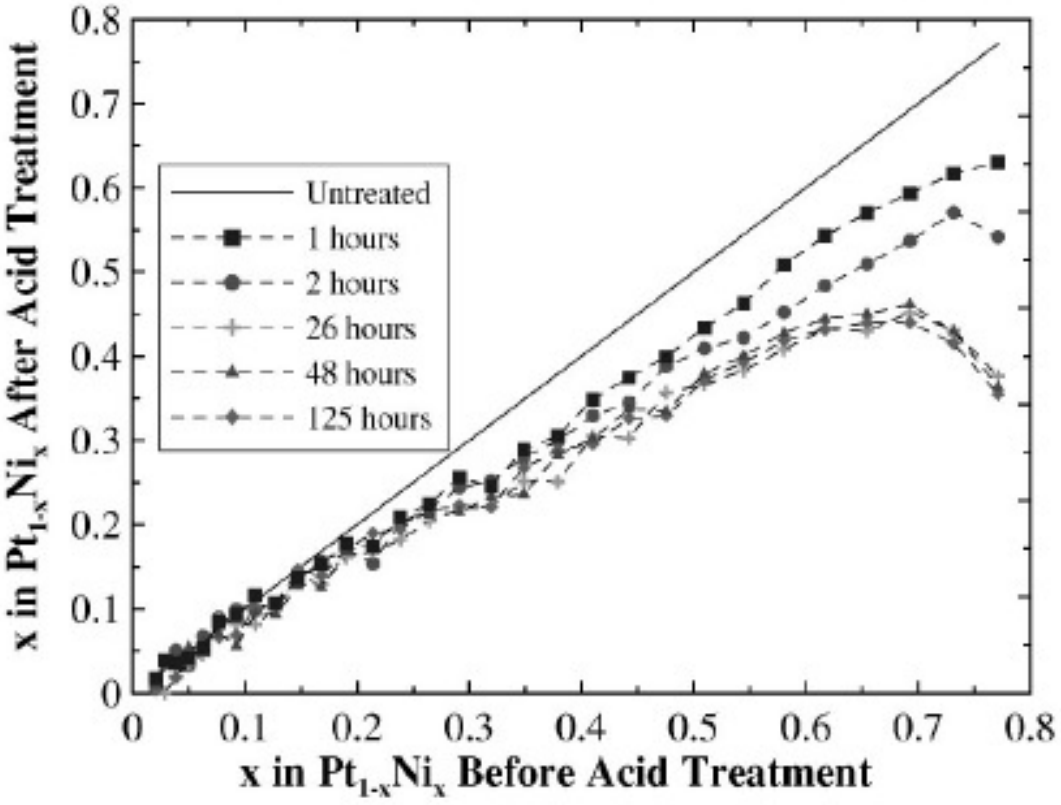

Figure 2-5 Corrosion experiment of a $Pt_{1-x}Ni_x$ (0<x<0.8) film deposited on NSTF (from [70]).

Garsuch et al. deposited thin film Pt on various under-layer materials (alumina, gold, titanium carbide and titanium disilicide) on NSTF supports, as shown in Figure 2-6. The catalysts were tested in fuel cell MEAs [66]. The study showed that gold and titanium disilicide used as underlayers on the NSTF supports lead to a loss of electrochemical surface area during operation. Migration and surface accumulation was observed when

gold was used as an underlayer material. For titanium disilicide, alloying and the generation of platinum silicide phases occurred. Alumina and titanium carbide were found to be potentially acceptable underlayer materials as well as alternative support materials on the basis of their influence on catalyst surface area.

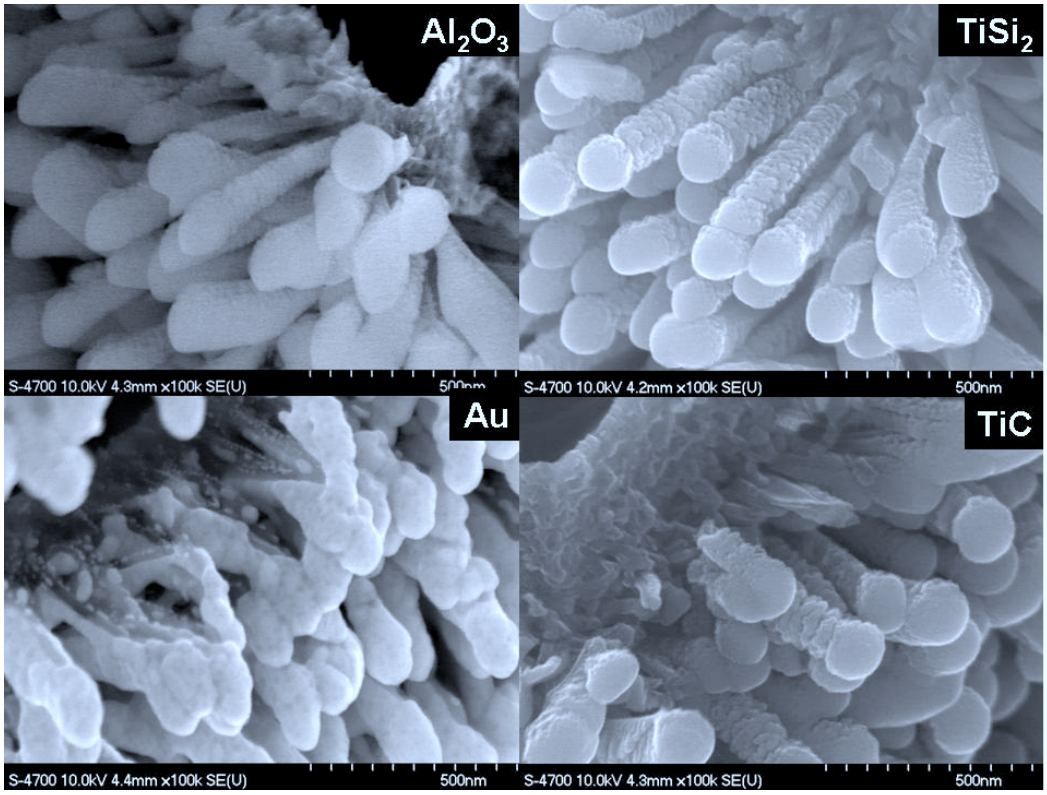

Figure 2-6 SEM images of ~ 100 nm planar equivalent coating of various catalyst materials on the NSTF support (from [66]).

2.2 Dealloyed Material as PEMFC Catalysts

Dealloying refers to the partial, selective dissolution of less noble component(s) of a binary or ternary alloy precursor, resulting in a noble-enriched, porous structure that has high surface area and different surface properties [71-73]. The amount of less-noble

species dissolved and the resulting dealloyed surface structure depends on the type and ratio of the elements in the starting precursor and the dealloying process. The dealloying process of a binary alloy has been extensively investigated in the corrosion community. Pickering et al. presented studies of Cu-Au alloys and showed Cu selectively leached away, forming a three-dimensional porous structure with a Au-enriched surface [74-78]. Lu et al. studied Ag-Au dealloying process and showed that significant dissolution of less noble Ag only occurs when the Ag content in the precursor is higher than 44% [79], [80]. As the Ag content increased, the dealloyed products showed an increasing degree of porosity, as well as Au content in the dealloyed regions [79]. Figures 2-7a and 2-7b show a precursor film with ~ 60% Ag produced a dealloyed film with visible islands of Au-Ag alloy. A precursor film with ~ 75% of Ag produced a nearly pure Au dealloyed film that was highly porous (Figure 2-7 c and d).

The Ag-Au dealloying study by Lu et al. suggested a "compositional threshold", or "dealloying threshold" for a given dealloying environment (the pH of the electrolyte) in order for the dealloying to take place. Below the dealloying threshold, the noble metal blocks the further dissolution and the process comes to a halt. This is consistent with the observations by Erlebacher and Sieradzki [81], [82], as well as earlier findings [83-86] regarding a composition-dependent electrochemical critical potential, above which the dissolution current increases significantly with potential, signaling the onset of bulk dealloying (shown in Figure 2-8). Below the critical potential, the surface is passivated by the noble element.

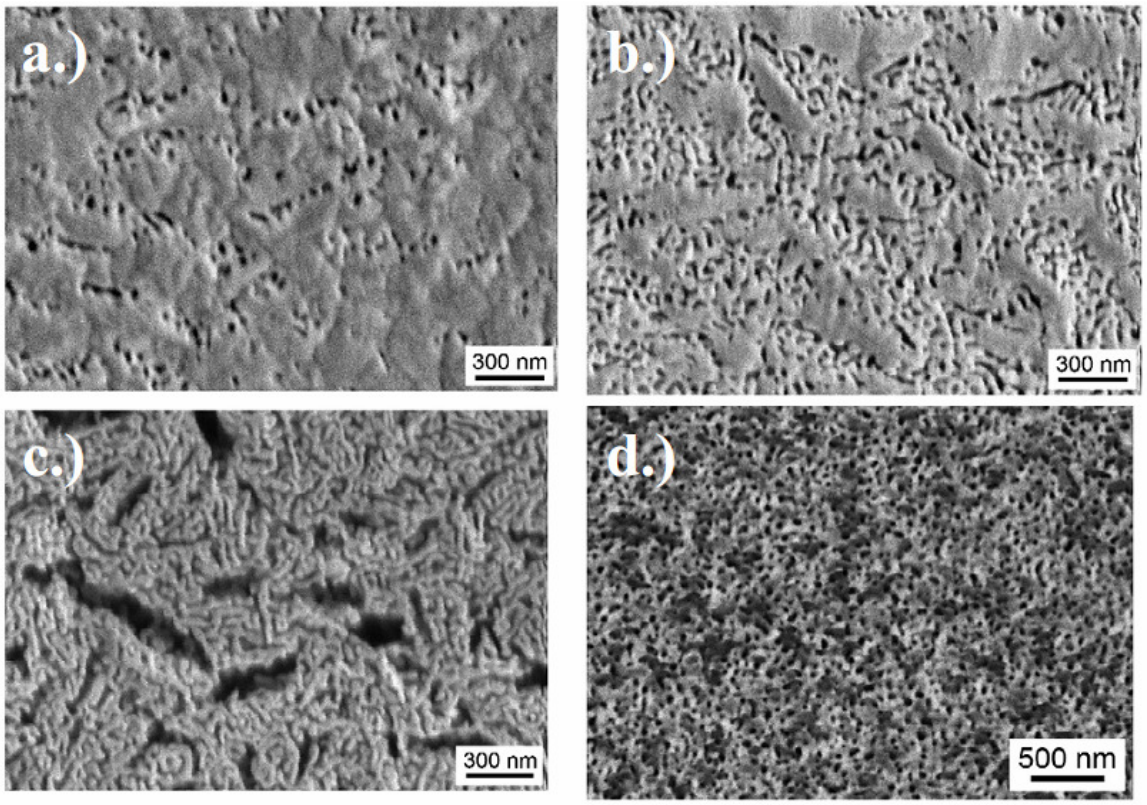

Figure 2-7 SEM images of dealloyed Ag-Au binary with different Ag content in the precursor material: 59% in (a), 65% in (b), 73% in (c) and 76% in (d) (from [79])

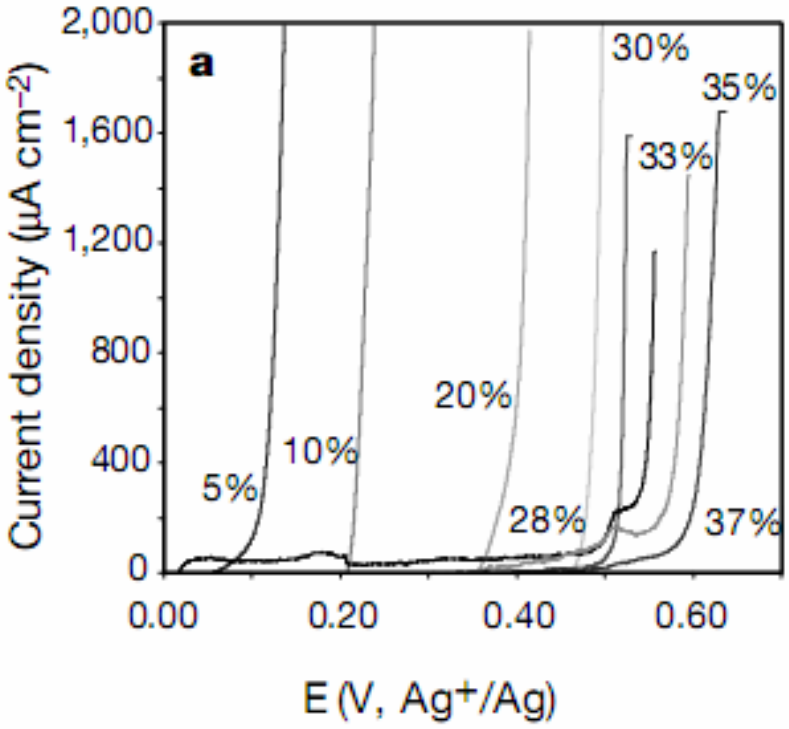

Figure 2-8 Current-potential behavior of varying Ag-Au alloy compositions (atom % Au) dealloyed in 0.1 M $HClO_4$ + 0.1 M Ag^+, the potential at which the current spikes up is referred to as the "critical potential". (from [84])

The concept of critical potential is helpful in understanding the formation of a core-shell type structure upon dealloying of a nanoparticle made of type A (noble) and B (non-noble) metals in a corrosive environment with applied potential (for an example, in a Galvanic cell). As dealloying occurs, a small amount of surface and near-surface type B atoms dissolve and the remaining type A atoms accumulate on the surface. As a result, a passivation shell that is enriched in type A atoms is formed. Thus, further dissolution of type B atoms is inhibited as long as the applied potential is lower than the critical dealloying potential of the newly formed shell alloy. If a higher potential is applied, additional type B atoms are dissolved from the particle until an alloy with a higher

content of type A atoms is formed with a critical potential that matches the applied potential.

The dealloying process has been extensively studied as a corrosion phenomenon [74], [87], [88]. However, the formation of a highly porous noble-rich surface structure has many benefits in heterogeneous catalysis, in which a large active catalytic surface area is desirable. A large active catalytic surface area can be achieved by dealloying a solid solution that is composed of the catalytic element and a less noble species that can be dissolved away, leaving a porous, high surface area structure that is composed of mostly the active catalyst. In recent years, Strasser et al. reported dealloyed Pt-M (M = Cu, Co) catalysts to be highly active for ORR in acidic media [89-91]. When a Pt-M (M = Cu, Co) alloy precursor is placed in a corrosive environment, the less noble element(s) from the surface and near-surface typically dissolves away, leaving behind a Pt-rich shell that has high surface area and high ORR catalytic activity (Fig. 3-9).

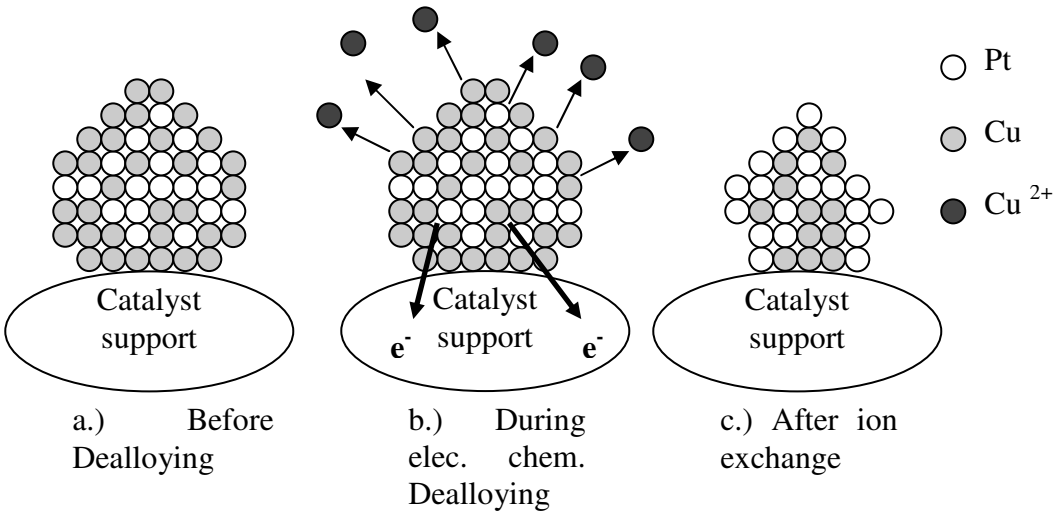

Figure 2-9 Stepwise illustration of the dealloying process of Pt-Cu from a Cu-rich precursor in (a) to a Pt-Cu core-shell nanoparticle in (c) (from [91]).

It has also been suggested that the high catalytic activity of dealloyed Pt-M catalysts results from a combination of both increased surface area and lattice strain between the Pt-rich shell and M-rich core. Strasser et al. reported that the dealloyed Pt-Cu nanoparticles showed a core-shell structure after dealloying [91], with a Pt-rich shell and a Pt-Cu alloy core. The interatomic Pt-Pt distance in the Pt-rich shell was found to be smaller than expected based on the chemical composition of the shell, suggesting the presence of a compressive strain that helped to enhance ORR activity [92]. Prior to dealloying, the Pt-M precursor would have had relatively low catalytic activity; as dealloying occurred, its electrochemical active surface area (ECSA) and specific ORR catalytic current density ($mA/cm^2_{catalyst}$) would have increased. This transient behaviour can be monitored by electrochemical techniques such as testing of MEAs in fuel cells or testing of catalyst-coated disks with the rotating disk electrode (RDE) technique.

One goal of this thesis was to combine the NSTF support with the rotating disk electrode (RDE) technique as an alternative method for screening fuel cell catalysts. The first task was to grow, characterize and use NSTF as a catalyst support on polished glassy carbon (GC) surfaces for RDE measurements. The catalysts used were pure Pt (as a control) and Pt-Ir alloys. The catalysts were sputter-deposited on both mirror-polished GC disks and NSTF-coated GC disks. The ORR activity of the disks was determined by RDE. The results were then compared to examine the contribution of the high surface area NSTF support to the overall catalytic performance of different catalyst/support combinations. Ir was selected as it is a noble metal and thus is unlikely to dissolve/corrode away to any

significant extent during normal fuel cell operation. This then allowed the author to examine the impact of the catalyst support on the electrochemical surface area and ORR performance without having to consider additional contributions from corrosion. In addition, the experiment determined whether the presence of Ir under a Pt capping layer influenced ORR performance, as shown in Chapter 4. NSTF-coated GC disks were used because they allow RDE techniques to be used to screen catalysts sputter-deposited on high-surface area supports more effectively. Once it is est ablished that the NSTF-coated disks are a viable addition to the standard RDE/RRDE technique, they can then be used to examine dealloying catalysts such as $Pt_{1-x}Ni_x$ and $Pt_{1-x}Co_x$ ($x > 0.6$) in Chapter 5.

Chapter 3 Experimental Techniques

3.1 Combinatorial Magnetron Sputtering

Traditional preparation of materials such as catalysts, inorganic compounds, and polymers, involves making and testing one composition at a time. The process is time-consuming and labor-intensive. Parallel synthesis and testing of multiple compositions or combinatorial chemistry, has been developed and is a common strategy for the discovery of chemicals in the pharmaceutical industry. The principles of the combinatorial method include a standardized method of preparing and testing multiple compositions in a single experiment and therefore minimize human error and test variations. At Dalhousie University, Professor Jeff Dahn and his team of researchers have developed and streamlined a combinatorial sputtering apparatus aimed at producing reliable composition spreads of different metal thin films. Sputter-deposition can be used to deposit thin film elements, alloys, conductors, semi-conductors and insulators on any vacuum-compatible substrate.

All thin film composition spreads described in this thesis were fabricated using a Corona Vacuum System VT-3 multi-target sputtering machine. The details of this system have been described in previous publications [93-96]. Before any sputtering run, the chamber pressure is lowered to the 10^{-7} Torr range by a turbo pump (Varian 500L/s) and a Polycold cryopump (Brooke Automation Inc.). The sputtering process involves the ejection of atoms from a target surface when it is bombarded by energetic particles like gaseous ions. The source of the bombarding ions is a plasma of an inert gas (Ar)

accelerated towards the target when an electric field is applied to the target. Typical sputtering pressures are from 1 mTorr to 30 mTorr. This is achieved by a continuous flow of Ar gas together with vacuum pumps operating at a fixed rate. The sputtering systems are magnetron based; the magnet is used for trapping electrons to increase the ionization efficiency.

Figure 3-1 shows a typical setup for a sputtering run used throughout this thesis. The sputtering chamber is equipped with four 2" diameter target magnetrons, and one plasma cleaning electrode. Figure 3a shows the sputtering chamber with two targets mounted. A Pt target was mounted at the 11 o'clock magnetron position while a Ni target was mounted at the 5 o'clock position. The Pt target has a "constant mask" covered at the end of its tunnel so the deposition profile along the sputtering track is constant throughout. The Ni target has a "linear out" mask that blocks the deposition at the inner side of the track and creates a linear gradient of deposition along the sputtering track. Figure 3-1 also shows spare magnetrons at 1, 7 and 9 o'clock covered with copper foils.

Figure 3-1b shows the substrate table after a sputtering run. Numerous sample substrates were mounted along the donut-shaped sputtering track, shown in Figure 3-1b, including two 64 channel FC electrodes, weighing disks, a holder that contains five GC disks for RDE, half-covered Si wafers and NSTF strips/sheets for X-ray and corrosion testing. To produce a film of a binary library composed of two elements, A and B, the circular table is rotated over the stationary sputtering targets, A and B. The substrates are positioned along the rotating table. The sputtering targets are behind specially designed masks

which lead to either constant or linearly varying deposition profiles on the substrate table. The thickness of films deposited during each sputtering experiment can be adjusted using the sputtering power, the rotation speed of the table, and the pressure of the sputtering chamber.

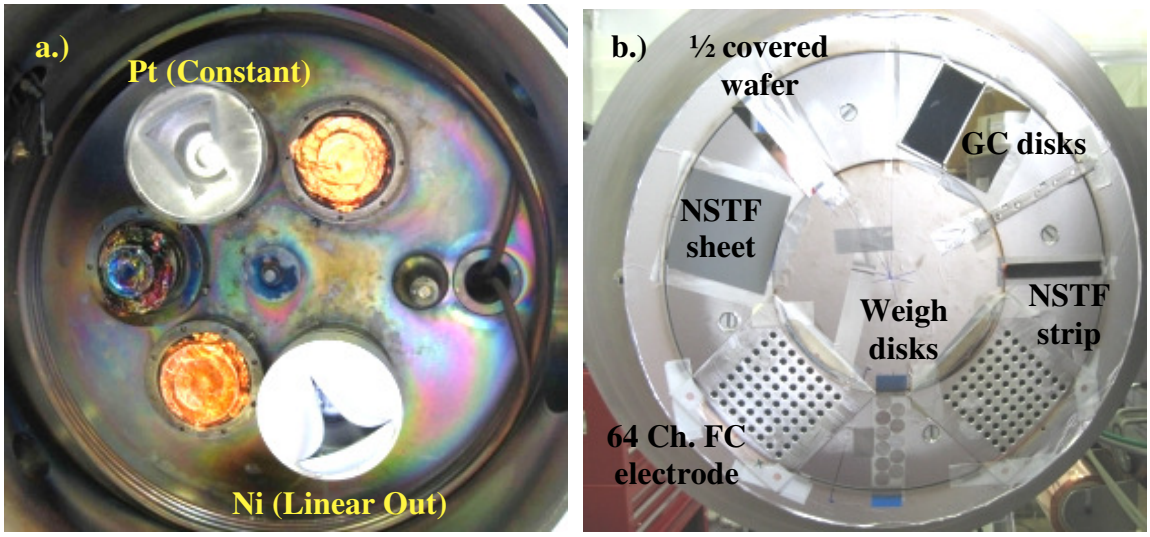

Figure 3-1 The sputtering chamber (a) that has a Pt target with a "Constant" mask and a Ni target with "Linear Out" mask while spare magnetrons were covered with copper foils. The substrate table (b) is mounted with various samples.

The amount of the deposited films was determined by weighing an array of aluminum disks placed along the sputtering track, shown in Figure 3-1. The disks are aluminum foils punched into 1.26 cm diameter (1/2 inch) circular shape. They were weighed before and after the sputtering run by a Satorius SE-2 micro-balance that has a resolution of 0.1 µg. The planar thickness of the depositions was measured with a Dektak 8 profilometer (Veeco Instruments Inc.) on a silicon wafer substrate that was partially covered by tape during sputtering. The tape was removed after deposition to reveal a fresh surface underneath. This surface was used as the baseline for the thickness measurements.

During the Dektak measurement, the stylus radius was set to 12.5 µm. The accuracy of the measurements was typically +/- 5 nm. The data from weighing disks and film thickness measurements can be used to calculate the density of the sputtered films on the planar substrate [97].

3.2 X-ray Diffraction

X-ray diffraction is an ideal method for determining the structure of materials quickly. This is because X-rays with wavelengths comparable to the inter-atomic distances of crystalline materials diffract according to Bragg's diffraction law (shown in Figure 3-2):

$$n\,\lambda = 2\,d\,\sin(\theta) \qquad \text{(Eqn. 3-1)}$$

where d, θ, λ and n are the atomic plane spacing, the angle between incident ray and the scattering planes, the X-ray wavelength and an integer, respectively [98-100].

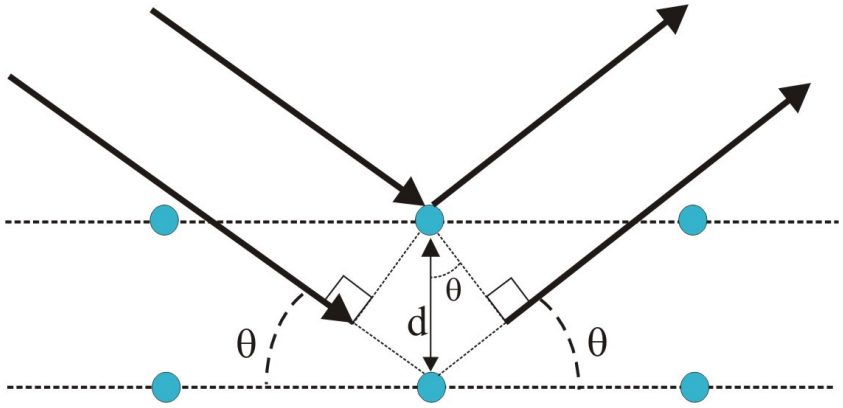

Figure 3-2 A simple schematic showing the diffraction geometry, under the conditions stated in Bragg's Law. The reflected rays are in phase and produce a maximum response at the detector.

A typical XRD measurement consists of counting the scattered X-rays as a function of the scattering angle, 2θ. The compilation of data then results in a series of diffraction peaks

(Bragg peaks) versus the scattering angle. The peaks are identified by their Miller indices (hkl), which denote atomic planes orthogonal to the (hkl) direction in the basis of the reciprocal lattice vectors. The positions of the peaks (2θ) depend on the plane spacings. For a cubic crystals,

$$\frac{1}{d^2} = \frac{h^2 + k^2 + l^2}{a^2}, \qquad \text{(Eqn. 3-2)}$$

where "a" is the lattice constant of the cubic lattice structure.

The magnitude of the peaks depends on several factors: beam intensity, atomic scattering factor, structure factor, multiplicity of the planes and possible preferential orientation of the crystal planes. The broadening of the diffraction peaks depends on the crystallite size, strain and the resolution of the detector. However, the crystallite size (or grain size) is the dominant factor and thus, after correcting for the instrumental resolution, the full width at half maximum (FWHM) of the peaks (in radian) is often used to obtain a measure of the grain size, using Scherrer's equation [100]:

$$D_{grain\ size} = \frac{0.9\lambda}{FWHM \times \cos(\theta)}. \qquad \text{(Eqn. 3-3)}$$

Detailed information about crystal structures, the physics of X-ray scattering, XRD instrumentation and data analysis can be found in numerous textbooks such as *X-ray Diffraction*, among others [100]. During the work of this thesis, the information obtained from XRD measurements such as lattice structure and grain size of the sample were gathered and correlated to the electrochemical measurements.

XRD measurements were collected with a Bruker D8 discover x-ray system equipped with a x-y-z translation stage, a Cu target x-ray tube, an incident beam monochromator to select Cu K_α radiation and an area detector. The detector was set in a position that allowed for collection of data over a scattering angle range of 30-57° at one time. The incident beam was set at 6° in order to sample a relatively large area of the thin film to improve counting statistics. XRD spectra were measured at a series of points across the composition spread for the catalyst deposited on a Si wafer and also on NSTF, counting for 900 s for each scan.

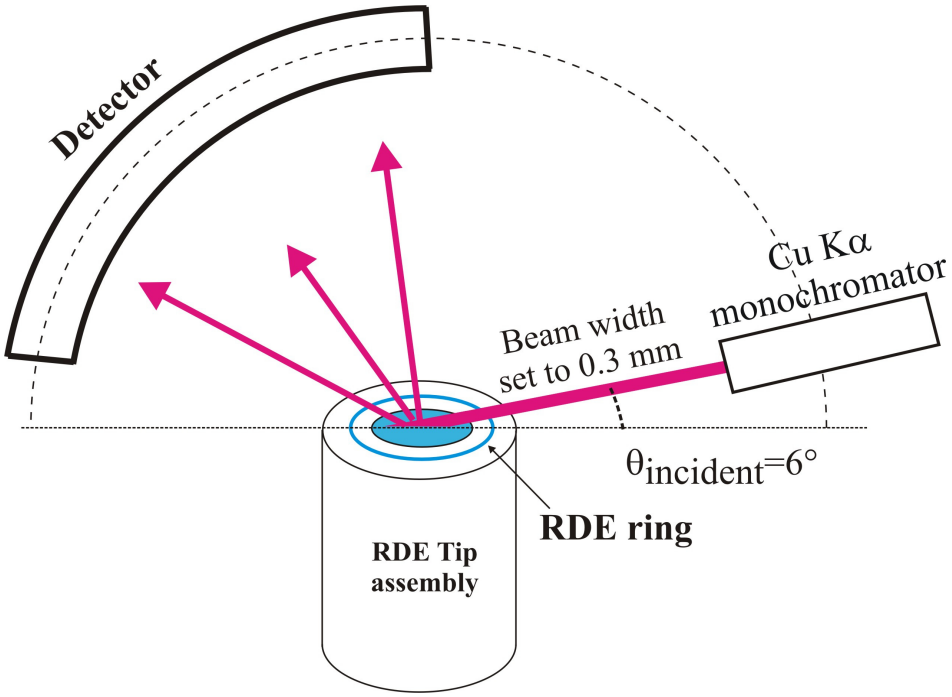

Figure 3-3 A schematic of the diffraction geometry. The sample and the incident beam are stationary with a curved detector. In order to examine materials on the RDE disk (shown here), the X-ray beam width was adjusted to 0.3 mm to avoid hitting the RDE ring (this figure is not drawn to scale).

Figure 3-3 shows a schematic of the XRD measurement performed on a RRDE electrode. The RRDE electrode is a circular disk with a diameter of 5.07 mm that contains the XRD samples. It also has a co-centric Pt ring (6.5 mm I.D., 7.5 mm O.D.) around the electrode disk. The details of the RDE electrode are discussed in the later section of this chapter. During the XRD measurements, the beam width was set to 0.3 mm so to avoid hitting the Pt ring that would give a false signal.

3.3 Electron Microprobe (EMP) Composition Determination

Electron Microprobe (EMP) is an analytical tool for determination of the composition of solid materials. The intensity of X-rays produced from an element in a compound, when it is struck by an electron beam, is proportional to the amount of the particular element present. EMP can detect elements ranging from boron to uranium. An EMP system requires a high energy electron beam (2 to 20 keV) and a good vacuum chamber. EMP is a very common method used by material scientists [101]. EMP measurements presented in this thesis were made by a JEOL JXA-8200 Superprobe using wavelength dispersive spectroscopy to determine the elemental composition of the deposited film. An accelerating voltage of 5 kV, with 50 nA current, was applied to the electron beam, which allowed all elements to be detected, but the electron beam to still be contained in the planar films. An electron spot size of 50 microns was used to average the film composition over a reasonable area.

In this thesis, 3M Company's Nanostructured thin film (NSTF) was used extensively as catalyst support. The NSTF film is a rough substrate that has a surface area

approximately 10 times larger than the geometric surface area. Any material deposited onto NSTF will therefore be distributed over a larger area than the same material deposited on a flat substrate such as a silicon wafer. The catalyst layer on the NSTF film will thus be thinner than the same material deposited on a flat substrate. From previous results at 3M, this is known to affect the crystallite grain size, which generally scales with the sputter deposited film thickness (by a factor of 10). Other than this expected difference, the data from the thinner films on NSTF were compared to the data from the films deposited on the Si wafers to ensure that any contribution from the substrates did not affect the result. In principle, the results from the two substrates should be equivalent.

3.4 Rotating (Ring) Disk Electrode Technique

The electrochemical measurements presented in this thesis were made using the rotating disk electrode (RDE) technique. RDE is a 3-electrode technique that is performed in a solution cell. The Rotating Ring Disk Electrode technique, or RRDE, uses the same setup as RDE with an added ring and will be discussed later. The RDE method provides an alternative way of assessing the catalytic behavior of the material other than MEA testing in a fuel cell. Some of the unique aspects of RDE measurements include control of working pH by changing the solution pH, a convenient way of detecting hydrogen peroxide produced during the ORR via the ring current (with RRDE) and studying the impact of impurities. The RDE technique can provide a highly accurate measurement of ORR activity and its fundamental approach lead to characterizing the impact of Pt electrode surface crystalline structure on ORR activities [102-104]. This was done by RDE of single crystals of Pt and Pt alloys. Such experiments were not possible in a FC

MEA because complexities such as electrode structure and the mass-transport effects that exist in a FC MEA are not present in RDE.

The principles of RRDE operation are covered in numerous experimental technique / electrochemistry texts including: *Electrochemical Methods: Fundamentals and Applications* [105], *Fundamentals of Electrochemical Science* [106] and *Electrochemistry: Principles: Methods and Applications* [107].

3.4.1 RRDE Mass-Transport Limited Current Density

The analytically defined mass-transport limited current is one of the fundamental differences between RRDE and an actual FC MEA. In a FC MEA, the mass-transport depends on various parameters such as H_2/O_2 gas flow rates, humidity, temperature, pressure, diffusion…etc., where as RRDE is a "hydrodynamic electrochemistry" technique. RRDE enables "forced convection" to set the transport rate of the active reactant species to the electrode. RRDE operation forces convection by rotating the electrode in the aqueous electrolyte that pushes the electrolyte at the electrode surface away and draws fresh electrolyte to the surface at a constant rate. Because of this, the rate-determining parameter, known as the "mass-transport limited current", in the measurement can be analytically realized [105]. The derivation of the RRDE mass-transport limited current is beyond of the scope of this thesis and can be found readily in textbooks [105], [107], [108]. The mass-transport limited current density, as a function of various RRDE experimental parameters, is:

$$j_{diff-\lim} = \frac{i_{diff-\lim}}{A} = 0.620nFD^{\frac{2}{3}}\mu^{-\frac{1}{6}}C\omega^{\frac{1}{2}}. \qquad \text{(Eqn. 3-4)}$$

The parameters used in Eqn. 3-4 are listed in Table A-1. The diffusion-limited current density is derived directly from the convection of fresh electrolyte to the electrode surface regardless of the electrode surface properties (catalyst type, surface roughness…etc.) [105], [107], [108]. In other words, Eqn. 3-4 shows the physical limit of electrical current generated in an RDE experiment is limited by the delivery rate of fresh electrolyte to the electrode surface. Eqn. 3-4 also shows the delivery rate of fresh electrolyte in an RDE experiment can be changed by the rotation rate (ω in Eqn. 3-4) of the electrode, shown in Figure 3-4.

Table 3-1: *Parameters and Preferred Values Used*

symbol	name	Preferred value	unit	note
n	Number of electrons	4		$O_2 + 4H^+ + 4e^- \rightarrow 2H_2O$
F	Faraday's Constant	96485	Coulomb / mole	
D	Diffusion Coefficient	2.1E-5	cm^2 / sec	For aqueous $HClO_4$ electrolyte, $[HClO_4] < 1.0$ M ([109])
μ	Kinematic Viscosity	1.01E-2	cm^2 / sec	
C	Electrolyte Bulk Concentration	various	mol / mL (mol / cm^3)	Typically $[HClO_4] = [H^+] = 0.1$ M
ω	Rotation Rate	various	rad / sec (sec^{-1})	Typically 900 ~ 2500 rpm
j	Current Density	various	Amp / cm^2	
A	Area	various	cm^2	0.201 cm^2 for a 0.507 mm diameter GC disk

Figure 3-4 shows typical RDE polarization measurements made with different disk rotation rates. The sample was 5 mm O.D. mirror-polished polycrystalline Pt RDE measured at ambient conditions (20°C, 1 atm.). The diffusion-limited current density for each measurement is reached when the current shows a flat plateau, typically at $V < 0.6$ V_{RHE}. It is apparent that the diffusion-limited current density is proportional to the

square-root of rotation rate (Eqn. 3-4): ~ 1.5 mA/cm^2 for 100 rpm, 3 mA/cm^2 for 400 rpm, 4.5 mA/cm^2 for 900 rpm and 6 mA/cm^2 for 1600 rpm. Figure 3-4 also shows an on-set potential around 0.97 V_{RHE} for all polarization curves, this is typical for mirror-polished Pt or Pt-alloy samples and will be discussed in later chapters. It should be noted that the $j_{diff\text{-}lim}$ for RDE measurement is orders of magnitudes smaller than that of a FC MEA (~ 1 A/cm^2 at 0.6V). However, the well-defined diffusion-limited current density of RDE technique allows researchers to accurately examine the "kinetic region" (shown in Figure 3-4 as the shaded potential region) and will be discussed in detail next.

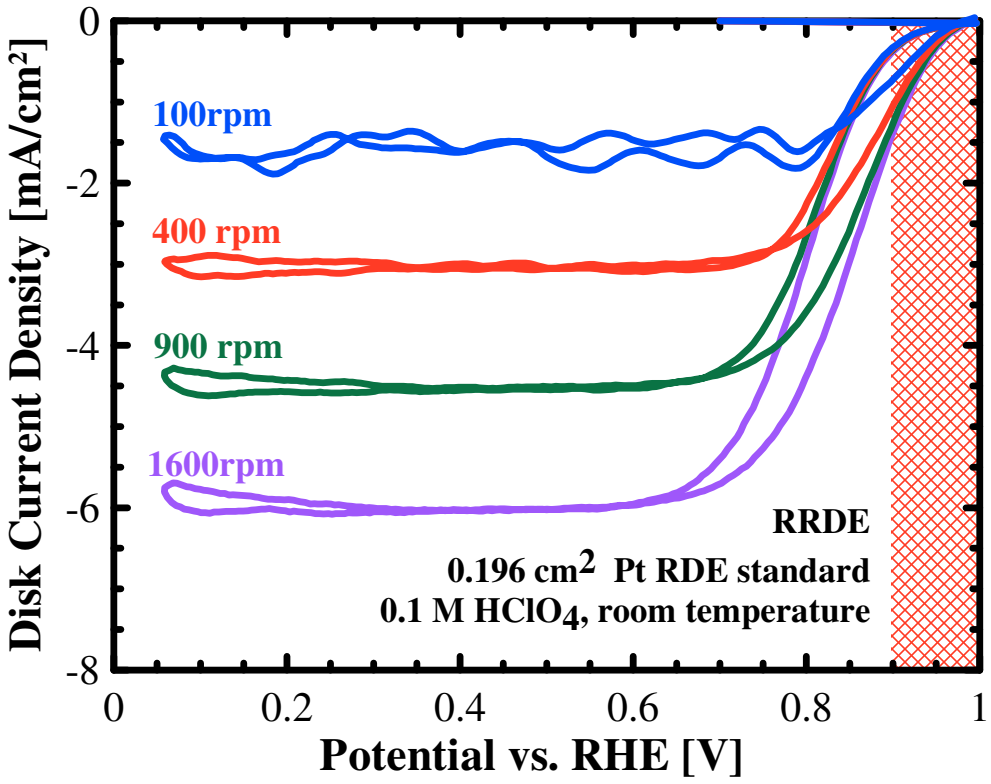

Figure 3-4 A typical Pt RDE polarization plot at various rotation rates. The shaded region (V > 0.9 V_{RHE}) is known as the "kinetic region".

3.4.2 RDE Kinetic Current Density

In the absence of any mass transfer effects, i.e. when the current is small in the high potential region ($V > 0.9\ V_{RHE}$ for a mirror polished surface), only kinetic contributions are significant. The relationship between the diffusion-limited, kinetic and measured current densities is described by the Koutecky-Levich relation (K-L Eqn.):

$$\frac{1}{j_{net}} = \frac{1}{j_{kinetic}} + \frac{1}{j_{diff-\lim}} \qquad \text{(Eqn. 3-5)}$$

where j_{net} is the measured current density in the "kinetic region", shown in Figure 3-4 as the shaded area and $j_{kinetic}$ is the kinetic current density. The derivation of the K-L Eqn. is beyond the scope of this thesis and can be found in *Electrochemical Methods: Fundamentals and Applications* [110] and *Electrochemistry: Principles: Methods and Applications* [111].

3.4.3 RDE Instrumentation

Figure 3-5a shows a typical setup of the RDE experiment. All RDE experiments were performed in a single-compartment glass cell (#6961-64 from ACE glass) filled with ~125 mL of 0.1 M $HClO_4$ electrolyte prepared from doubly distilled 70 wt% stock solution (GFS Chemical) and 18 MΩ nano-pure water from a Barnstead nanopure Diamond system (Model D11911). A Pt-wire was used as the counter electrode with a Cl^- free Koslow mercury/mercurous sulfate (MMS) reference electrode. Different gases (Ar, O_2 and H_2) were introduced into the electrolyte via a 2 μm fritted tube (#9435-10 from ACE Glass). All of the rotating ring-disk electrode (RRDE) measurements were

performed using a Pine electrochemical system (AFMSRX rotator and AFCBP1 bipotentiostat).

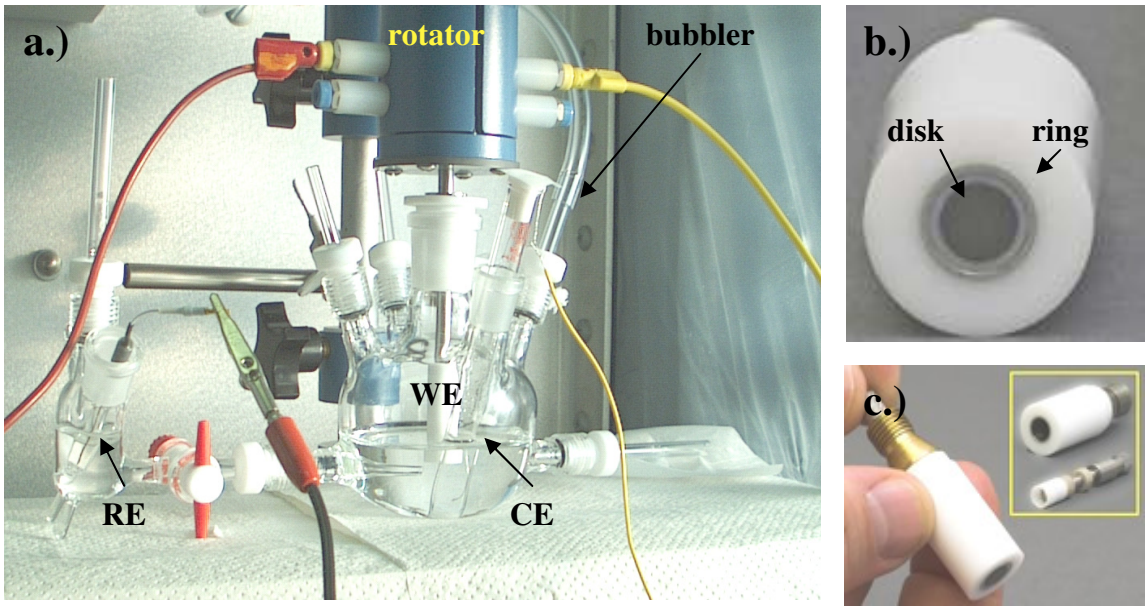

Figure 3-5 RDE experimental setup (a) includes the working (CE), reference (RE) and counter (CE) electrodes. The bubbler supplies Ar, O_2 or H_2 gases. The disk and ring are shown in (b). RRDE tip assembly is shown in (c). (from [112])

During an RDE experiment, extreme care was taken to maintain clean glassware, cell parts and samples during handling. Typical cleaning procedures for glassware and Teflon cell parts included 0.1 M NaOH base bath and boiling the glassware and the parts in nano-pure water. The RRDE response of a 1 µm polished Pine Pt (polycrystalline) RDE electrode was measured regularly to confirm that the equipment and materials used were able to generate performance curves in agreement with state-of-the art measurements from other researchers [16]. The potential of the Hg/Hg_2SO_4 reference electrode was calibrated versus a reversible hydrogen electrode (RHE) arrangement for each individual

disk measurement. All of the potentials discussed in this paper are potentials vs. this RHE calibration potential. All measurements were carried out at ambient temperature.

3.4.4 RDE Data Analysis and Key Terminologies

For each sample, the surface enhancement factor (SEF) is the ratio of its electrochemical surface area (ECSA) to the geometric surface area of the 5 mm diameter disk. Figure 3-6 shows that the ECSA was calculated by numerically integrating charge for the $H^{+}_{des\ Ar\text{-}CV}$ regions of the CVs (as shown in Figure 3-5) taken under Ar-purged cell conditions and using the 210 μC/cm^2 conversion factor commonly used [113] for the charge corresponding to a 1:1 coverage of Pt sites.

$$SEF = ECSA / SA_{planar} = \frac{H^{+}_{ads\ Ar-CV}}{210\ \mu C\ cm^{-2}} \Big/ 0.195\ cm^{2}_{\ planar} \qquad \text{(Eqn. 3-6)}$$

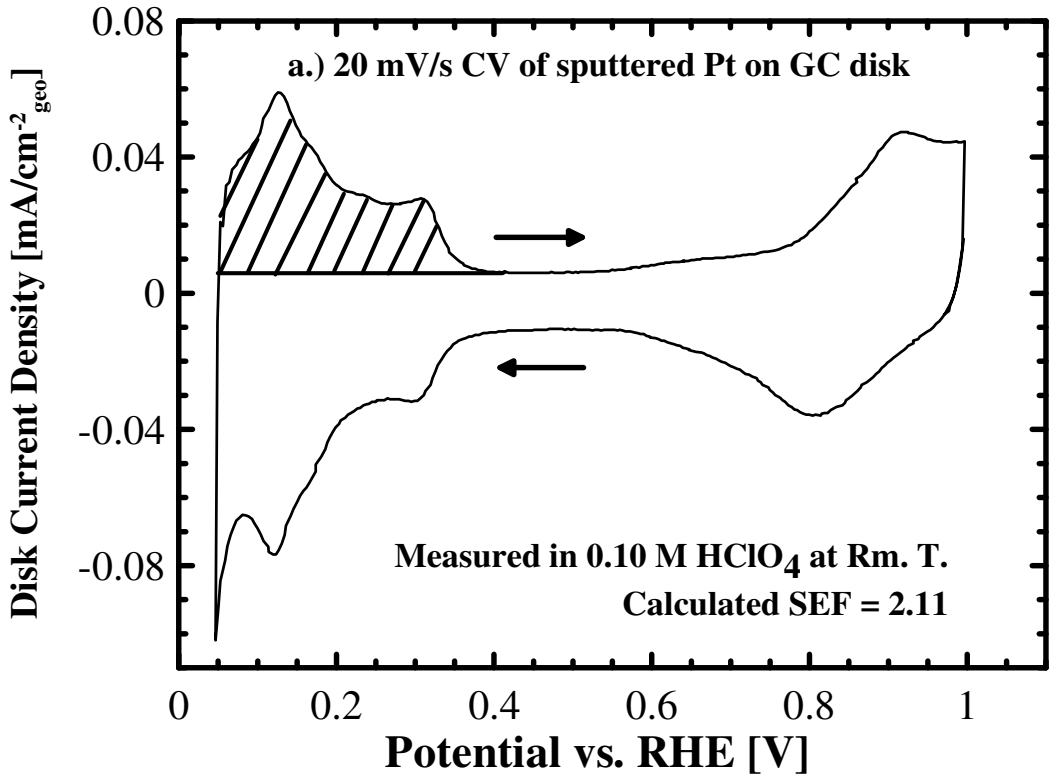

Figure 3-6 The Surface Enhancement Factor (SEF) was determined by numerically integrating the hydrogen desorption region of the CV (shaded region).

The Faradaic current density, j_{fara} (current per geometric cm^2 of electrode area) measured for a sample was determined by subtracting the non-Faradiac contribution (measured with Ar CVs) from the total current density, $j_{fara} = -(j_{ORR} - j_{CV})$. The true planar kinetic ORR current density measured per geometric surface area, j_{planar}, was calculated through use of the Levich relation [114]:

$$j_{planar} = \frac{(j_{fara} \times j_{diff})}{(j_{diff} - j_{fara})} \qquad \text{(Eqn. 3-7)}$$

The planar kinetic current density, j_{planar}, was divided by SEF to obtain the specific electrochemical current density, $j_{specific}$.

$$j_{specific} = j_{planar} / SEF \qquad \text{(Eqn. 3-8)}$$

In the Tafel kinetic analysis of a catalyst, both current densities $j_{specific}$ and j_{planar} were plotted on a logarithmic scale as the horizontal axis against V_{RHE} as the vertical axis. In this thesis, criteria such as SEF, j_{planar} and $j_{specific}$ of a potential catalyst were measured over many potential cycles and compared to form an analysis of the sample's catalytic durability. The SEF shows the available catalytic surface of the sample, j_{planar} is the overall catalytic activity of the sample while the $j_{specific}$ is the catalytic activities of each site.

Chapter 4 $Pt_{1-x}Ir_x$ ($0 < x < 0.3$) RDE on NSTF-coated GC Disks

This chapter presents RDE data for $Pt_{1-x}Ir_x$ ($0 < x < 0.3$) on GC disks coated with 3M Company's NSTF material. The majority of the work in this chapter has been published ([115]).

4.1 Experimental Procedure

4.1.1 Preparation of Glassy Carbon (GC) Disks

A series of 5 mm diameter GC disks, (from Tokai Carbon) were polished with a 0.05 µm polishing solution (#40-6353-006 alumina slurry on a #40-7212 microcloth pad from Buehler Inc.) to produce a mirror-like surface finish. 3M's NSTF support was then grown on the polished and cleaned surface of some of the GC disks using the same methods described in previous publications [60], [61], [116]. The NSTF growth process was done at 3M's facility. The GC disks were polished and prepared at Dalhousie, they were sent to the 3M Company for the NSTF growth before returning to Dalhousie for catalyst deposition and characterization (Figure 4-1).

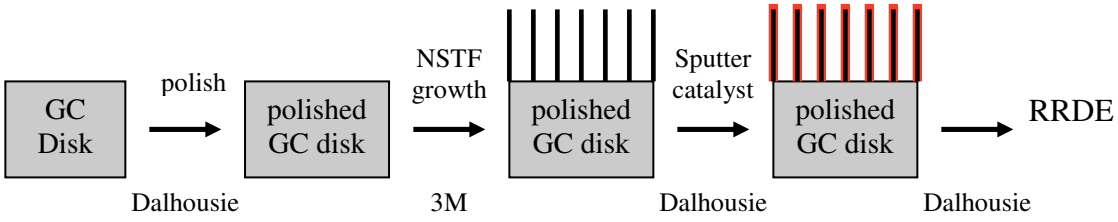

Figure 4-1 Diagram of the scheme used to grow NSTF on GC disks for RRDE measurements

4.1.2 Sputtering of Pt and Pt-Ir Layer Films

The catalyst samples were prepared using a Corona Vacuum Coaters V3T multi-target magnetron sputtering machine. Detailed information about this apparatus and its operation can be found elsewhere [94], [96]. During deposition, the chamber pressure was kept at 0.8 mTorr with an Ar flow of 2.3 standard cubic centimeters per minute (sccm) and substrates were mounted on a rotating table. The sputtering targets (Pt and Ir) were covered with different masks during the deposition – a constant mask over the platinum target designed to produce a constant film thickness across the substrates on the rotating substrate table and a "linear out" mask over the Ir target designed to deposit a linear gradient of Ir across the substrates. In this work, two samples were prepared: The first sample contained only Pt (constant loading of 0.16 mg/cm^2) deposited across the substrate track. The second sample contained fourteen alternating layers of Pt (0.16 mg/cm^2 constant loading) and Ir (from 0.01 to 0.063 mg/cm^2 linear gradient), giving an overall bulk composition of $Pt_{1-x}Ir_x$ ($0 \leq x \leq 0.33$). The total platinum loading was the same for both samples. Figure 4-2 shows a schematic diagram of the $Pt_{1-x}Ir_x$ sample.

During deposition of the constant Pt films, the Pt target was covered with a constant mask and operated at 50 W for 45 minutes. During deposition of the $Pt_{1-x}Ir_x$ films, the Pt target was covered with the same constant mask used for the constant Pt spread and the Ir target was covered with a "linear out" mask. When the deposition of the $Pt_{1-x}Ir_x$ films began, the Pt target was first turned on at 50 W and operated for 3 minutes before being switched off. After the Pt target was switched off, the Ir target was turned on at 50 W and operated for 3 minutes then switched off. The substrate table continued to rotate during sputtering. This process of alternating Pt and Ir targets was repeated 14 times to deposit 14 bi-layers

containing a constant amount of Pt and a linear gradient of Ir. After 14 bi-layers were deposited, the Pt target was turned on and operated at 50W for additional 3 minutes to create a top-layer of Pt and ensure that the overall Pt loading was the same as that of constant Pt samples. Both composition samples were deposited on smooth (mirror polished) and NSTF-coated GC disks in order to examine their electrochemical response with RRDE techniques. It is essential to realize that the layer thickness of Pt and Ir on the NSTF is reduced by a factor similar to the roughness factor introduced by the NSTF (approximately 10). For an example, if 5 nm planar-equivalent layers were deposited on flat substrates (i.e. like Figure 4-2), then the layer thicknesses of the same film deposited on the NSTF supports would be approximately 0.5 nm if the material coats that NSTF as smooth layers. This means that the materials being tested are not the same even though they have the same overall composition.

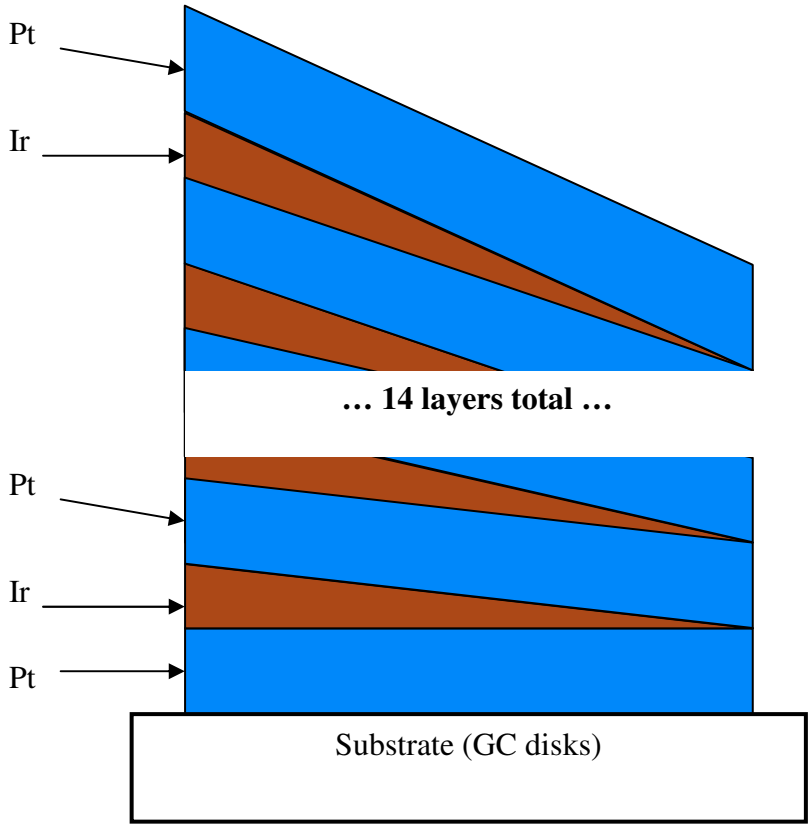

Figure 4-2 A schematic diagram of Pt-Ir films showing 14 alternating layers of constant Pt and Ir wedges sputtered onto the substrate. The layered films were capped with 5 nm of Pt.

4.1.3 Film Mass and Thickness

The mass of material deposited was determined by weighing pre-weighed aluminum disks placed along the sputtered region after sputtering. The planar thickness of the depositions was measured with a Dektak 8 profilometer (Veeco Instruments Inc.) on a silicon wafer substrate that was partially covered by tape during sputtering. The tape was removed after deposition to reveal a fresh surface underneath. This surface was used as a

baseline for the thickness measurements. During the Dektak measurement, the stylus radius was set to 12.5 µm. The accuracy of the measurements was typically +/- 5 nm.

4.1.4 Electrochemical Measurements

All of the rotating ring-disk electrode (RRDE) measurements were performed using a Pine electrochemical system (AFMSRX rotator and AFCBP1 bipotentiostat) in a single-compartment glass cell (#6961-64 from ACE glass) with Pt-wire as the counter electrode and a Cl^- free Koslow mercury/mercurous sulfate (MMS) reference electrode. The electrolyte was ~125 mL of 0.1 M $HClO_4$, prepared from doubly distilled 70 wt% stock solution (GFS Chemical) and 18 MΩ nano-pure water from a Barnstead NANOpure Diamond system (Model D11911). Different gases were introduced into the electrolyte via a 2 µm fritted tube (#9435-10 from Ace Glass) Extreme care was taken to maintain clean glassware, cell parts and samples during handling. The RRDE response of a 1 µm polished Pine Pt (polycrystalline) RDE electrode was measured weekly to confirm that the equipment and materials used were able to generate performance curves in agreement with state-of-the art measurements from other researchers. The potential of the Hg/Hg_2SO_4 reference electrode was calibrated versus a reversible hydrogen electrode (RHE) arrangement for each individual disk measurement. All of the potentials discussed in this paper are potentials vs. this RHE calibration potential. All measurements were carried out at ambient temperature.

4.1.5 Disk Mounting Tool

A home-made mounting device was used to facilitate mounting and alignment of the NSTF-coated disks into the RRDE tip while minimizing damage to the whisker surfaces. The device was made from polyetherimide (Ultem 1000) and had three cylindrical holes with the diameters and depths shown in Figure 4-3. Each of the three holes was also drilled through with a 4.5 mm bit as shown in the side view in Figure 4-3.

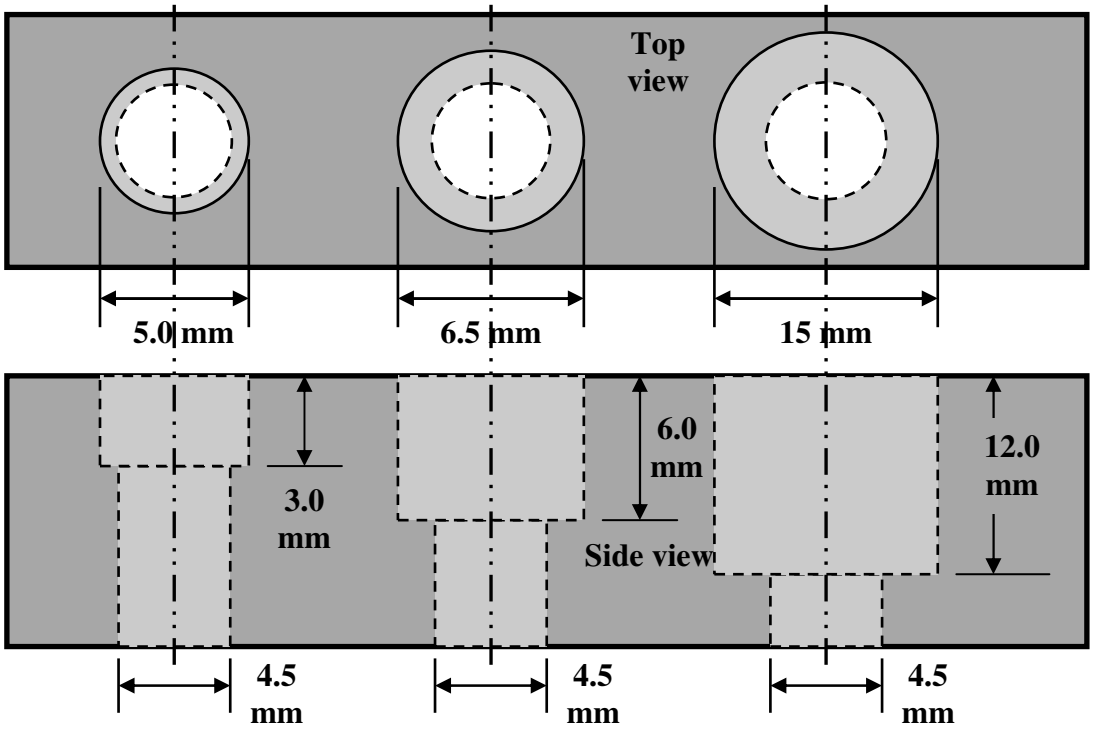

Figure 4-3 Dimensions of the disk mounting tool

The NSTF-coated disks were mounted onto the RDE tip in three steps, shown in Figure 4-4. The first hole of the mounting tool has the same diameter as the GC disk, 5 mm, and was drilled to a depth of 3 mm. A NSTF-coated GC disk was partially inserted into a Teflon u-cup by placing the disk in this hole with the coated surface down (step 1 of Figure 4-4). The outer edge of the disk surface was in contact with the recessed flat face

of the countersunk hole, so some damage occurred; this was, however, restricted only to the material within 0.25 mm of the edge. The second hole was used to push the U-cup down onto the disk and to align the RRDE assembly (step 2 of Figure 4-4). Finally, the third hole was used to completely insert the U-cup into the RRDE assembly (step 3 of Figure 4-4). The morphology of the catalysts deposited on the NSTF-GC disks was examined by a Hitachi S-4700 SEM and will be discussed in detail later.

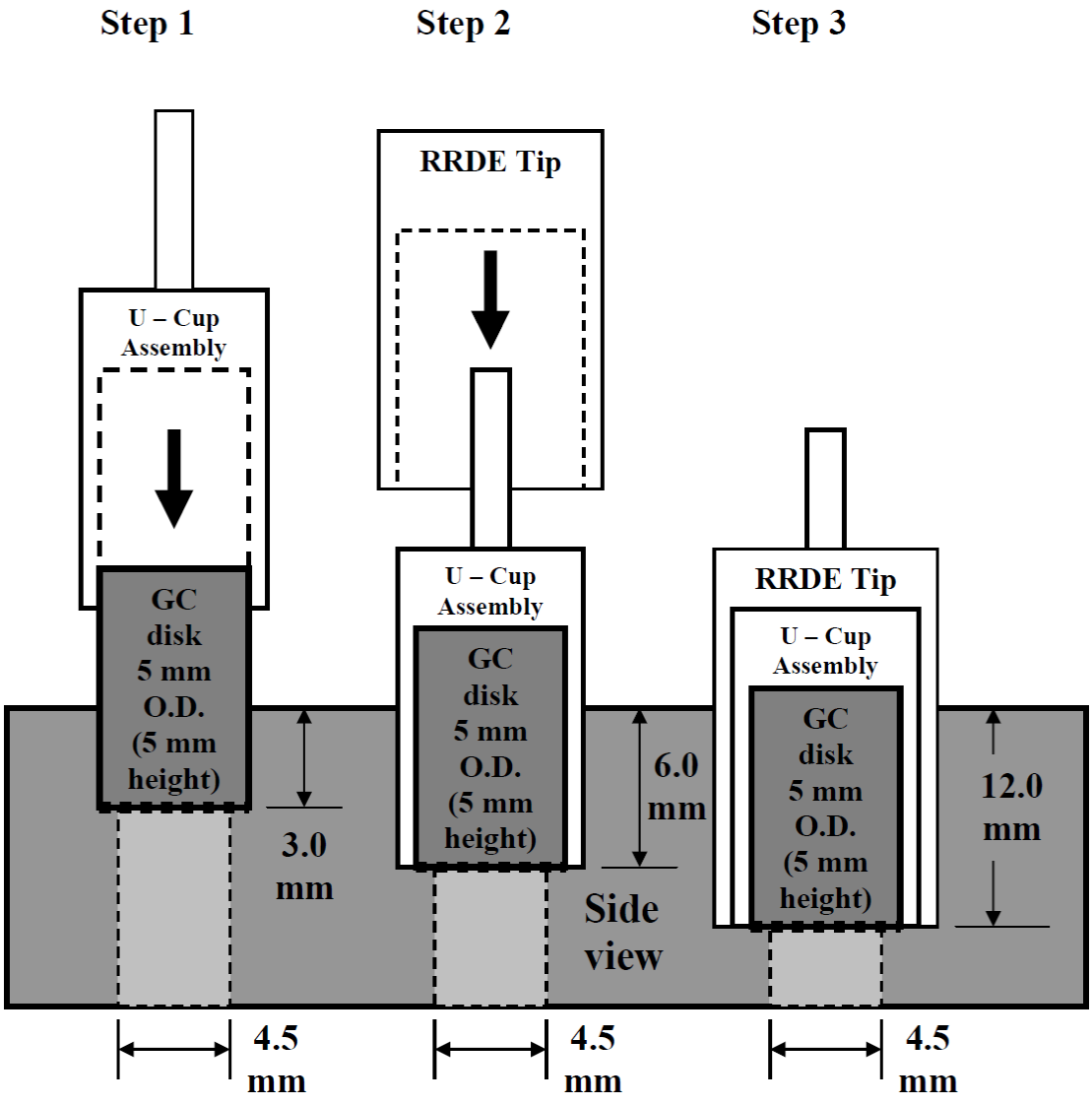

Figure 4-4 NSTF-coated GC disk is inserted and aligned to the RDE tip in three steps.

4.1.6 Electrochemical Measurement Procedure

As stated in previous sections, all of the RRDE disks and the Pt ring were first electrochemically cleaned by sweeping their potential between 0.05 and 1.20 V at 500 mV/s in Ar-saturated electrolyte (by purging the solution with Ar at 50 sccm for 15 minutes) until steady state cyclic voltammograms (CVs) were obtained. Slow rate CVs were then acquired in the same potential range at 50 mV/s. Oxygen reduction scans were then recorded at the same sweep rate (50 mV/s) for two full cycles while purging the solution with O_2 at a flow rate of 50 sccm. The ORR measurements were performed at 400, 900 and 1600 rpm. The data obtained for different rotation rates showed the same trends and thus only the 900 rpm data is discussed in this paper. All measurements were performed at room temperature.

4.2 Results and Discussions

The mass and thickness of the sputtered films as a function of distance along the sputtered region are shown in Figure 4-5. Both types of films were sputtered onto five mirror-polished GC disks and five NSTF-coated GC disks positioned along the sputtering region. The positions of the disks are shown as labeled circles at the bottom of Figure 4-5b. Figure 4-5a shows the mass of the films, measured on pre-weighed aluminum disks, as a function of the distance along the sputtered region for both the constant Pt and $Pt_{1-x}Ir_x$ films. The constant Pt film has a constant mass profile (0.165 mg/cm^2) while the mass profile of the $Pt_{1-x}Ir_x$ increased linearly (from 0.167 to 0.23 mg/cm^2) along the sputtered track due to increasing Ir content. The Ir ratio (x in $Pt_{1-x}Ir_x$) of the $Pt_{1-x}Ir_x$ composition spread was calculated for each mass measurement – these values are shown in Figure 4-

5a with the scale at the right hand side of the figure. The Ir content increased from x = 0.05 (corresponds to RRDE disk #1 location) to x = 0.3 (RRDE disk #5) along the sputtered track.

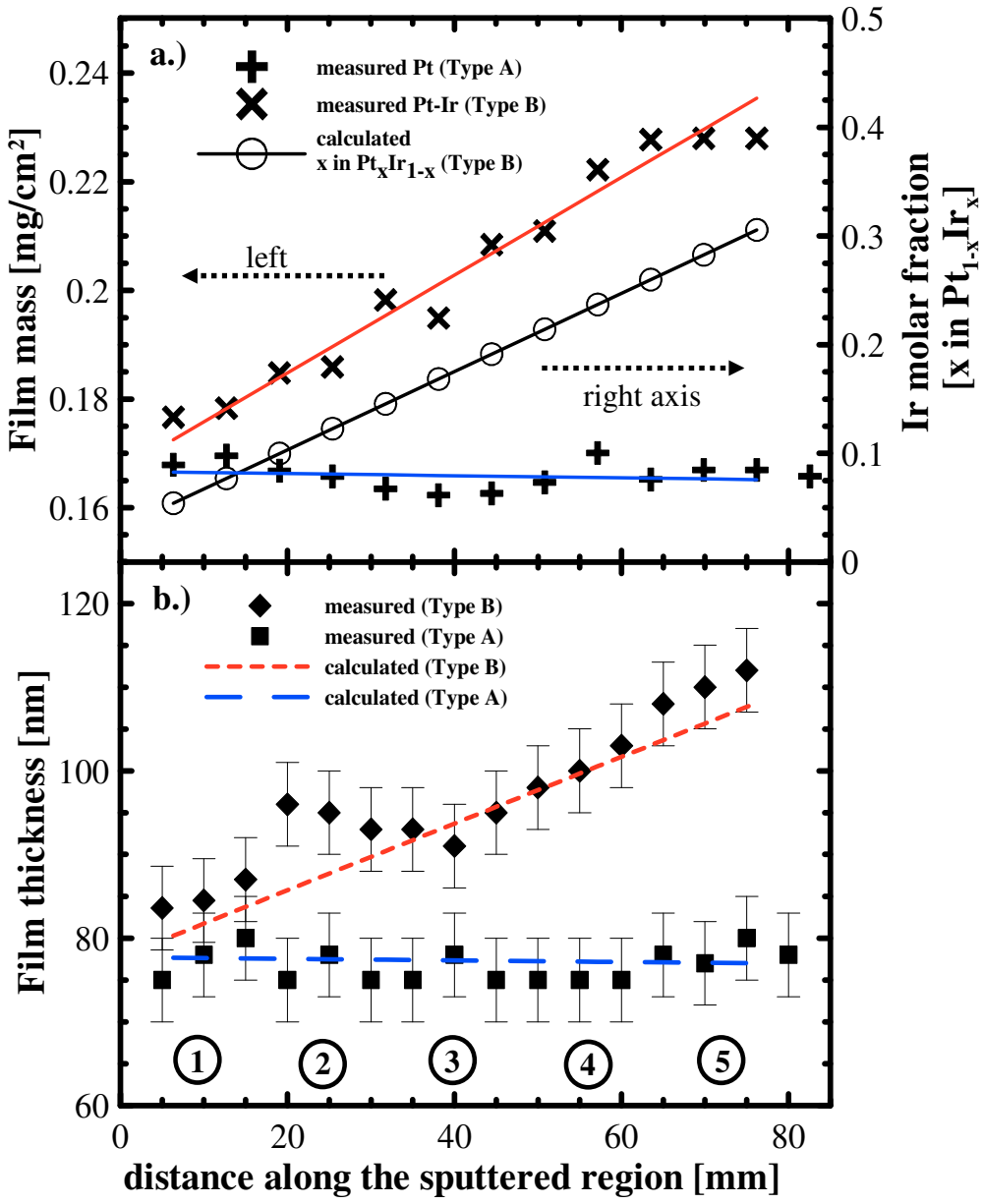

Figure 4-5 The mass and thickness of the sputtered films along the sputtering track compared to the positions of the GC disks, shown in circles at the bottom. The measured mass of Type A and B films are shown in (a), giving x values between 0.05 and 0.3 for $Pt_{1-x}Ir_x$. The mass data were then used to calculate the thickness of the films (assume 100% bulk density), shown in (b) to compare with measured thickness by DekTak profilometer.

The measured mass data in Figure 4-5a for both types of films were used in a linear curve-fit with the results shown in the same figure. The curve-fit results were then used to calculate the film thickness with the assumption that the material sputtered at 100% bulk density. The calculated thicknesses are shown in Figure 4-5b as dashed lines. Figure 4-5b also shows the measured thickness data for both types of films compared with the calculated values. It is apparent that the sputtered Pt had the same density as bulk Pt because the measured thickness data of sputtered Pt in the constant Pt films agreed with the calculated thickness. The measured thickness data of the $Pt_{1-x}Ir_x$ films also agreed with calculated values well. The agreement between the calculated and measured thickness for $Pt_{1-x}Ir_x$ films suggests that the sputtered Pt-Ir films have near-bulk density. Note that the $Pt_{1-x}Ir_x$ films have the same amount of Pt as the constant Pt films, have 14 alternating layers of Pt and Ir and are capped with a layer of Pt, which makes 15 layers of Pt in total. Each layer of Pt was ~5 nm (planar equivalent) thick, or ~0.011 mg/cm^2 because they were sputtered with identical settings (50 W at 0.8 mTorr for 5 minutes). The actual layer thicknesses depend on the roughness of the substrate used.

The morphology of the sputtered $Pt_{1-x}Ir_x$ films on NSTF-coated GC disks was examined by SEM and is shown in Figure 4-6. All disks of both constant Pt and $Pt_{1-x}Ir_x$ films on NSTF-coated GC disks were also examined post-RRDE and showed similar morphology. Figure 4-6a shows that only the edges of the disks suffered minimal damage when mounted into the RRDE tips. The home-made mounting tool, shown in Figure 4-3a, only makes physical contact with the outer rim (~ 0.25 mm wide ring) of the GC disk thereby

leaving most of the GC disk area intact. In the higher magnification SEM images shown in Figures 4-6b and 4-6c, the surface of the disks were densely covered with large numbers of NSTF whiskers. Figure 4-6d shows that the catalysts sputtered on the NSTF whiskers formed nanometer-size "whiskerettes" that coated the NSTF support evenly.

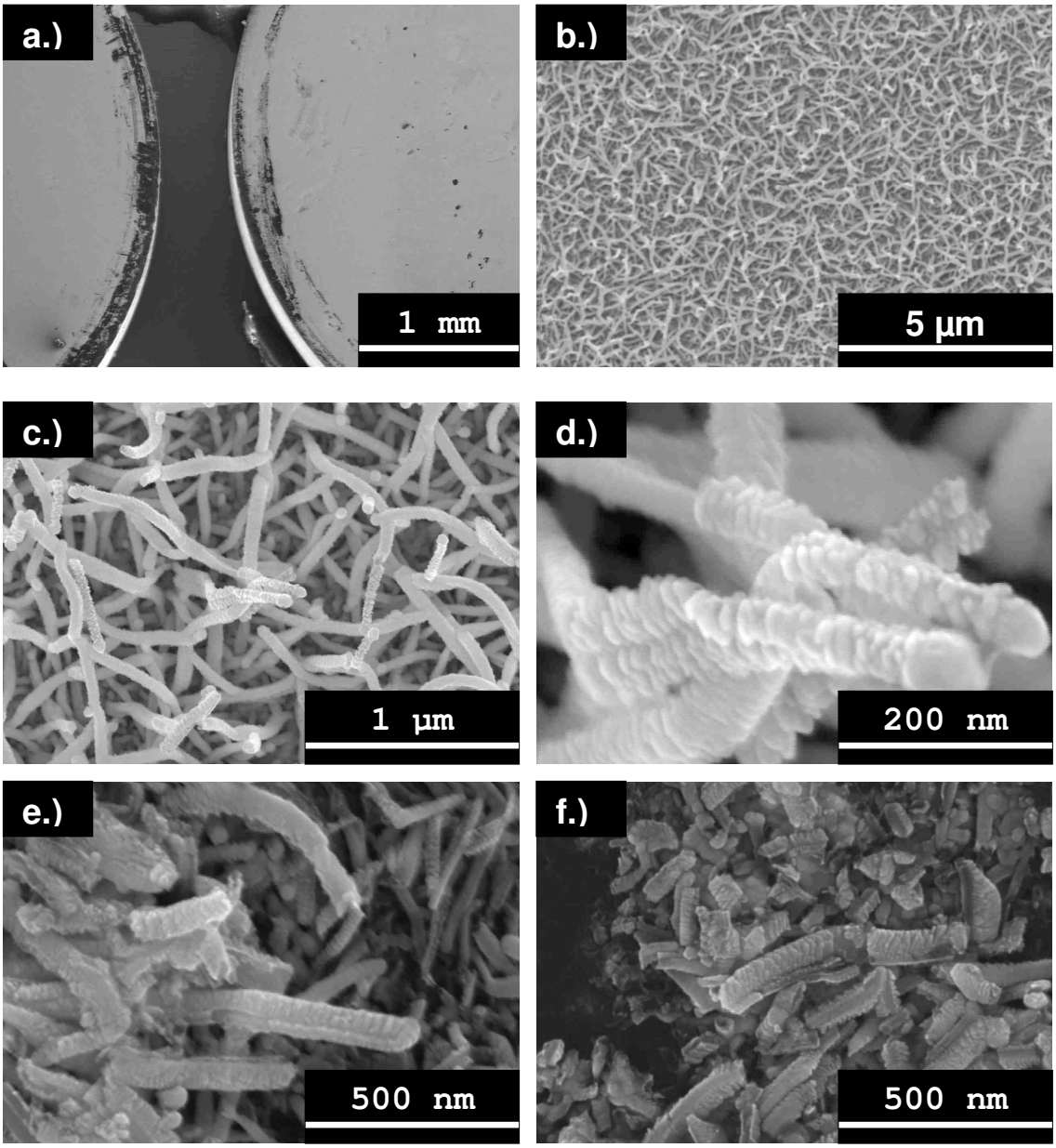

Figure 4-6 Post-RDE SEM images of sputtered Pt-Ir films on NSTF-GC disks. The Pt-NSTF films remained intact (a, b). The NSTF whiskerettes are visible at magnification (c, d). Crushed catalyst-coated NSTF remain at the rim of the disk (e, f)

The sputtering of catalyst on NSTF materials and the formation of whiskerettes were examined in detail in previous publications [64], [18], [116]. Note that SEM images of the catalyst on NSTF-coated GC disks were taken after RRDE experiments. Since some of the disks underwent 200 cycles with the potential swept between 0.05 and 1.20 V_{RHE} (50 mV/s) that typically takes ~3 hours with more than 130,000 rotations in the electrolyte (900 rpm). This shows the NSTF material coated directly on the GC disks was able to withstand prolonged exposure to liquid electrolyte under rotation conditions without falling off the disk. SEM images in Figures 4-6e and 4-6f collected close to the edge of the disk show that some catalyst-coated NSTF remained, although it had been crushed / flattened. It is likely that there was some contribution to catalytic performance from the small region that was damaged during disk mounting.

Cyclic voltammograms of a polycrystalline Pt electrode and sputtered Pt on GC disks are shown in Figure 4-7a (mirror-polished disks) and 4-7b (NSTF-coated disks). The sputtered Pt films on mirror-polished surfaces had larger H adsorption / desorption peaks than the polycrystalline Pt disk (Figure 4-7a), indicating a larger surface area, presumably due to somewhat increased surface roughening. The SEF value determined for the polycrystalline Pt disk electrode was 1.8 cm^2_{Pt}/cm^2_{planar} while the sputtered Pt and Pt/Ir films on mirror-polished GC disk shown in Figure 4-7a both had SEF values around 2.1 cm^2_{Pt}/cm^2_{planar}. The CVs of the sputtered Pt and Pt/Ir samples on NSTF-coated GC disks are compared in Fig 4-7b. The catalysts deposited on NSTF-coated GC disks have a much larger active Pt surface area than catalysts deposited on the flat GC disk substrates.

Platinum deposited on the mirror-polished GC disk gives an SEF of ~ 2.1 cm^2_{Pt}/cm^2_{planar} while on NSTF-coated GC disks this increased to ~ 14.2 cm^2_{Pt}/cm^2_{planar}. This is consistent with previous data that showed that the surface area on a NSTF-substrate is about 14-15 times higher than the planar area [18], [63], [64].

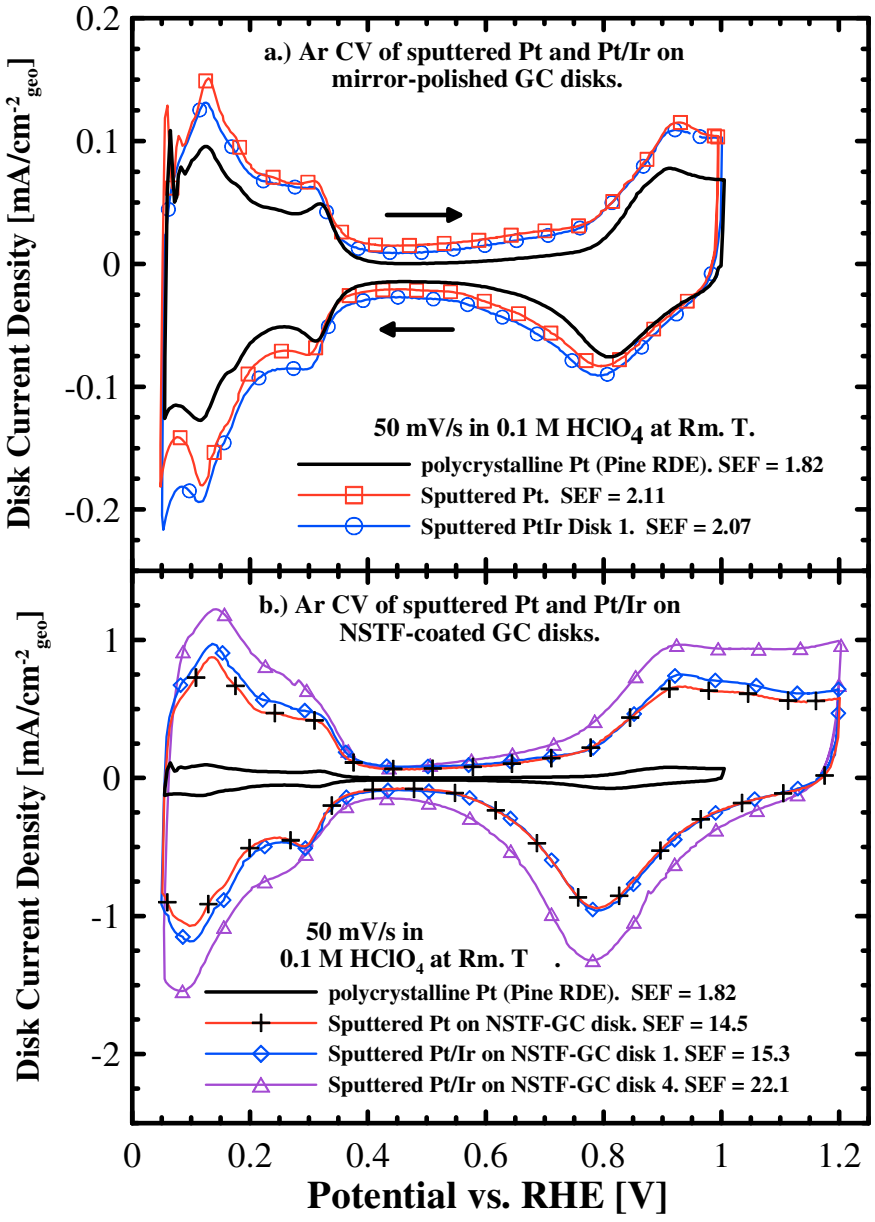

Figure 4-7 Ar CV of sputtered Pt and Pt-Ir on mirror-polished disks and a polycrystalline Pt disk (a) and on NSTF-coated disks (b)

The SEF values calculated for both films sputtered on both mirror-polished and NSTF-coated disks are plotted in Figure 4-8. The values calculated for the constant Pt film samples have no compositional change and are thus plotted against disk number (top horizontal axes) while the values for the $Pt_{1-x}Ir_x$ film samples are plotted against Ir content in the film (x in $Pt_{1-x}Ir_x$ - calculated from the sputtering mass data shown in Figure 4-5a. The disk positions of constant Pt samples shown in both Figures 4-8a and 4-8b correlate with the composition data for equivalent disks for the $Pt_{1-x}Ir_x$ samples. For example, disk #4 of the constant Pt run was positioned at the same location along the sputtering track as disk #4 for the $Pt_{1-x}Ir_x$ deposition which had a composition of $Pt_{0.75}Ir_{0.25}$ (i.e. x = 0.25 in $Pt_{1-x}Ir_x$).

Figure 4-8a compares the SEF values calculated for the films sputtered on NSTF-coated GC disks. The SEF values for Pt range between 13.5 and 14.5 cm^2_{Pt}/cm^2_{planar} as discussed earlier. Figure 4-8a shows that the addition of Ir to the film increases the SEF further for samples deposited on NSTF-coated GC disks, reaching a maximum of 22 cm^2_{Pt}/cm^2_{planar} at x = 0.25 in $Pt_{1-x}Ir_x$. The surface area of the deposited film on NSTF is controlled by the surface area of the whiskerettes formed. The surface area of the whiskerettes increases as the amount of material increases because the whiskerette volume increases. The surface area measured electrochemically (i.e. the SEF) is likely predominantly that of the top Pt layer spread over the whiskerettes. Thus the SEF should increase with the total amount of material deposited [64]. Although the expected measured electrochemical surface area increase could in principle be modeled, we choose not to do so as the complexity of such

a model (selection of whiskerette shape to use, relative surface area contributions from different crystal faces that may be present etc.) is too high. The SEF values for the $Pt_{1-x}Ir_x$ catalyst pass through a maximum at x = 0.25, suggesting that there may be an optimum Pt-to-Ir ratio for $Pt_{1-x}Ir_x$ catalyst at which high surface area whiskerettes are formed.

The variations in SEF values from 1.0 to 2.1 for catalysts deposited on mirror polished disks shown in Figure 4-8b could be the result of sputter deposition angle. In Figure 4-8a and b, the Pt disk numbers were shown at the top horizontal axis. These disk numbers are the same as those shown in Figure 4-5. In other words, Pt disk #1 was centered at ~ 9 mm along the sputtering track near the inner edge of the sputtering track while disk #5 was centered near the outer edge of the sputtering track. During sputtering, it is apparent that disks #1 and #5 were positioned "off-axis" from the sputtering plasma and thus could be impacted by the glancing angle deposition (GLAD) effect. GLAD is an area of intense academic and industrial research and could have many applications in the semiconductor industry [117-119]. The high SEF of "off-axis" disks shown in Figure 4-8b (Pt disk #1 and #5) could be the result of GLAD-type deposition that incurred higher roughness. This trend could be subtle enough that it was not visible via the SEM image comparisons.

The $Pt_{1-x}Ir_x$ catalysts deposited on mirror-polished GC disks show the same SEF trend as those of pure Pt disks, suggesting that the $Pt_{1-x}Ir_x$ catalysts on mirror-polished disks were subject to the same GLAD effect. However, on NSTF-coated disks, the $Pt_{1-x}Ir_x$ catalysts show a distinctive trend different from pure Pt as discussed earlier.

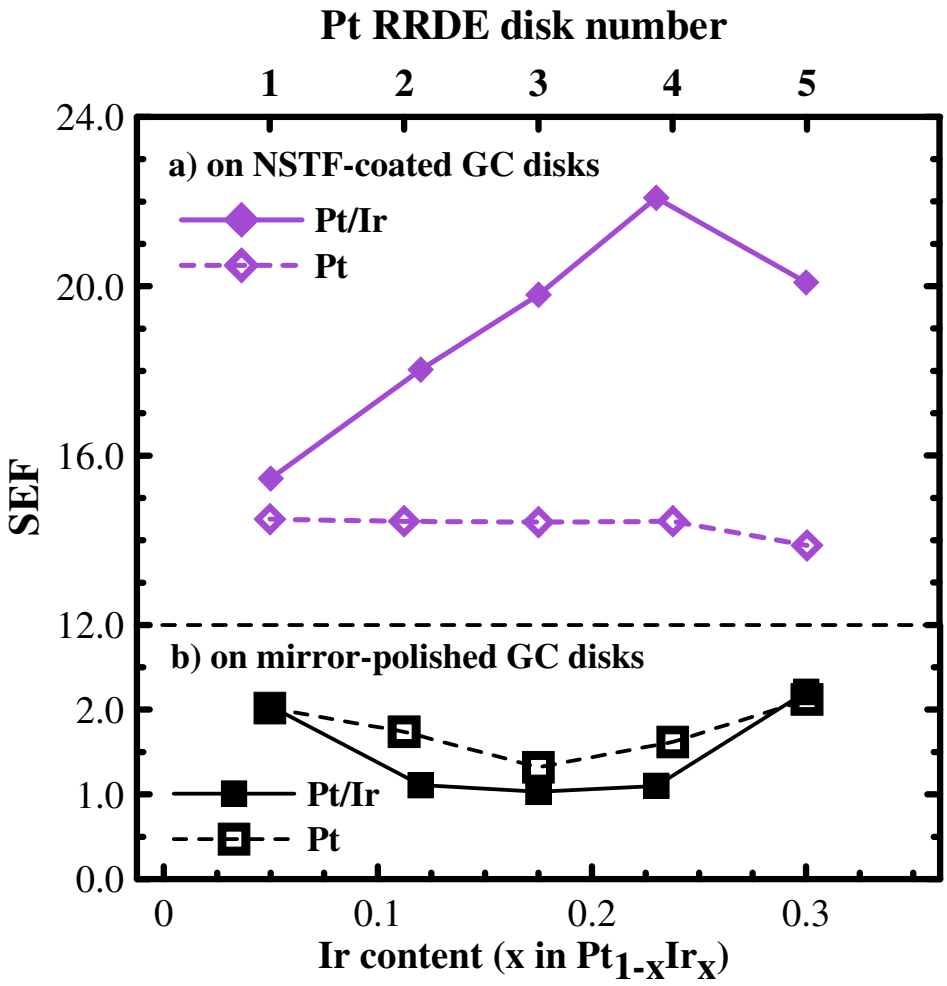

Figure 4-8 SEF values for sputtered catalysts on NSTF-GC disks (a) compared to those for mirror-polished GC disks (b).

ORR curves for selected Pt and Pt-Ir samples are shown in Figure 4-9. All of the measurements presented in Figure 4-9 were made between 0.05 ~ 1.20 V_{RHE} and all current densities shown were measured at 900 rpm with a sweep rate of 50 mV/s, a high sweep rate, in order to prevent excess Pt oxide buildup in the high potential region. Note that all of the measurements shown reached the theoretical mass-transfer limited current which, according to the Levich equation [114], [120], is 4.5 mA/cm^2 for oxygen diffusion in 0.1 M $HClO_4$ electrolyte at room temperature at 900 rpm. The Levich analysis

presented in Chapter 3 regarding $j_{diff\text{-}lim}$ and $j_{kinetic}$ of RDE measurements is valid here since the NSTF-coated layer is less than 1 µm thick at the RDE surface, much less than the hydro-dynamic boundary layer thickness (t_{HDBL}). In RDE, t_{HDBL} is roughly defined as the thin layer of fluid dragged by the rotating disk at the electrode / electrolyte interface [105]. For 0.1 M $HClO_4$ at ω = 100 rad/sec (~ 950 rpm), t_{HDBL} = 360 µm [105].

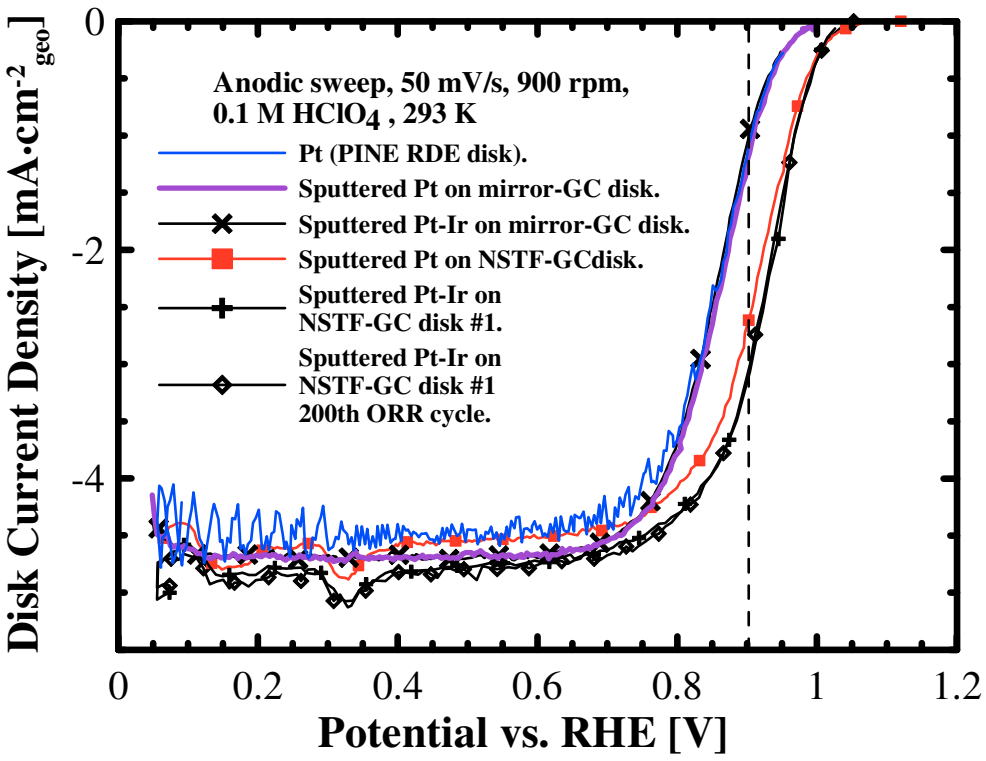

Figure 4-9 ORR measurements of the sputtered catalysts on different substrates.

As shown in Figure 4-9, the onset potentials (the potential at which measurable current flow occurred) for the catalysts deposited on flat surfaces, including the polycrystalline Pt and sputtered Pt/Pt-Ir materials on mirror-polished GC disks, were 50-100 mV lower than the onset and half-wave potentials for catalysts deposited onto NSTF-coated GC disks. This is a direct result of the increased catalyst surface area generated when Pt is deposited onto NSTF-coated GC disks. Several Pt and Pt-Ir samples deposited onto the NSTF-

coated GC disks were selected for 200-cycle ORR at 900 rpm and 50 mV/s potential sweep rate to see the effects, if any, of prolonged potential cycling on the activity. The result obtained for $Pt_{1-x}Ir_x$ disk #1($Pt_{0.95}Ir_{0.05}$) is shown in Figure 4-9. It is apparent that extended potential cycling and prolonged exposure to liquid electrolyte had no effect on the catalytic activity of samples deposited onto the NSTF-coated GC disks as the ORR performance for the 200^{th} cycle was essentially the same as was seen for the first cycle.

The kinetic current densities of the ORR measurements shown in Figure 4-9 were calculated and plotted as Tafel-style graphs in Figure 4-10. The details of calculations were discussed in earlier sections. While Tafel plots of ORR catalysts are typically compared at potentials between 0.875 and 0.95 V in numerous publications (e.g. [114], [120]), in this thesis, the Tafel plots were compared at a higher potential region, between 0.95 and 1.00 V, due to the high current density of NSTF-supported samples at 0.875~0.95 V. As discussed earlier, Tafel plot comparisons are best made in regions where the current density is less than half of the diffusion-limited current level so that the uncertainties associated with mass-transport corrections can be minimized. Figure 4-10 shows all of the plots in Figure 4-9 in the kinetic region in two formats: planar current density, j_{planar} (plotted with dashed lines) and area specific current density, $j_{specific}$ (plotted in solid lines). Both sets of values were plotted to demonstrate the impact of different supports. The catalyst supported on NSTF-coated GC disks, shown in Figure 4-10a, has much higher planar current density (~ 1 mA/cm^2_{planar} at 0.97 V) than the mirror-polished GC disks (0.15 mA/cm^2_{planar} at 0.97 V) shown in Figure 4-10b. However, after

normalizing the data by the active Pt surface area, all samples had similar specific current densities (~ 0.07 mA/cm^2_{Pt} at 0.97 V) and Tafel slopes (~ 60 mV/decade).

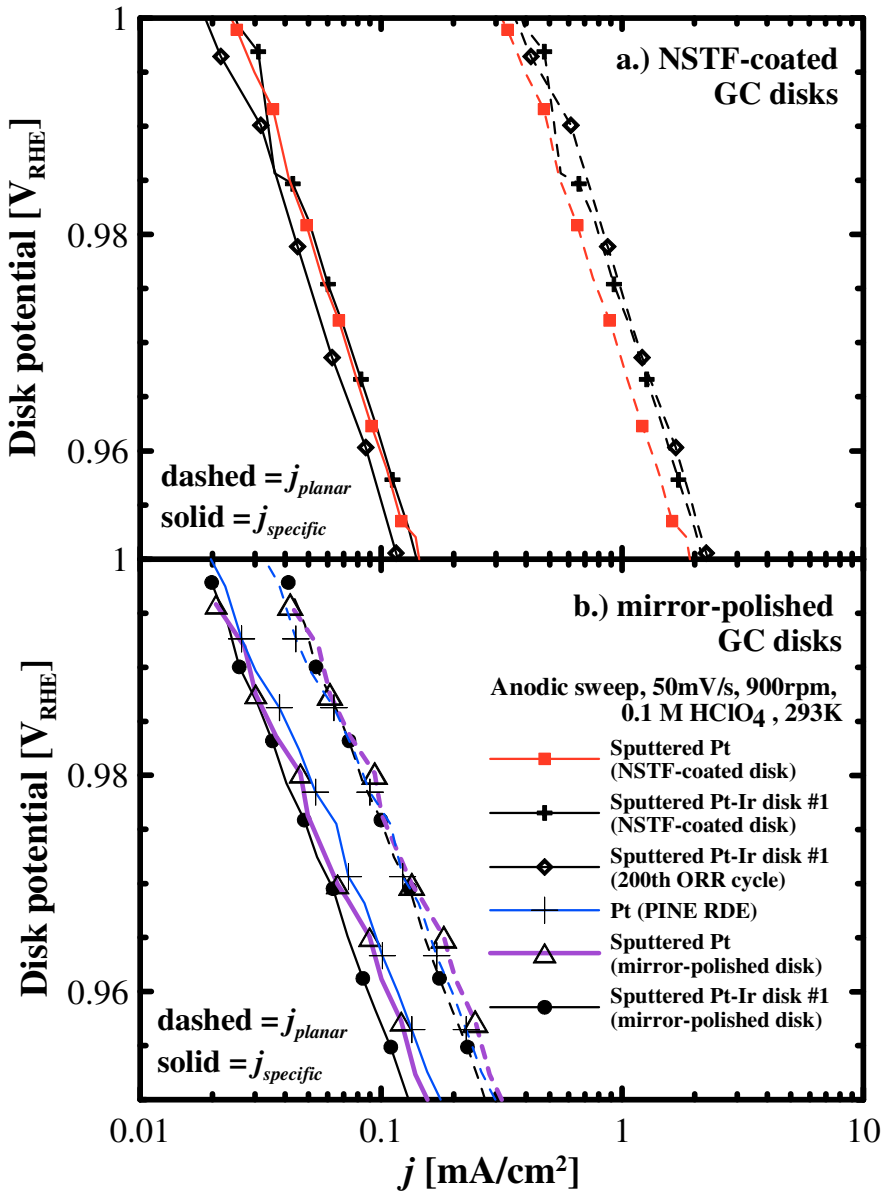

Figure 4-10 Tafel plots of NSTF-GC disks (a) and mirror-polished GC disks (b). The dashed lines shows planar current density data; the solid lines show the ORR performance per unit catalyst area.

Figure 4-10a includes data for Pt-Ir disk #1 after 200 CV cycles. These data show that extended potential cycling had no impact on ORR kinetics of NSTF-supported materials

because the planar/specific current densities and Tafel slopes were unchanged after extended potential cycling. Figure 4-10 also shows that the specific current densities for catalyst films on mirror-polished and NSTF-coated GC disks were the same as those measured on the polycrystalline Pt disk, suggesting that the active ORR catalyst in all four types of catalyst/film combinations was Pt.

The kinetic current densities at 1.0V for the constant Pt and $Pt_{1-x}Ir_x$ composition spreads, sputtered on both types of supports (mirror-polished and NSTF-coated GC disks), are compared in Figures 4-11 and 4-12. The plots are presented in the same format as those of Figure 4-8, with data from constant Pt films plotted against disk number and $Pt_{1-x}Ir_x$ films plotted against Ir content. Figure 4-11 compares the activities of the catalysts on mirror-polished disks and Figure 4-12 shows the comparison on NSTF-coated GC disks. The figures also present both planar and specific current densities for comparison. Figure 4-11a shows the planar current density (j_{planar}) of the constant Pt disks ranged from 0.033 to 0.045 mA/cm^2_{planar} while the $Pt_{1-x}Ir_x$ disks ranged from 0.022 to 0.045 mA/cm^2_{Pt} at 1.00 V_{RHE}. After conversion to specific current densities ($j_{specific}$ from Eqn. 4) both materials show the same performance per measured area of platinum, with specific current densities around 0.02 mA/cm^2 at 1.0 V_{RHE}. There was little difference in performance between the two types because the $Pt_{1-x}Ir_x$ disks have a ~5 nm (planar) Pt over-layer on top of the alternating Pt-Ir layers which may have masked the impact from Ir.

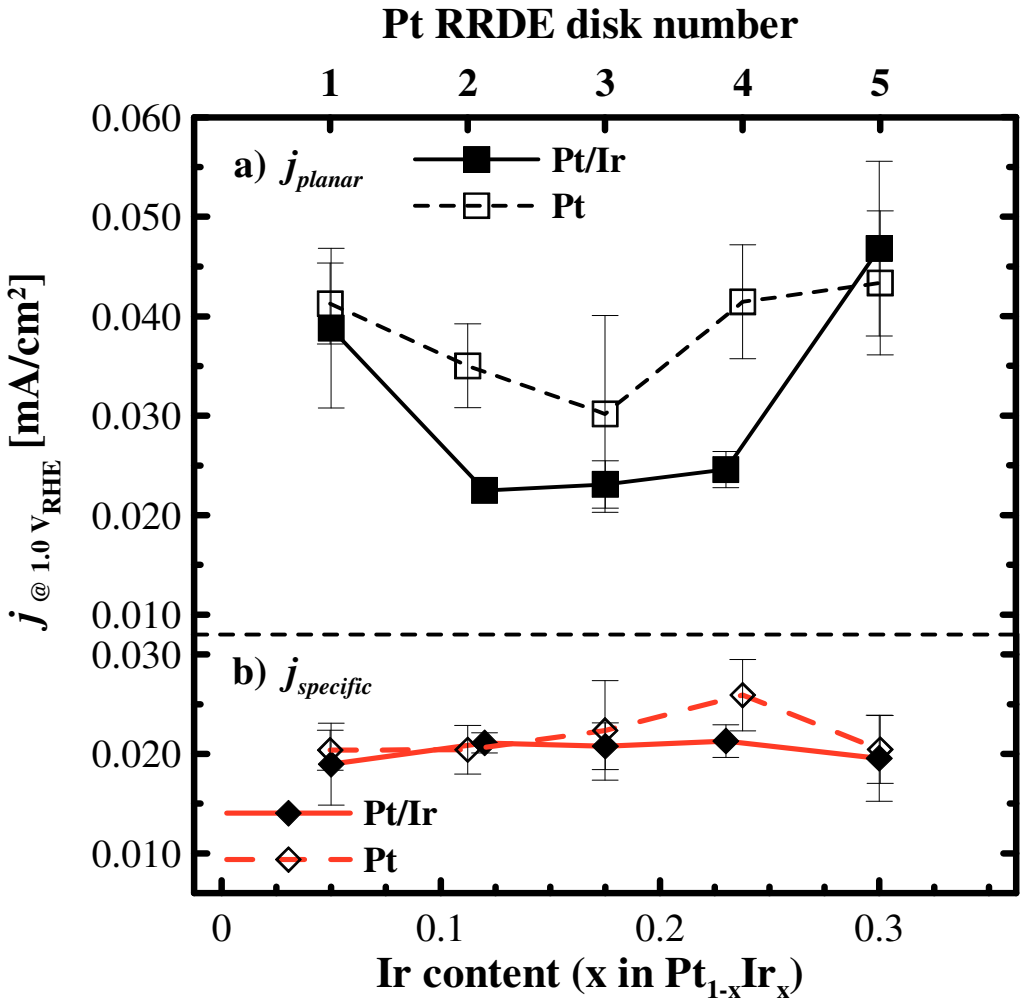

Figure 4-11 Kinetic current density data for sputtered Pt and Pt-Ir catalysts on mirror-polished GC disks at 1.0V_{RHE}

Figure 4-12 shows the activities of both the Pt and the Pt-Ir composition spread on NSTF-coated GC disks. Figure 4-12a shows that the planar current density (or j_{planar}) of the constant Pt disks ranged between 0.25 to 0.32 mA/cm$^2_{planar}$ while that of the $Pt_{1-x}Ir_x$ disks increased as the SEF increased, from 0.33 (x = 0.05) to 0.45 mA/cm$^2_{planar}$ (x = 0.25) at 1.00 V_{RHE}. After normalizing for the active Pt surface area (Figure 4-12b), both constant Pt and $Pt_{1-x}Ir_x$ disks showed specific current densities ($j_{specific}$) around 0.02 mA/cm$^2_{Pt}$ at 1.0 V_{RHE} for all disks, the same as the specific kinetic current densities of the catalyst

coated, mirror-polished GC disks shown in Figure 4-11. It is likely that the planar current density of $Pt_{1-x}Ir_x$ catalyst increased with increasing Ir content because of an increase in surface roughening of the platinum on the NSTF support. This material also had a 5 nm Pt "capping" layer, however this was a 5 nm planar equivalent capping layer. The thickness of this layer on a deposit on mirror-polished GC disks was likely close to 5nm. The catalyst deposited on NSTF had a much higher surface area (10 ~ 15 times higher than a deposit on mirror-polished substrates) than on a flat surface and thus the thickness of the capping layer on the whiskerettes (the nano-scale catalyst particles deposited on the NSTF whiskers) was likely closer to 0.5 nm. If Ir had an impact on catalytic activity, then this was likely thin enough that the effect from the Ir would be observed. The data in Figures 4-11 and 4-12 therefore imply that the active catalytic surface for both types of films was essentially the same regardless of substrate and thus Ir was just a spectator for ORR.

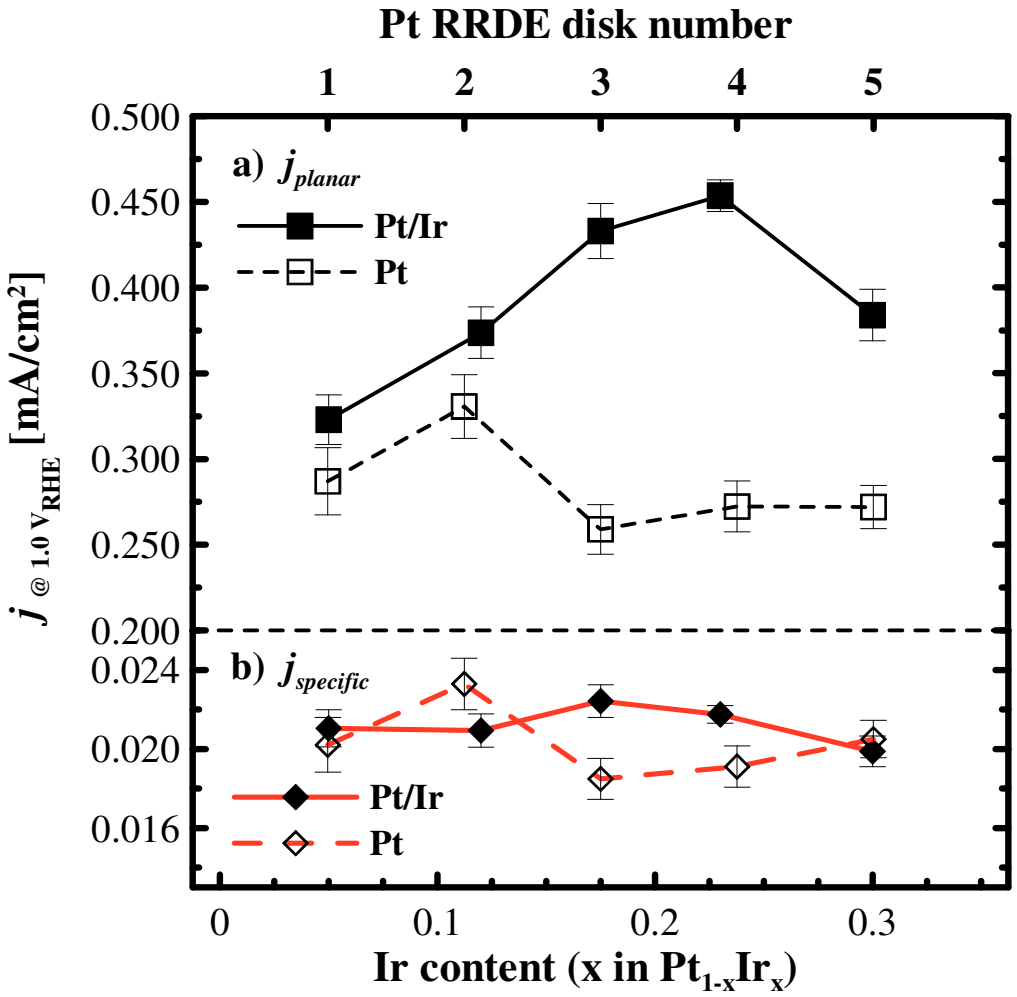

Figure 4-12 Kinetic current density data for Pt and Pt-Ir catalyst sputtered on NSTF-coated GC disks at 1.0V_{RHE}

Ideally, the trends observed in the RRDE experiments should also be seen for fuel cell measurements made with the same catalyst through MEA fabrication and testing. However, RRDE experiments of sputtered films on GC disk surfaces, which can accurately measure the catalytic kinetic current density, cannot examine the impact of the support. It is clear from the examples presented here that the support can play a large role in ORR performance. In order to more reliably assess the impact of compositional and other changes on fuel cell performance without going to full sized MEA preparation and

testing, R(R)DE measurements should be made on a catalyst support that is as close as possible to the support that would be used in a fuel cell. The techniques described here for NSTF deposition on GC disks and subsequent overcoating with catalyst can therefore provide better quantification of kinetic ORR parameters and thus a better indication of expected performance in a fuel cell. R(R)DE measurements such as these can therefore be used to reliably screen potential catalyst materials.

4.3 Chapter Summary and Conclusions

Layered $Pt_{1-x}Ir_x$ ($0 < x < 0.3$) and Pt were sputter-deposited onto 0.05 μm mirror-polished and NSTF-coated GC disks and were studied for ORR activity by RRDE. The constant Pt film had a thickness of ~ 75 nm (0.165 mg/cm^2) while the $Pt_{1-x}Ir_x$ film contained 14 alternating layers of constant Pt and Ir wedges with an over-layer of ~ 5 nm (planar-equivalent) Pt. The $Pt_{1-x}Ir_x$ composition spread had the same amount of Pt as the constant Pt film and was ~ 80 nm thick (0.175 mg/cm^2) at the thin end and ~ 115 nm thick (0.23 mg/cm^2) at the end with the highest Ir content ($x = 0.3$ in $Pt_{1-x}Ir_x$). The SEFs of polycrystalline Pt, sputtered Pt on mirror GC disks and NSTF-coated GC disks varies between 1.0 to 2.11 (depends on the sputtering angle) and ~14 cm^2_{Pt}/cm^2_{planar}, respectively. The SEF of $Pt_{1-x}Ir_x$ films on mirror-polished GC disks were similar to those of constant Pt films on mirror-polished GC disks By contrast, the SEFs measured for $Pt_{1-x}Ir_x$ catalysts sputtered on NSTF-coated GC disks increased from 15 to 23 cm^2_{Pt}/cm^2_{planar}, reaching a maximum at $x = 0.25$ (in $Pt_{1-x}Ir_x$).

During the ORR measurements, all of the catalyst / support combinations reached the theoretical diffusion-limited current densities. However, NSTF-supported catalysts reached these diffusion-limited current densities at a much higher potential than did mirror-polished supported catalysts. After normalizing the data for active Pt surface area, the specific current densities were all the same, regardless of support, and showed the same Tafel slopes. This implied that all of the catalyst / support combinations shared the same active catalytic ingredient, likely Pt. The high SEF measured on NSTF-supported catalysts on GC disks was due to the surface area enhancement (area about 14 ~15 times the planar surface area) provided by the NSTF support and the whiskerette growth mode. The trend of increasing SEF / current density with increasing Ir content for the $Pt_{1-x}Ir_x$ samples was probably caused by an increase in surface roughness of the nano-scale catalyst particles (whsikerettes) due to an increase in total deposited volume.

Several constant Pt and $Pt_{1-x}Ir_x$ samples supported by NSTF-coated GC disks underwent 200 cycles of ORR measurements, which typically take more than 3 hours and 130,000 rotations at 900 rpm, and showed no decline in activity, suggesting all the whiskers remained firmly attached to the disks. The post-RRDE SEM measurements of the GC disks showed the NSTF structures remained intact and the catalyst whiskerettes were clearly visible along the NSTF whiskers. All of this suggests that NSTF-coated GC disks are a viable alternative to the regular mirror-polished GC disks in screening catalyst activities because both the catalytic activities and the effects of high-surface area support can be examined in a single measurement. Also, catalysts deposited onto NSTF-coated GC disks via a physical vapor deposition (sputtering) method showed no impact of the

GLAD effect. This is compared with the same catalysts deposited onto mirror-polished disks located off-axis from the sputtering plasma, which showed significantly higher surface area (× 2 in some cases) than the disks located at the center of the sputtering track probably due to the roughening effect, GLAD. Performing RDE on catalysts supported on NSTF is a better measurement than using mirror-polished GC disks because the material being measured has the same morphology, composition and surface structure as the material that would be used in a PEM fuel cell.

Chapter 5

ORR Activity of $Pt_{1-x}M_x$ (M = Ni, Co) Dealloyed Catalysts

This chapter presents data collected from measurements performed on binary Pt-M (M = Ni, Co) solid solutions. The majority of the work in this chapter has been published ([121]).

5.1 RDE Measurement Protocol

In this study, the catalyst precursors were sputtered-deposited onto NSTF-coated GC disks to be measured by the RDE technique. The catalyst samples, RDE measurement procedures, as well as data analysis were chosen / modified in order to effectively characterize the dealloying process. The catalyst precursors $Pt_{1-x}M_x$ (M = Ni, Co) have high Ni or Co content ($x > 0.6$). When these precursors were placed in the electrochemically corrosive environment of the RDE cell, the material underwent dealloying. The dealloying process impacts the active surface area (SEF) and catalytic activities (j_{planar} and $j_{specific}$) as the experiment continued. The RDE electrodes used in this chapter were NSTF-coated GC disks that were explained in detail earlier in Chapter 4 and in [18], [60], [61], [64], [115].

5.1.1 Continuous Ar CV – ORR Measurements by RDE

Traditionally, RDE measurements start with an electrochemical cleaning procedure that involves multiple cycles of fast (e.g. 100 ~ 500 mV/s) CVs over the same potential range

of the measurements until a steady state voltammogram is obtained. The data measured during the electrochemical cleaning procedure, if any, represents the transient behavior of the catalyst and are usually discarded. Figure 5-1 shows a CV plot obtained during a typical electrochemical cleaning of a polycrystalline Pt RDE. It is apparent that the Pt catalytic surface underwent small changes during the cleaning process as the current peaks that represent Pt (110) and Pt (100) at 0.15 and 0.35 V_{RHE}, respectively [113], increased gradually during 100 CV cycles. The catalytically active surface area of the polycrystalline Pt electrode also increased during the cleaning, shown in Figure 5-2. The SEF of the electrode increased from ~ 1.6 cm^2/cm^2 at the beginning of the cleaning, to ~ 1.85 cm^2/cm^2 around the 50^{th} CV cycle and stabilized for rest of the CVs.

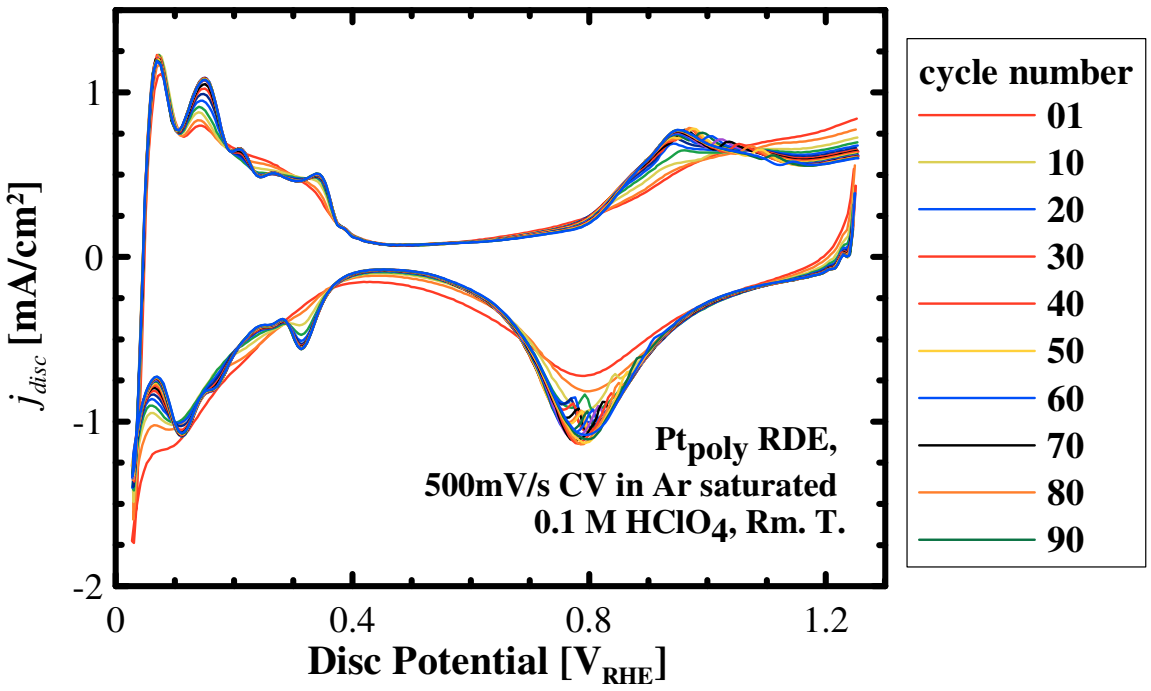

Figure 5-1 A typical "Electrochemical Cleaning" of polycrystalline Pt.

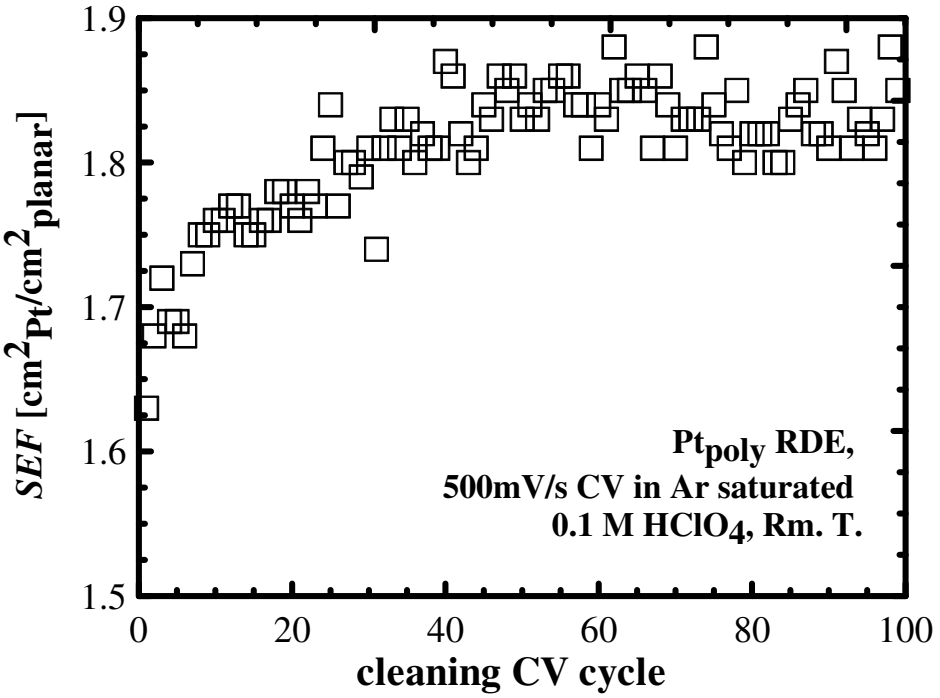

Figure 5-2 SEF varies over CV cycle number measured during the electrochemical cleaning of polycrystalline Pt.

The transient response is of interest to study the dealloying process of the sputtered catalysts to the Ar CV and ORR experiments prior to the steady state. Figure 5-3 shows the continuous CV-ORR RDE protocol used to examine the samples. During an experiment, the catalyst supported on the NSTF-coated GC disks was mounted into the RDE tip and washed with warm nano-pure water before being placed in the RDE solution cell. Once in the cell, the electrode was first held at 600 mV_{RHE} while Ar gas was continuously bubbling in the electrolyte for 10 minutes, as shown in Figure 5-3. After the Ar purge, three 50 mV/s CV cycles were measured, followed by 1-minute potential holds at 1000 mV_{RHE} and 900 mV_{RHE} each. For each potential hold, the electrode was first held at 600 mV_{RHE} for 10 seconds before stepping to the high potential for measurements. The purpose of a 600mV_{RHE} hold prior to the measurement is to electrochemically clean the

catalyst surface. After the potential hold measurements in Ar-saturated electrolyte, the electrode potential was held at 600 mV_{RHE} and the gas was changed to O_2 for a 10 minute purge, shown in Figure 5-3 by bold lines. After O_2 purging, the same CV and potential hold experiments were performed in the O_2-saturated cell, shown in Figure 5-3 as bold lines and cross-hatched areas. After the O_2 measurements, the gas was changed back to argon and the "Ar purge-CV-Hold → O_2 purge-CV-Hold" test block was repeated many times. The data from this continuous CV-ORR testing protocol were then used to track SEF, j_{planar}, and $j_{specific}$ as a function of time for the catalyst materials of interest.

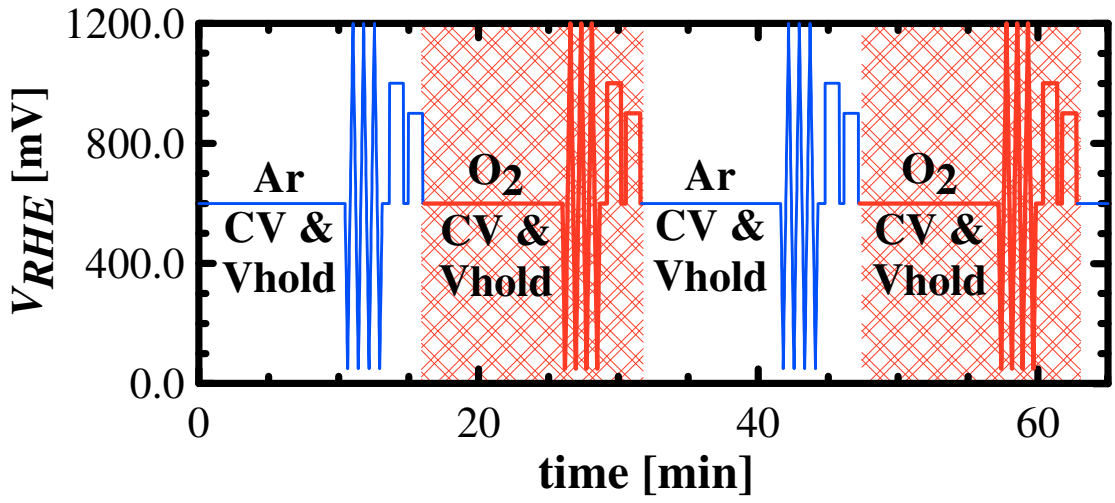

Figure 5-3 Continuous RDE protocol has repeating Ar CV and ORR measurements.

5.1.2 Large Active Surface Area and IR-Correction

When measuring CV and ORR data of thin film catalysts on NSTF-coated GC disks, it is important to take into account the resistance from the 0.1 M $HClO_4$ solution cell and its impact on the CV and ORR measurements [122-125]. The impact of solution cell resistance on the CV and ORR features was a lesser concern for samples measured on

mirror-polished surfaces because the catalytically active surface area and the measured current were smaller. Figure 5-4 illustrates the impact of high active surface area on the measurements. Figure 5-4a shows Ar CV, ORR and Faradaic current versus potential plots of catalyst on mirror-polished disks and Figure 5-4 b) shows the plots for NSTF-supported catalysts. In both Figures 5-4a and 5-4b, the Faradaic currents were calculated by simple subtraction: $j_{fara} = j_{ORR} - j_{CV}$.

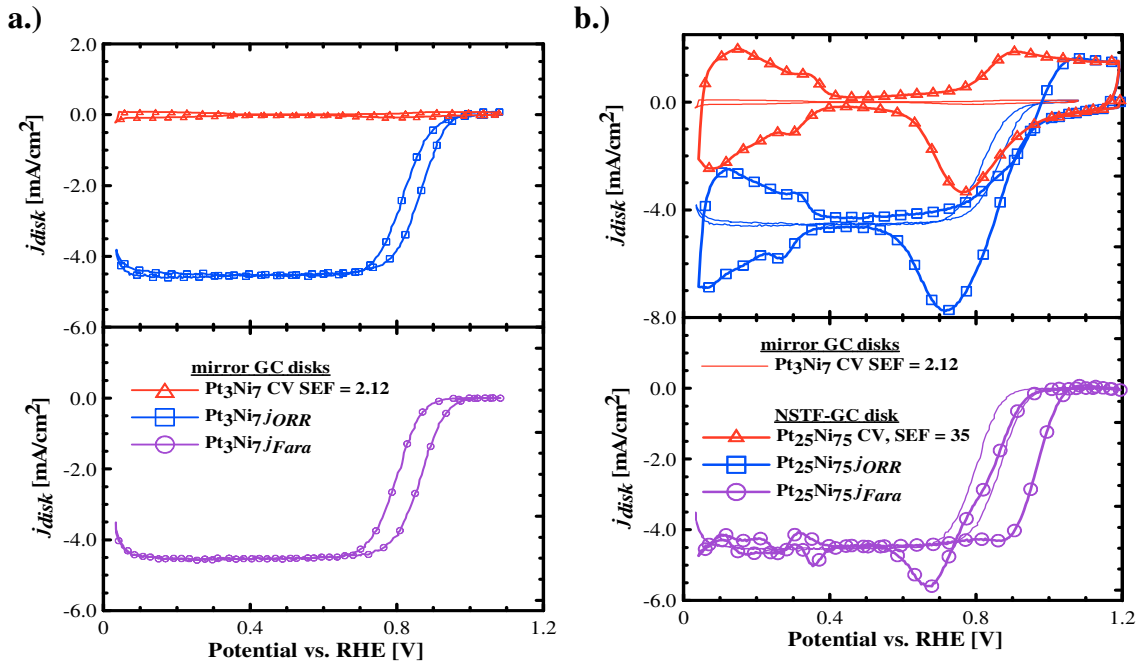

Figure 5-4 Ar CV and ORR plots of catalyst measured on mirror GC (a) and NSTF-coated GC disks (b).

Figure 5-4a shows a smooth ORR curve with the Faradaic diffusion limited current at a constant level that is consistent with the Levich equation [110], [111], [114]. The impact of the ohmic contribution to the measurements, for mirror-polished disks, was negligible and the faradaic current can be realized via simple subtraction. This is not the case for

NSTF-supported catalyst as shown in Figure 5-4 b). Instead of a flat, constant-current level, the diffusion-limited region of the faradaic curve has multiple peaks. This is due to the misalignment of the potentials of the ORR and CV curves caused primarily by solution resistance in the RDE cell. The high current from NSTF-supported samples, together with the cell resistance, causes the potential of voltammetric features to shift during measurement. The potential shift is current dependent and IR correction of the data is needed to ensure reliable determination of the faradaic ORR current density.

In this study, the IR correction to the data was done by a least square fitting software program that minimizes the fluctuation of faradaic current in the diffusion limited regions by adjusting the resistance, R:

$$V_{corrected} = V_{measured} - I_{measured} * R \qquad (4\text{-}1)$$

The typical value of optimized value for R in this study was ~ 50 Ohm. This is consistent with a recent report by van der Vliet et al. [122] on the measured resistance of 0.1 M $HClO_4$ being ~ 30 Ohms with a Pt/C slurry working electrode and a Pt black counter electrode. Figure 5-5 shows the result of the IR correction on the same set of data in Figure 5-4b. The figure shows data before the IR-correction in dashed lines and the results of IR-correction in solid lines. After the IR-correction, there are small changes in the CV and ORR curves while the faradaic curve shows a constant current level in the diffusion-limited region.

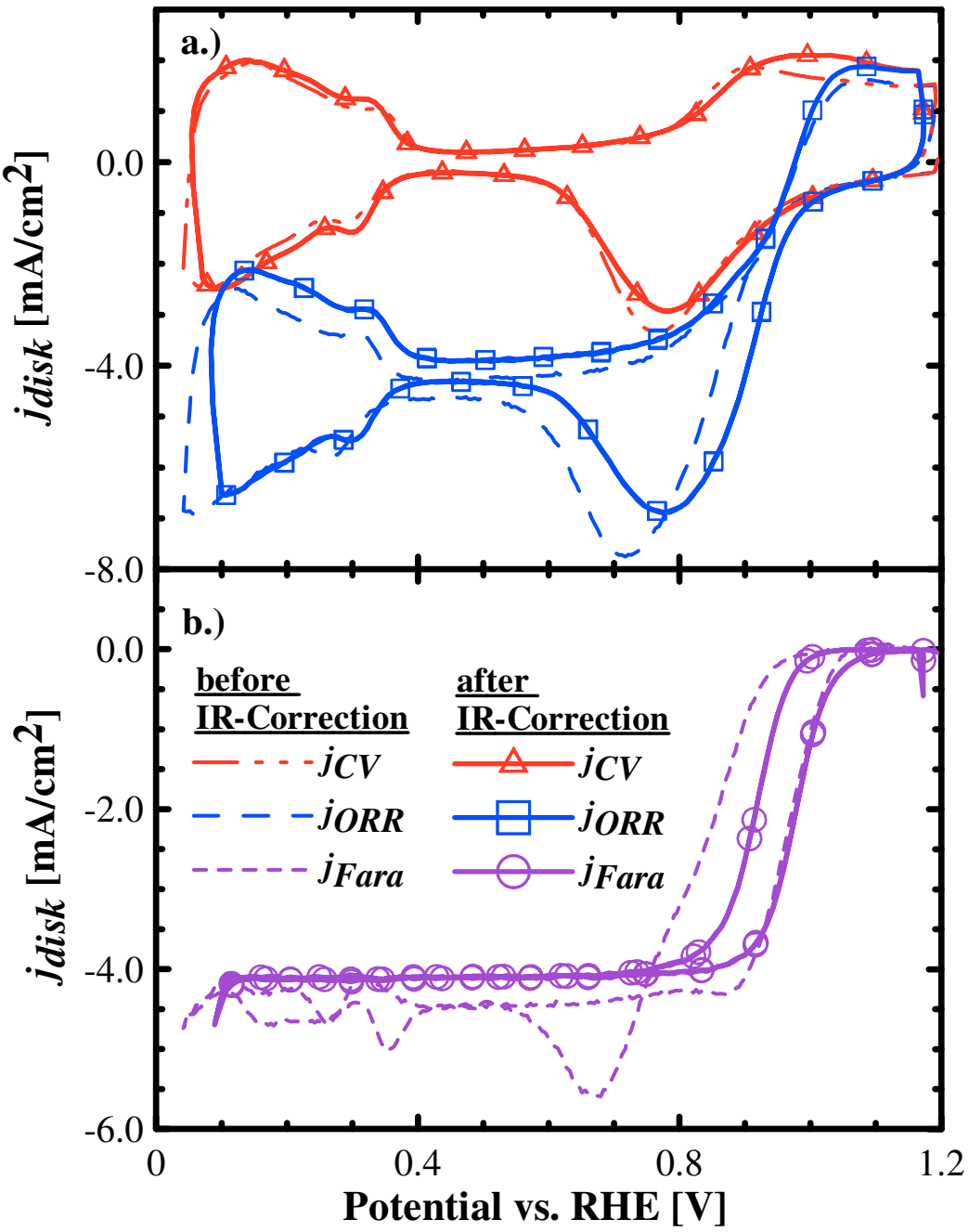

Figure 5-5 Measured Ar CV and ORR curves before (dashed lines) and after (solid lines) IR correction shown in a). Faradaic current before (dashed lines) and after (solid lines) IR correction shown in b).

5.2 Sputter Deposition of $Pt_{1-x}Ni_x$ and $Pt_{1-x}Co_x$ Catalyst Precursor Films

The catalysts were deposited on both mirror-polished and NSTF-coated GC disks with a Corona Vacuum Coaters V3T multi-target magnetron sputtering machine. Detailed information about this apparatus and its operation can be found in previous sections. During deposition, the chamber pressure was kept at 0.85 mTorr with an argon flow rate of 3 sccm and substrates were mounted on a rotating table. A "constant" mask was placed over the platinum target to deposit a constant amount (0.15 ~ 0.16 mg/cm^2) across the substrates mounted on the rotating substrate table. In order to deposit a high M (M = Ni, Co) content and to produce a linear gradient of $Pt_{1-x}M_x$ ($0.6 < x < 0.8$), two targets of the same M (M = Ni or Co) were used during sputtering. The first target was covered with a "constant" mask in order to deposit a constant loading across each substrate. The second was covered with a "linear out" mask to deposit a linear gradient of M across the sputtering track. During the sputtering run, all three targets (two M and Pt) were turned on at the same time and were set to deposit a linear gradient of M (M = Ni, Co) intermixed with 0.16 mg/cm^2 Pt, across the sputtered region.

Figure 5-6 shows the composition of the sputtered $Pt_{1-x}Ni_x$ catalyst film measured by different techniques. The mass of material deposited, shown in Figure 5-6a, was determined by weighing preweighed aluminum disks placed along the sputtering track after deposition. Figure 5-6a shows mass data for two sputtered films; the first set of data was from the $Pt_{1-x}Ni_x$ intermix as described above, the second set of data was from a constant Pt film sputtered under identical conditions, resulting in a constant mass profile

(0.15 mg/cm^2). The mass profile of $Pt_{1-x}Ni_x$ increased linearly (from 0.3 to 0.35 mg/cm^2) along the sputtered track due to increasing Ni content. The atomic fraction of Ni (x in $Pt_{1-x}Ni_x$) in the $Pt_{1-x}Ni_x$ composition spread calculated from each mass measurement is shown in Figure 5-6b with a dashed line. Figure 5-6b compares the Ni ratio calculated from the mass data with measurements made by a JEOL 8200 electron microprobe. Figure 5-6b also shows the location of RDE disks positioned along the sputtering region as labeled circles. The Ni content increased from x = 0.65 (RDE disk number 1) to x = 0.75 (RDE disk number 5) along the sputtering track.

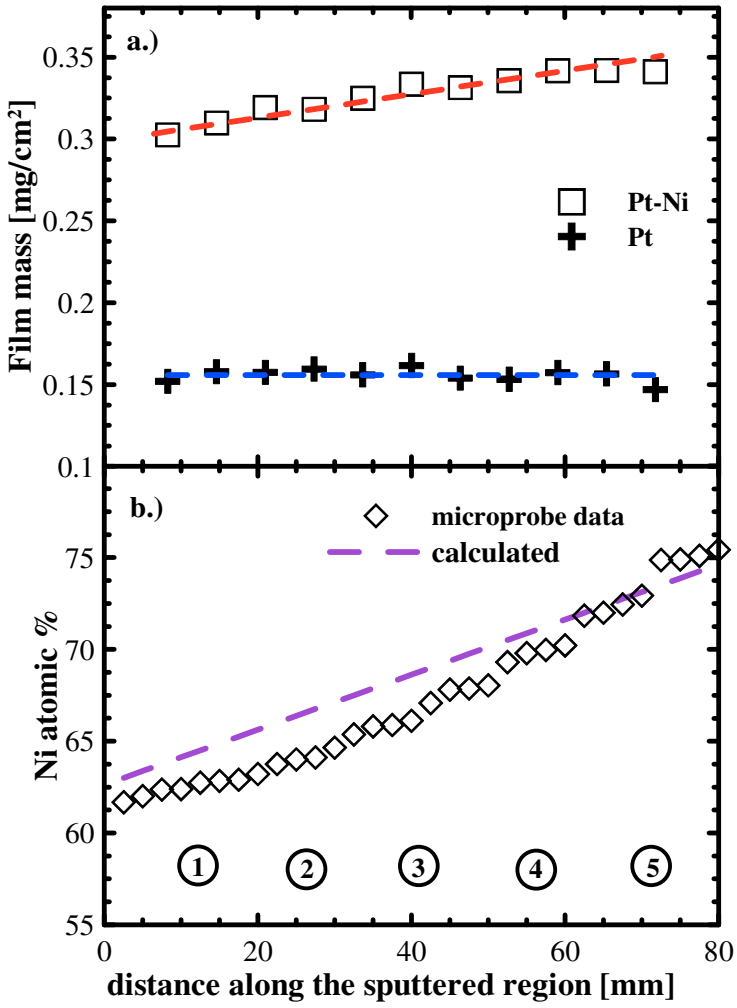

Figure 5-6 Composition of sputtered Pt-Ni catalyst measured by mass (a) and microprobe (b), the circles at the bottom shows the location of the RDE disks. ([121])

The $Pt_{1-x}Co_x$ ($0.6 < x < 0.8$) films were produced in the same manner as $Pt_{1-x}Ni_x$ films described in earlier section, with a constant Pt target, a constant Co target and a linear-out Co target. Figure 5-7 shows the weigh disk data together with the electron microprobe data collected for the composition-spread deposited. The composition spread appears to range from approximately 0.6 to 0.75 mol fraction of Co or $0.6 < x < 0.75$ in $Pt_{1-x}Co_x$. Prior calibration of the amount deposited when running with just the Pt target energized gave an average Pt deposition of 0.15 mg/cm^2. The difference in mass between the Pt calibration run and the mass measured on the composition spread reported here should be a measure of the mass of cobalt deposited. These data can then be used to determine an independent measure of cobalt atomic content. The electron microprobe and weigh disk data were combined through a series of equations developed to provide a best fit to the combined data set in terms of composition as a function of radial distance across the sputtering track. The dashed lines in Figure 5-7 show the results from this fit protocol. The agreement between the calculated and measured data for both test methods is good, giving confidence in the fit equation that will be used later to determine composition for a given position along the sputtering track.

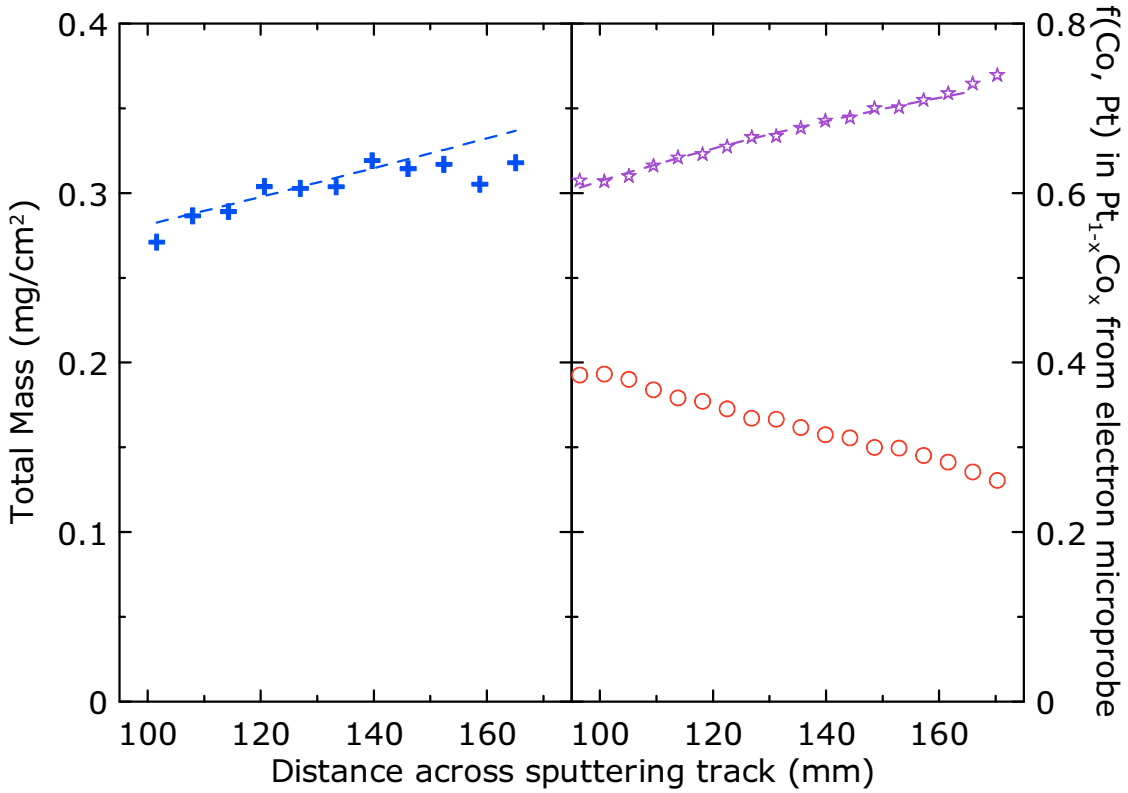

Figure 5-7 Left panel, weigh disk data; right panel, electron microprobe data for the $Pt_{1-x}Co_x$ composition spread. The dashed line on both panels represents the linear best fit obtained from the microprobe data (Ni: stars, Pt: circles) [121].

As described in section 3.1 of this thesis, during sputtering deposition of catalyst films the stationary Pt and M (M = Co or Ni) targets were turned on. Each target was covered with a mask to produce the desired deposition profiles (linear gradient or constant thickness). The substrates such as NSTF-coated GC disks and weighing disks were mounted on the rotating substrate table. During each sputtering deposition runs, the substrate table rotates at 15 ~ 18 rpm in order to produce a solid solution of different metals intermixed at an atomic level.

The sputtering of the $Pt_{1-x}Co_x$ and $Pt_{1-x}Ni_x$ catalyst film samples used in this thesis typically took 1 hour to complete. In the 1-hour-long sputtering deposition, the substrates on the rotating table would pass the stationary targets roughly ~ 1000 times and received roughly an atomic layer of Pt and M (M = Ni or Co) during each passing. Thus the resulting $Pt_{1-x}Co_x$ and $Pt_{1-x}Ni_x$ films were solid solutions of the elements and showed respective characteristic XRD structural signatures [69], [70], [126].

5.3 $Pt_{1-x}Ni_x$ Dealloying Process – RDE and *ex-situ* XRD Study

Figure 5-8 shows selected CV and ORR curves for $Pt_{35}Ni_{65}$ sputtered onto a NSTF-coated GC disk. The figure also includes data for Pt sputtered on mirror-polished and NSTF-coated GC disks for comparison. The Pt control samples were measured by the same CV/ORR protocol as explained in the previous section. The data shown in Figure 5-8 were corrected for RDE cell IR-drop as discussed earlier. Figure 5-8a shows that the CV curves for $Pt_{35}Ni_{65}$ had a larger hydrogen adsorption-desorption area than that of Pt on NSTF-coated GC disks (bold black line) at the beginning of the test protocol (test block #1, shown with crosses). As the experiment continued, the CV curves showed an apparent increase in the ECSA and voltammetric features appeared near 100 and 250 mV_{RHE}. Figure 5-8a also shows an apparent shift of the voltammetric onset associated with Pt-OH formation near 800 mV_{RHE} during the anodic sweep. As the experiment progressed, the onset for Pt-OH_{ads} formation shifted to a higher potential (see block 10 for example). This trend was apparent for all of the Pt-Ni samples measured by the continuous CV-ORR test protocol and will be discussed in more detail later.

Figure 5-8b shows selected ORR curves for $Pt_{35}Ni_{65}$ and Pt deposited on NSTF-coated GC disks. All ORR data were collected at 900 rpm with a sweep rate of 50 mV/s. All of the measurements shown reached the theoretical mass-transfer limited current (~ 4.5 mA/cm^2 for oxygen diffusion in 0.1 M $HClO_4$ electrolyte with 900 rpm RDE rotation rate at room temperature [114]). The onset potentials and half-wave potentials for catalysts from the same sputtering run deposited on flat surfaces were 50 to 100 mV lower than the onset and half-wave potentials of the catalysts sputtered onto NSTF-coated GC disks. The high onset and half-wave potentials measured for the NSTF-supported catalysts was in part caused by the high surface enhancement factor (SEF) of the NSTF. The Pt film sputtered on the mirror-polished disk had SEF of ~ 1.8 cm^2/cm^2 and reached the diffusion-limited current level at ~ 0.75 V_{RHE} while the NSTF-supported Pt had a SEF of ~14 cm^2/cm^2 and reached the diffusion-limited current level at ~0.85 V_{RHE}. Figure 5-8b also shows that $Pt_{35}Ni_{65}$ initially had a very high onset potential (in test block #1) and reached the diffusion-limited current level at ~ 1.0 V_{RHE}. The onset of the ORR curves shifted to a lower potential for the second test block and reached the diffusion-limited current level at ~ 0.95 V_{RHE}. The ORR half wave potential decreased slowly for the rest of the experiment (test block #3 to #10).

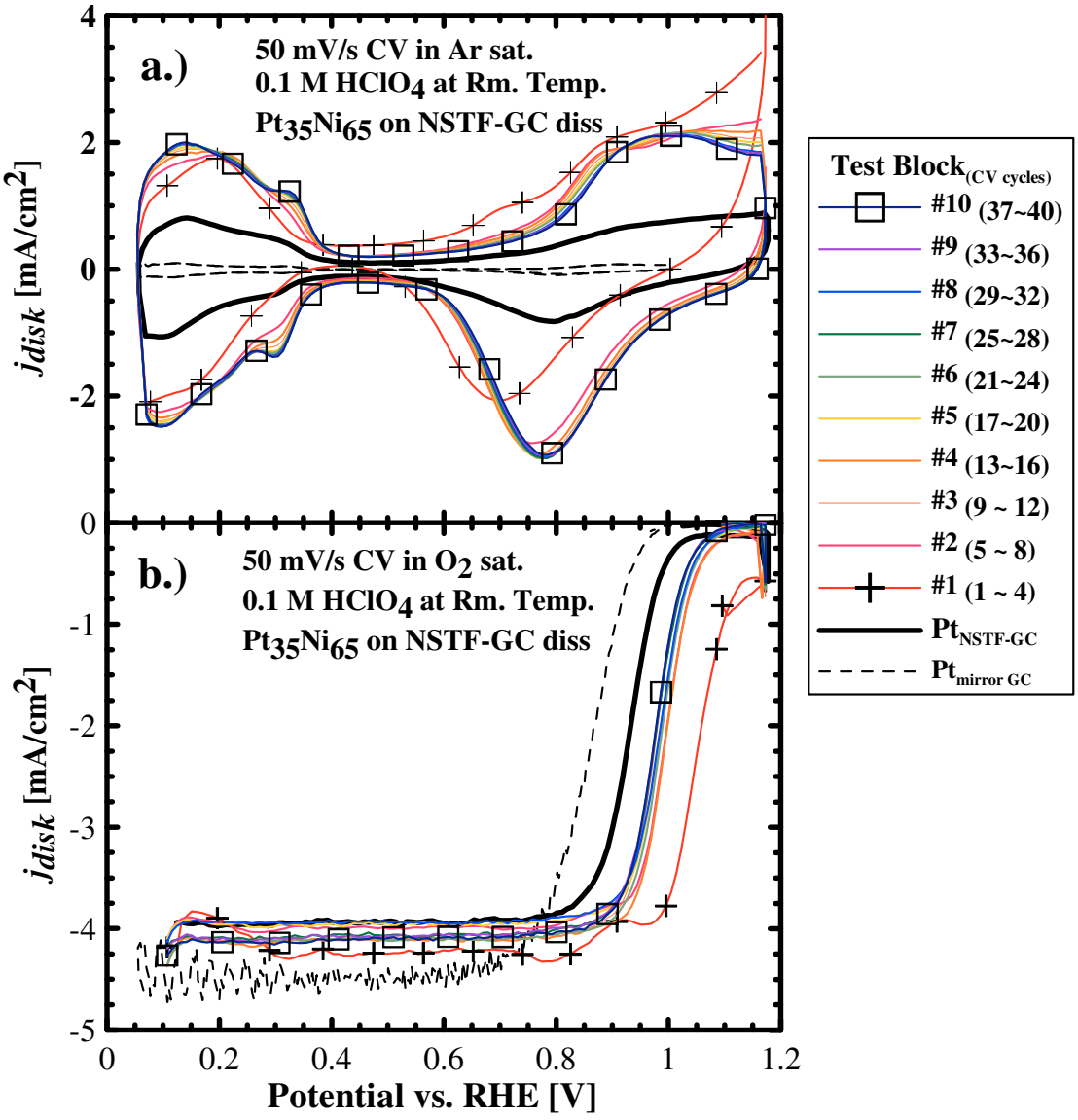

Figure 5-8 Ar CV (a) and ORR (b) measurements from the continuous RDE protocol

The kinetic current densities of the Pt and $Pt_{35}Ni_{65}$ material supported on NSTF-coated GC disks shown in Figure 5-8 were calculated and are plotted as Tafel-style graphs in Figure 5-9. ORR activities of different catalysts in such Tafel plots are typically compared at potentials between 850 and 950 mV for thin film catalysts measured on flat surfaces as they have onset potentials near 900 mV and reached diffusion-limited currents

near 800 mV. The NSTF-supported catalysts described here have a higher onset potential (near 1000 mV) and reached the diffusion-limited currents near 900 mV. In order to minimize the error introduced by the diffusion correction, the catalytic activities of these catalysts need to be compared at higher potentials; between 950 and 1000 mV.

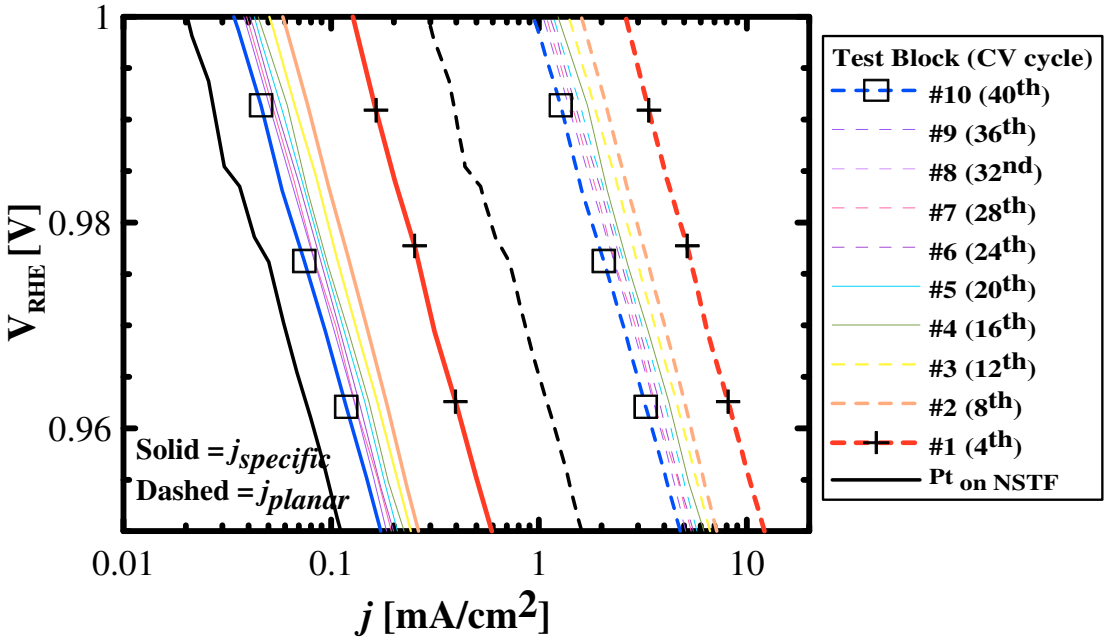

Figure 5-9 Tafel plots of Pt_3Ni_7 catalyst compared with Pt on NSTF-coated GC disks. The dashed lines show planar current density data; the solid lines show the ORR performance per measured Pt area ([121])

Figure 5-9 shows the Tafel-style plots in the kinetic region and presents the data in two formats: planar current density j_{planar} (Eqn. 3-7, plotted with dashed lines) and specific current density $j_{specific}$ (Eqn. 3-8, plotted with solid lines). It is apparent that, on NSTF-coated disks, the $Pt_{35}Ni_{65}$ material has much higher planar current density than sputtered Pt. As shown in Figure 5-9, j_{planar} of $Pt_{35}Ni_{65}$ material reached > 2 mA/cm^2 at 1000 mV at the beginning (test block #1) before shifting to a lower current density level of ~ 1.5

mA/cm^2 at 1000 mV (test block #2) and gradually declined to ~ 1 mA/cm^2 at 1000 mV as the experiment progressed towards test block #10. The same Pt loading (with no Ni) deposited on NSTF-coated disks, on the other hand, shows j_{planar} of only ~ 0.2 mA/cm^2. After normalizing the data by the active Pt surface area (Eqn. 3-8), it was found that $Pt_{35}Ni_{65}$ (at 0.15 mg Pt/cm^2) has higher $j_{specific}$ than sputtered Pt. As shown in Figure 5-9, $j_{specific}$ of $Pt_{35}Ni_{65}$ reached > 0.1 mA/cm$^2_{Pt}$ at 1.0 V at the beginning (test block #1), dropped to ~ 0.06 mA/cm$^2_{Pt}$ at 1.0 V (test block #2) and then continued to decrease, reaching ~0.035 mA/cm$^2_{Pt}$ for test block #10. The pure Pt disk exhibited $j_{specific}$ of ~ 0.02 mA/cm$^2_{Pt}$. Figure 5-9 also shows that the $Pt_{35}Ni_{65}$ catalyst material had the same Tafel slopes (~ 60 mV/decade) as sputtered Pt.

The SEF of different $Pt_{1-x}Ni_x$ compositions as a function of potential cycles is shown in Figure 5-10. The data shown in Figure 5-10 are grouped into test blocks, with three measurements of SEF per test block. Figure 5-10 also includes SEF data for Pt sputtered on a NSTF-coated GC disk for comparison. The continuous CV-ORR test protocol was performed on the sputtered Pt and $Pt_{1-x}Ni_x$ materials for 14 test blocks over 9 hours. Conceptually, the CV-ORR test block could be repeated continuously for a very long period of time. However, as the experiment continues for more than couple of hours, atmospheric contamination of the liquid electrolyte of the RDE cell has a measurable impact on the catalyst performance. Therefore the continuous CV-ORR test protocol was used to examine the transient response of the catalyst only: from the initial point where the electrode was assembled, until the performance indicators reached a meaningful steady-state trend at the end of 14th test block.

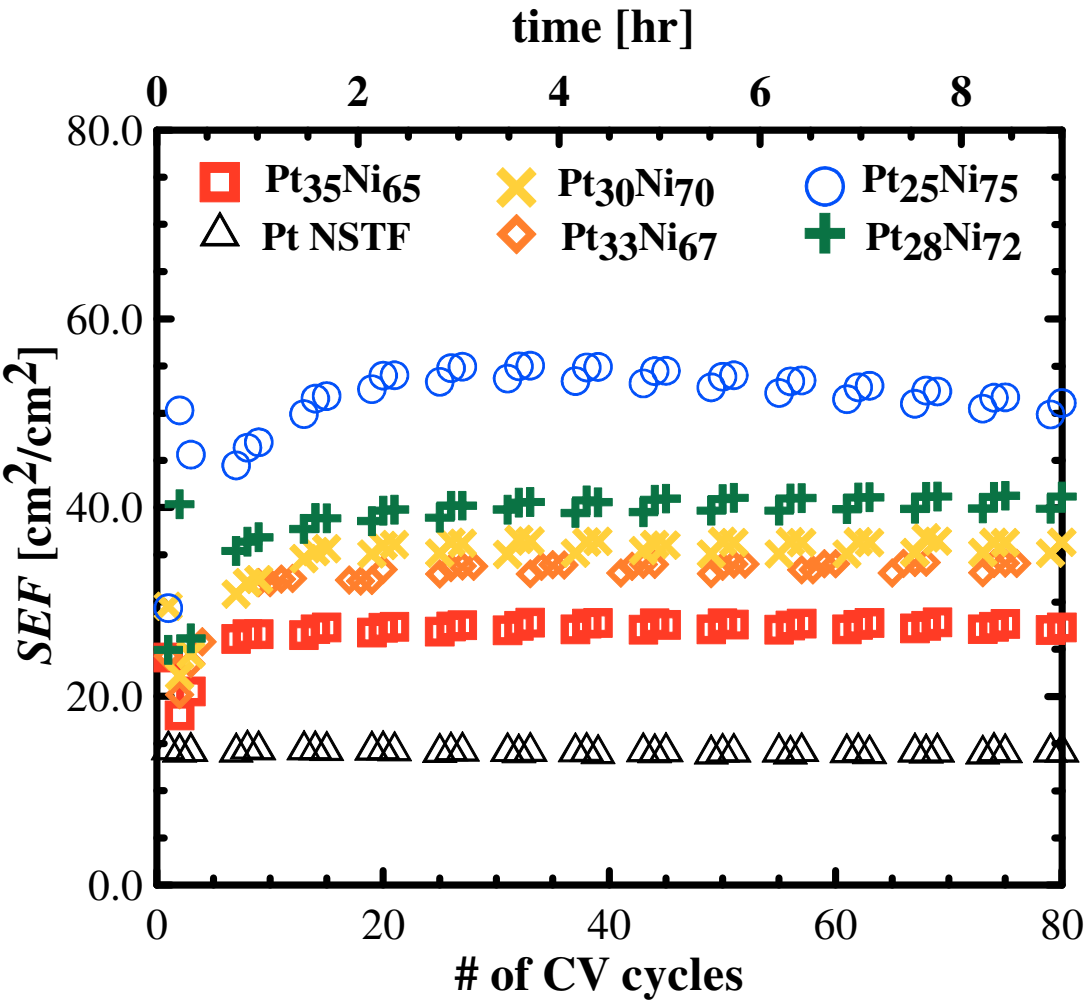

Figure 5-10 SEF values of all Pt-Ni catalysts plotted as a function of CV cycle numbers. Data from sputtered Pt are also included for comparison ([121]).

Figure 5-10 shows a summary of SEF as a function of CV cycles for all $Pt_{1-x}Ni_x$ materials compared to sputtered Pt. The sputtered Pt had a SEF of ~ 14 cm^2/cm^2 and the SEF values showed a very subtle declining trend. The subtle decline in Pt SEF likely results from electrolyte contamination during the experiment. The Pt-Ni electrodes show a different trend: in general, all of the $Pt_{1-x}Ni_x$ electrodes had an initial SEF of ~ 20 cm^2/cm^2 (test block #1) which increased rapidly for the first few test blocks before

reaching stable values. As the nickel content increased (x in $Pt_{1-x}Ni_x$ increased from 0.65 to 0.75), the maximum SEF value increased. $Pt_{35}Ni_{65}$ gave a maximum SEF of ~ 28 cm^2/cm^2 and the SEF for $Pt_{28}Ni_{72}$ reached a maximum value of ~ 40 cm^2/cm^2. The SEF of $Pt_{25}Ni_{75}$ material had the same trend and had an initial value of ~ 20 cm^2/cm^2, reaching a maximum of ~ 55 cm^2/cm^2 near test block #5 ~ 6. These rapid increases in surface area with increasing x are consistent with observations by other groups on Pt-M dealloy catalysts, where M is a non-noble metal [89], [92], [127]. The peak value is dependent on the analytical method used to measure the at% Ni fraction, whether the measurement uses an MEA versus RDE sample, and to some extent the history of each sample.

These large increases in SEF relative to pure Pt are believed to be the result of Ni dealloying from the sputtered $Pt_{1-x}Ni_x$ catalysts during the CV cycling. During the RDE experiments, the acidic electrolyte, together with the applied potential, created favorable conditions for the less-noble metal, Ni, in the $Pt_{1-x}Ni_x$ catalysts to dissolve. Dissolution of Ni from the catalyst surface and near-surface would likely lead to the formation of a porous, Pt-rich structure that has high surface area. It is not clear from these data whether bulk de-alloying occurred or whether the enriched Pt surface layers formed through surface de-alloying hindered Ni dissolution from the bulk. In order to investigate this further, an ex-situ XRD study was conducted. The XRD profile of one high Ni content disk was measured at various times throughout the CV-ORR protocol by removing the electrode from the electrolyte and transferring it to the diffractometer. After XRD data was collected, the electrode was returned to the solution cell for further testing. The result is shown in Figure 5-11.

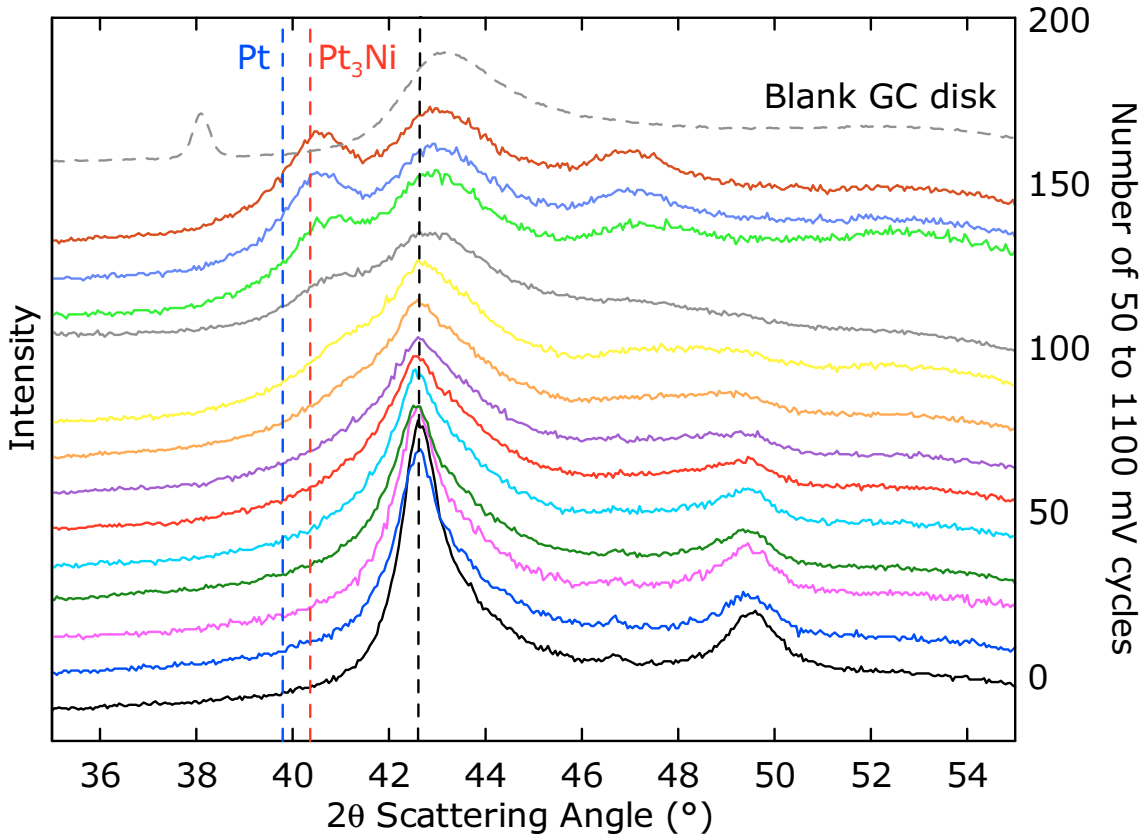

Figure 5-11 XRD data for $Pt_{0.28}Ni_{0.72}$ on a NSTF-coated GC disk as a function of number of potential cycles. The scans have been offset vertically for clarity. The data measured on a blank disk is shown as the top scan in the figure. The number of potential cycles increases from the bottom to the top of the figure. The scattering angles expected for FCC Pt, Pt_3Ni and the original sputtered material are shown as vertical dashed lines.

Figure 5-11 shows the XRD data measured for a disk with $Pt_{0.28}Ni_{0.72}$ deposited on NSTF. The top dashed scan shows the pattern of the blank or bare (no catalyst coating) NSTF-coated disk; this background is present in all scans measured. This blank will contribute a background to the observed data. The scans for the $Pt_{0.28}Ni_{0.72}$ disk have been offset vertically for clarity. The total number of potential cycles completed during the CV-ORR protocol increases from the bottom to the top of the graph – the vertical offset for each scan has been set such that high angle intensity is located vertically according to the

number of cycles completed. Three vertical dashed lines have been included on this figure; 39.8° showing where the (111) peak of FCC Pt would appear, ~ 40.4° which corresponds to the (111) peak position expected for FCC $Pt_{0.75}Ni_{0.25}$ and 42.5°, the approximate location of the initial (111) peak of the as-sputtered catalyst. At the start of the experiment, there are well resolved (111) and (200) peaks for a FCC lattice with a lattice constant of ~ 3.7 Å (significantly smaller than that expected for Pt – 3.92 Å, but larger than that expected for Ni – 3.52 Å). This is consistent with the deposited composition being a single phase. It could be characterized as either a contracted Ni-substituted FCC Pt lattice or as an expanded Pt-substituted FCC Ni lattice.

As the catalyst was electrochemically cycled, the intensity of the (111) and (200) peaks in this scattering angle range decreased, suggesting loss of Ni. Even after 60 cycles, there is still some evidence that some of this phase remained. However there is also evidence for the emergence of a lower Ni content phase, with a lattice constant somewhat close to the $Pt_{0.75}Ni_{0.25}$ composition, although it is at a higher angle and thus likely contains more than 25% Ni. There is no evidence for any significant amounts of a pure Pt phase, thus the bulk of the catalyst still contains some Ni. With more CV-ORR cycles, most of the high Ni content phase has been lost, and the peaks from the lower Ni content phase are much stronger. This suggests that the bulk of the catalyst has lost much, but not all of the Ni. The time/potential cycle dependence of the emergence of the lower Ni content phase suggests that bulk de-alloying occurs only slowly during each potential cycle. This is therefore consistent with the idea that loss of surface Ni creates a Pt-rich surface layer that hinders subsequent diffusion of bulk Ni to the surface for dissolution.

Figure 5-12 shows j_{planar} and $j_{specific}$ at 1.0 V $_{RHE}$ of sputtered Pt and $Pt_{1-x}Ni_x$ catalysts on NSTF plotted as a function of potential cycle number. The vertical scales of the figures were selected to best show the trends in the data of the entire experiment, therefore some of the data points from test block #1 are much higher than the scale and are not included in the figure. j_{planar} of Pt sputtered on NSTF was ~ 0.3 mA/cm^2 at the beginning of the experiment and had a slight decline over the 14 test blocks (~ 9 hours).

Figure 5-12 shows all of the $Pt_{1-x}Ni_x$ catalysts had higher j_{planar} than that of sputtered Pt. However, the current density for the first test block was high compared to the rest of the data collected. $Pt_{35}Ni_{65}$ showed an initial j_{planar} of > 5 mA/cm^2 in test block #1; this decreased to ~1.5 mA/cm^2 in the second test block. After test block #2, the current densities continued to decrease at a much lower rate, reaching ~ 0.8 mA/cm^2 at the end of the experiment (test block #14). Some of the $Pt_{1-x}Ni_x$ catalysts showed j_{planar} of > 10 mA/cm^2 (off-scale) in the first test block. The high ORR current density in the first test block is also shown in the RDE measurements in Figure 5-8. When comparing trends in planar current density, j_{planar}, for different catalysts, it is apparent that an increase in Ni content (x in $Pt_{1-x}Ni_x$) results in a higher j_{planar} level, with $Pt_{25}Ni_{75}$ having the highest current densities.

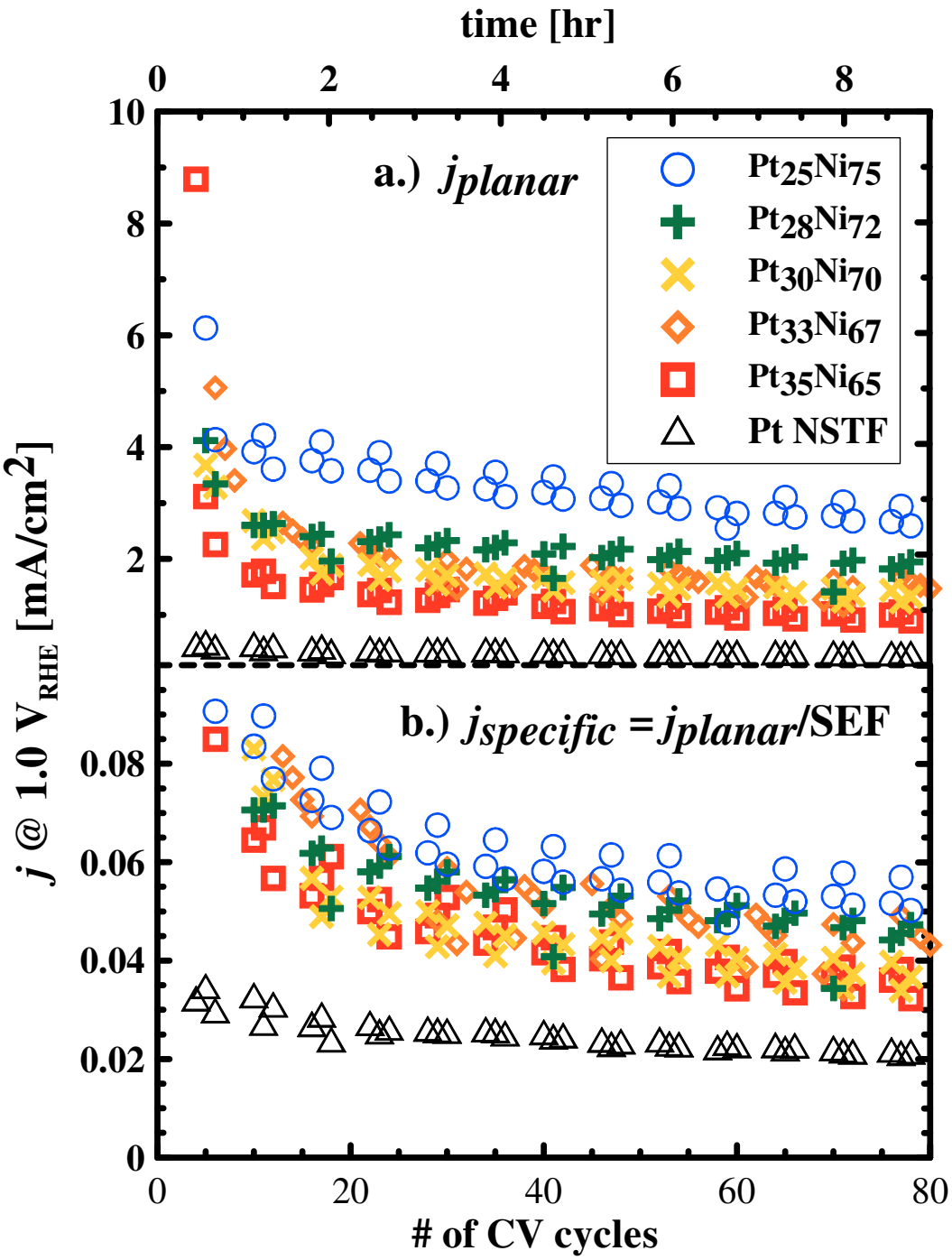

Figure 5-12 j_{planar} *and* $j_{specific}$ *of all Pt-Ni catalyst plotted as a function of CV cycle numbers. Data from the sputtered Pt are also included for comparison.*

Figure 5-12b shows the area specific current densities, $j_{specific}$, of all the $Pt_{1-x}Ni_x$ catalysts as a function of number of the potential cycles. The trends observed in $j_{specific}$ are similar

to those seen for j_{planar}, with an initial large current density drop between the first and the second test block, and then slow loss in specific activity to the end of the experiment. Figure 5-12b also shows that the catalyst with highest Ni content, $Pt_{25}Ni_{75}$, has the highest $j_{specific}$, i.e. highest catalytic activity per Pt site.

Figure 5-12b shows the $j_{specific}$ decaying trends for various Pt-Ni catalysts appear to be similar. In order to further examine the composition dependence of activity decay, the fractional specific activity of all catalysts shown in Figure 5-12b were plotted as a function of CV cycle number in Figure 5-13. In Figure 5-13, $j_{specific}$ measured at the beginning of test block #2 was used as the maximum (100%). Figure 5-13 shows the Pt fractional $j_{specific}$ (triangles) decayed to ~ 70% over the course of the experiment. When the frational $j_{specific}$ of various $Pt_{1-x}Ni_x$ catalysts are compared with that of Pt, it is apparent that the fractional $j_{specific}$ of various $Pt_{1-x}Ni_x$ catalysts decay at about the same rate as that of Pt. Since RDE measurements of all disks were performed under the same conditions (900 rpm in 0.1 M $HClO_4$ electrolyte at room temperature), a similar fractional $j_{specific}$ decay rate among all catalysts suggests the catalysts encountered the same poisoning factors during the continuous RDE measurement protocol.

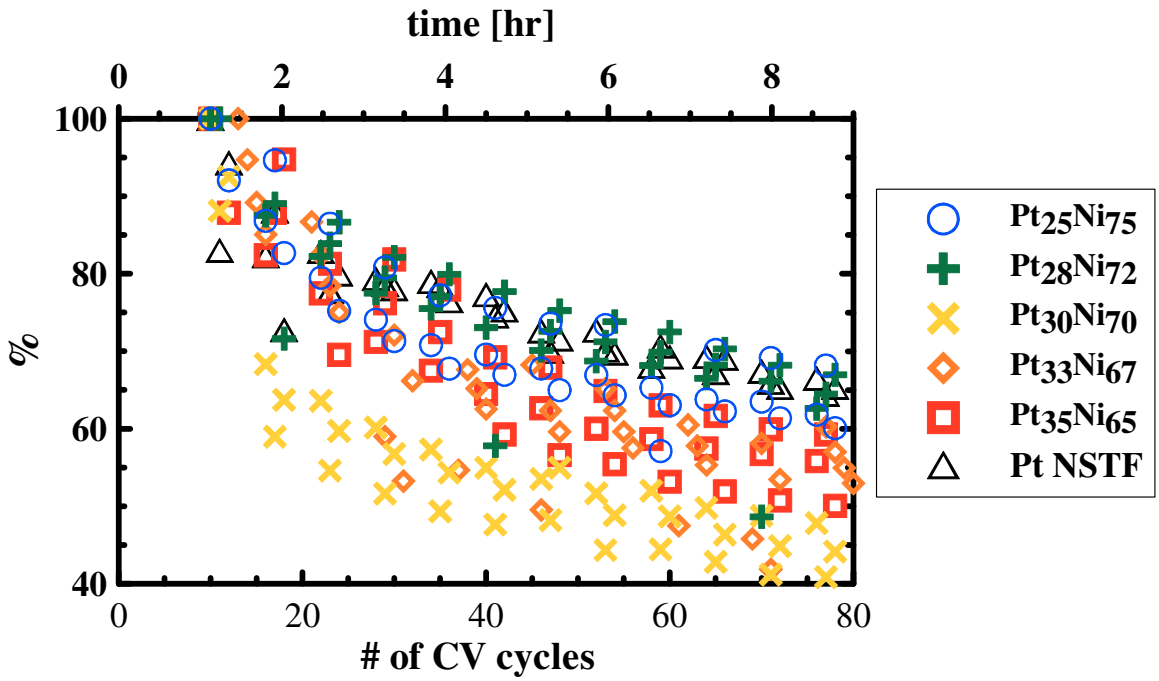

Figure 5-13 Fractional $j_{specific}$ of all Pt-Ni catalyst plotted as a function of CV cycle numbers. Data from sputtered Pt are also included for comparison. The $j_{specific}$ at the starting of test block #2 was used as 100%.

The loss in activity for both j_{planar} and $j_{specific}$ shown in Figure 5-12 and 5-13 is likely the combined result of Ni de-alloying, surface structure rearrangement and some contribution from electrolyte contamination. During the RDE measurements, Ar or O_2 were continuously bubbled through the electrolyte solution and vented into the ambient environment. Although the experiment apparatus and glassware were cleaned to the highest standards, and Ar or O_2 were continuously bubbled through the electrolyte, creating a small positive pressure in the solution cell, the cell was still open to the atmosphere. It is possible that trace atmospheric contaminants could enter the cells and dissolve into the electrolyte, potentially poisoning the catalyst surfaces to some extent. It is also possible that the electrolyte, 0.1 M $HClO_4$, decomposed and produced Cl^- ions which slowly poisoned the active Pt surfaces over the course of the experiment [109].

Figure 5-14 shows a summary of ORR performance indicators of Pt-Ni catalysts plotted as a function of Ni content. The Pt-area specific current density, $j_{specific}$, of all the $Pt_{1-x}Ni_x$ catalysts compositions tested were higher than that of sputtered Pt. As discussed earlier, the initial $j_{specific}$ of $Pt_{1-x}Ni_x$ catalysts measured in the first test block were nearly an order of magnitude higher than that of Pt in some cases. As the experiment progressed, the combined impact of the further de-alloying, and contamination of the electrolyte lowered the ORR activity. The final $j_{specific}$ from test block #4, shown in triangles in Figure 5-14, indicates that the ORR activities of $Pt_{1-x}Ni_x$ were still higher than that of sputtered Pt even after significant dealloying and some electrolyte contamination had occurred. Figure 5-14 also shows that $Pt_{25}Ni_{75}$ has the highest $j_{specific}$ after 14 test blocks. The SEFs of the $Pt_{1-x}Ni_x$ catalysts show the same trend, with $Pt_{25}Ni_{75}$ showing a SEF of ~25 cm^2/cm^2 at the beginning of the experiment, reaching a maximum of ~55 cm^2/cm^2 before declining to 50 cm^2/cm^2 at the end of the testing period.

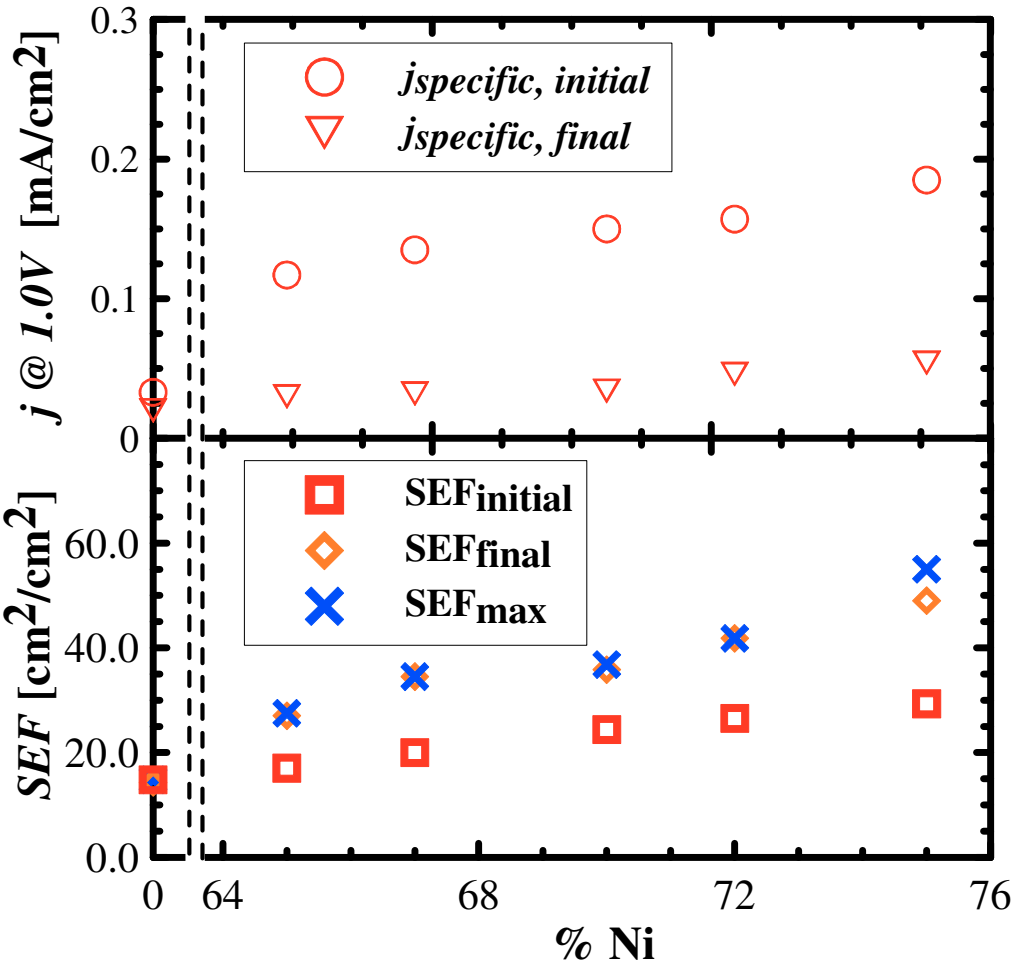

Figure 5-14 Summary of ORR performance indicators of Pt-Ni catalysts plotted as a function of Ni content

Recent investigations on Pt-Cu dealloyed catalysts by Strasser et. al. suggested that the area-specific activity gains seen for such catalysts result from both an increase in ECSA and, to a larger extent, the presence of compressive strain in the catalyst surface layers [92]. The compressive strain is thought to arise from the different lattice parameters between the Pt-rich shell and the Pt-Cu alloy core of the de-alloyed material. It is possible that core-shell like catalysts were formed from the $Pt_{1-x}Ni_x$ catalysts deposited on NSTF that have been described in this paper. At the beginning of the experiments

reported here, only a small amount of surface and near-surface Ni has been lost (as shown from the XRD data), resulting in a thin layer of Pt-rich shell (maybe exhibiting high strain). This material had the highest ORR activity. As de-alloying continued, more Ni dissolved, resulting in a thicker shell and hence possibly in less lattice strain at the surface. This resulted in a decrease in ORR activity.

5.4 $Pt_{1-x}Co_x$ Dealloying Process – RDE and *ex-situ* XRD Study

The $Pt_{1-x}Co_x$ catalyst films that were deposited onto NSTF-coated GC disks were measured by RDE protocol in the same manner as $Pt_{1-x}Ni_x$ disks. Figure 5-15 shows the evolution of the $Pt_{1-x}Co_x$ catalyst surface area enhancement factor (SEF) compared with Pt in the same style as $Pt_{1-x}Ni_x$ SEF trends shown in Figure 5-10. It is apparent that the $Pt_{1-x}Co_x$ samples have active surface areas that are 2 ~ 3 times higher than Pt. The SEF shows a systematic, dependence on Co content, reaching a maximum around 67 % Co content. The apparent higher surface areas of the alloys strongly suggest that much of the Co was lost during the RDE test protocol. In addition, the disks reached this high surface area after only a couple of CV cycles, suggesting this Co loss happened very quickly. All disks saw some loss in measured surface area with repeated cycling. Some of this loss likely comes from contamination of the electrolyte with atmospheric impurities as pure-Pt samples also see some loss of surface area over many hours of testing. However, the difference in SEF between disks with different Co contents (as-sputtered) decreases with multiple CV cycles as the higher (initial) surface area disks saw more surface area loss over time. This suggests that the surface structure initially formed from Co dissolution at

the peak dissolution level was somewhat less stable than the structures generated with lower Co loss.

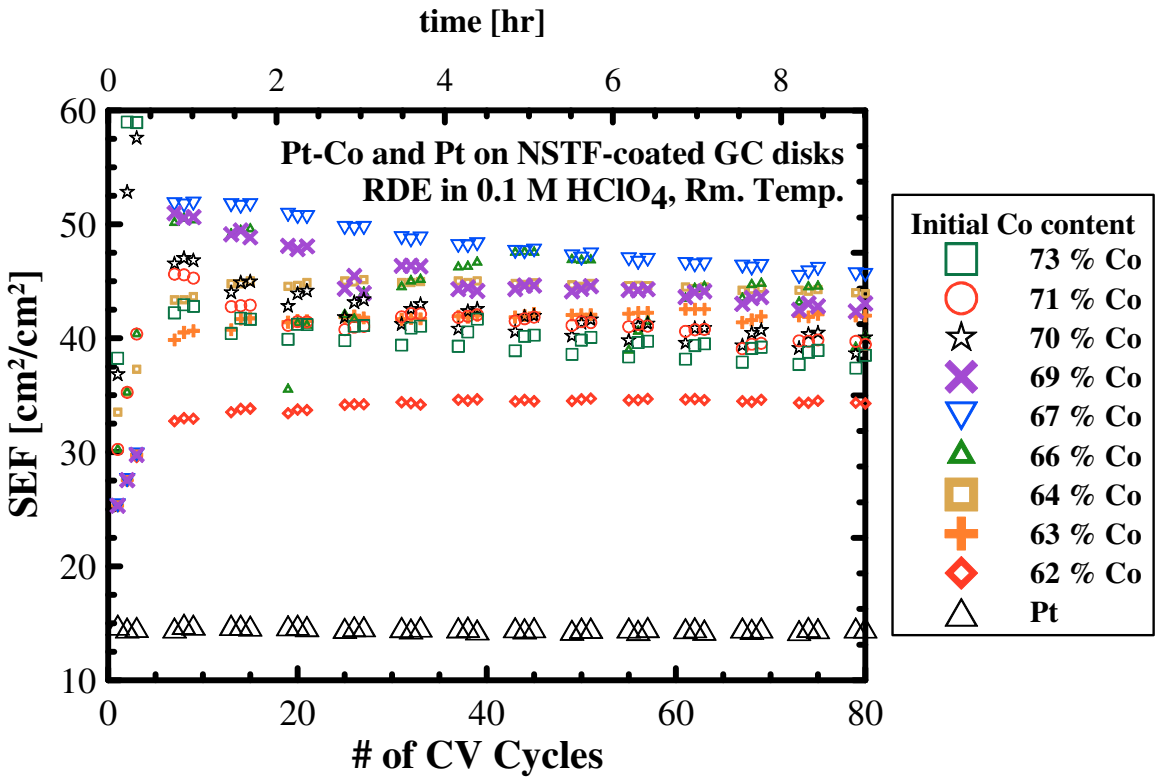

Figure 5-15 Surface enhancement factor (SEF) from RDE measurements on disks with different Co content over multiple potential sweeps ([128]).

Even with the problem of Pt-oxidation effectively covering a large fraction of the catalyst surface, it is interesting to examine the ORR current density at fixed potential as a function of Co content. Figure 5-16 shows the current density measured from ORR experiments, the data are presented in the same manner as that of Figure 5-12. Figure 5-16 shows the current density reaches a maximum for the disks containing around 66 $\pm$ 3 % Co. This is very close to the peak observed at 62 % in 3M fuel cell measurements of 50 cm^2 MEA's made with similarly deposited $Pt_{1-x}Co_x$ coated onto the NSTF whiskers in the Dalhousie apparatus [121], [128]. The measured current density decreases with

repeated CV-ORR cycling. This again may in part be indicative of surface structural rearrangement during testing. However, much of it is likely a result of contamination of the electrolyte with atmospheric impurities, as discussed earlier, during the ~ 7 hour measurement protocol.

Overall these results strongly suggest that the increased ORR activity of high Co content $Pt_{1-x}Co_x$ electrodes is predominantly the result of loss of Co from the catalyst, which leaves behind a porous, high-surface area, Pt-like matrix. There may also be a small enhancement of ORR specific activity caused by Co in the sub-surface atomic layers influencing the electronic properties of the surface. The data presented here does not, however, allow us to confirm whether or not this occurred especially as the ORR activities reported are for Pt surfaces with a variable fraction of the surface sites covered with OH-like species. The loss in surface area and ORR activity with repeated CV-ORR cycles may result from a combination of effects – some poisoning of the electrode surface by atmospheric impurities together with some collapse of the porous Pt network created by Co dissolution, possibly through an Ostwald ripening process.

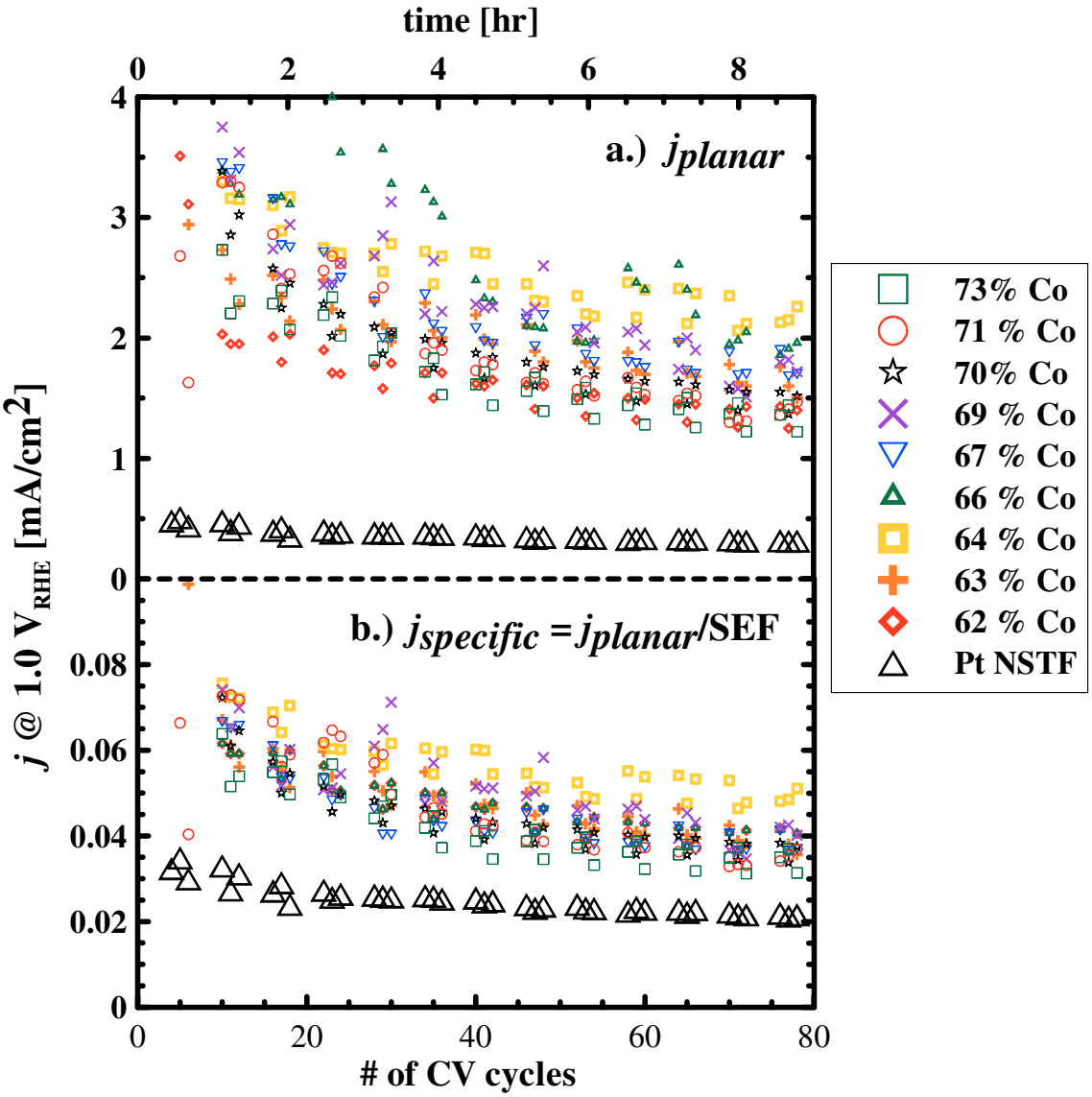

Figure 5-16 planar and specific ORR current of $Pt_{1-x}Co_x$ catalyst material as a function of CV cycles compared to Pt.

The RDE results indicate that much of the Co likely dissolved away during testing. This should result in significant changes to the bulk morphology of the catalyst deposits. In order to investigate these changes in bulk catalyst morphology, XRD data were collected on the disk containing 66 % Co (as-sputtered) throughout the CV-ORR cycling routine. The data in Figures 5-15 and 5-16 for this disk show step changes in performance. These

step changes occurred when the disk was removed from solution for measurement of XRD data. When the disk was placed back into the electrolyte, the observed surface area was lower than when the disk was removed from solution while the ORR activity increased, implying the specific activity increased. The SEF values increased and the ORR performance then decreased with more CV-ORR cycles.

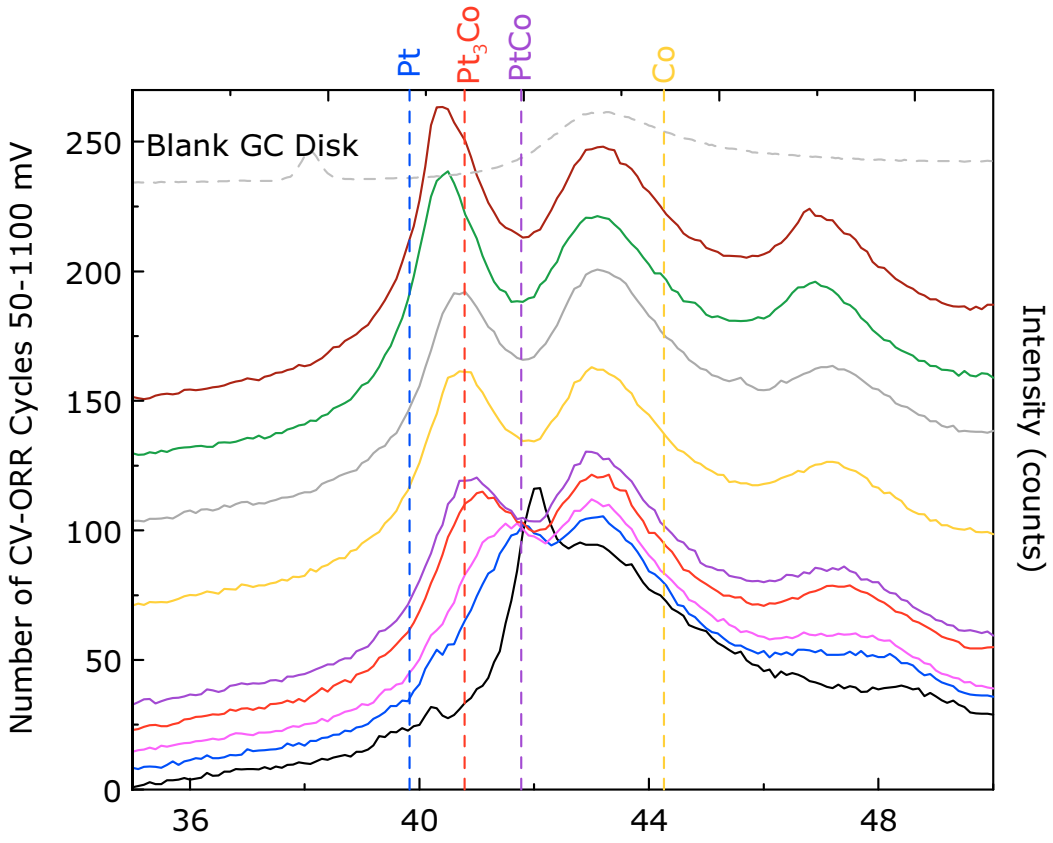

Figure 5-17 XRD data measured ex-situ on a NSTF-coated GC disk coated with $Pt_{0.34}Co_{0.66}$ throughout the argon/oxygen CV protocol. The scans have been offset vertically by the number of potential cycles completed to assist with visual clarity. The (111) peak positions expected for Pt, Pt_3Co, PtCo and Co are indicated with dashed lines on the figure.

Figure 5-17 shows the XRD patterns measured on the $Pt_{0.34}Co_{0.66}$ disk. The scans have been offset vertically to aid with data visualization and interpretation. The approximate

number of CV-ORR cycles completed for each scan is indicated on the left hand axis, with the cycle number determined by the point where the data intersects this axis. The (111) peak positions expected for Pt, Co and 2 known stable phases; PtCo and Pt_3Co are indicted by dashed lines on the Figure. The underlying GC disks provide a strong background contribution to the measured data – a scan collected on a blank disk is presented at the top of the Figure. The most important feature in this scan is the broad hump centered around 43.5°; this feature is present in all of the scans collected and essentially should be ignored or used as a reference point.

The first scan (scan number increases from the bottom to the top of the graph) exhibits a relatively sharp peak centered at 43° and shows that the catalyst layer deposits as an FCC lattice where Co has substituted for much of the Pt, giving a contracted lattice constant relative to Pt. The peak occurs at a higher angle than that expected for PtCo, consistent with a solid solution of Pt and Co containing more than 50 % Co (the disk contained 66 % Co by EMP). The second scan, after only 6 CV-ORR cycles has the main peak shifted to a lower scattering angle, close to that expected for PtCo. This implies some loss of bulk Co has occurred. With increase number of CV-ORR repeating test blocks, this peak continued to shift to lower angles, reaching the peak position expected for bulk Pt_3Co (~ 40.9°) after just 36 cycles. This implies that at least half of the Co initially present has dissolved away. The peak position keeps shifting to lower scattering angles with additional cycles, resulting in a final structure with bulk morphology somewhere between Pt and Pt_3Co. It is therefore clear that much of the Co initially present in the sample is lost during RDE testing and presumably would also be lost during fuel cell operation.

When comparing these XRD data with the RDE performance data, it appears that the extent of Co loss does not correlate directly with ORR activity and/or catalyst electrochemical surface area. It is clear that very large electrochemical surface areas (relative to Pt) are generated with only a relatively small loss of total Co. This will occur when a lot of Co dissolves from the catalyst surface, while the bulk Co remains. In addition, the maximum ORR activity was recorded after only a small number of CV-ORR cycles. Much of the bulk Co was still present at this time, as shown in the first XRD trace recorded after RDE testing (for example 6 cycles). It is therefore possible that loss of bulk Co is actually detrimental to ORR activity, although more work is required to determine whether this is the case as time-dependent electrolyte contamination also plays a role in the observed ORR activity loss.

5.5 Chapter Summary and Conclusion

A series of $Pt_{1-x}Co_x$ and $Pt_{1-x}Ni_x$ dealloy catalyst precursor films were deposited onto a range of substrates, including NSTF-coated GC disks, by high throughput sputter deposition techniques. The composition ratio of M (M = Co, Ni) were selected to be high in order to examine the dealloying process. The catalyst films were examined by a RDE protocol that foregoes electrochemical cleaning in order to track the performance indicators (SEF and ORR current densities) over number of CV cycles.

Intermixed $Pt_{1-x}Ni_x$ ($0.65 < x < 0.75$) materials supported on NSTF-coated GC disks showed an initial SEF of ~ 20 cm^2/cm^2. While the SEF for sputtered Pt showed a steady level around 14 cm^2/cm^2 throughout the experiment, the SEF of $Pt_{1-x}Ni_x$ material showed

a rapid increase for the first few test blocks before plateauing. Catalysts with higher Ni content showed higher SEF plateau values, with $Pt_{25}Ni_{75}$ being the highest, showing a SEF of ~ 50 cm^2/cm^2 at the end of 14^{th} test block. The area-specific ORR activity, $j_{specific}$ at 1000 mV_{RHE}, was shown to be as high as ~ 0.15 mA/cm^2 for $Pt_{1-x}Ni_x$ catalysts at the beginning of the test sequence. This dropped towards ~ 0.05 mA/cm^2 as the tests continued for 9 hours. Sputtered Pt, for comparison, reached 0.03 mA/cm^2 at the beginning of the test sequence; this activity had dropped to ~ 0.02 mA/cm^2 after multiple CV-ORR blocks.

The trends in SEF and $j_{specific}$ of the $Pt_{1-x}Ni_x$ material agreed with the current understanding of the dealloying process and its impact on catalytic performance. In a corrosive environment, the less noble metal of the $Pt_{1-x}Ni_x$ alloy should dissolve easily. The dissolution of Ni probably started with surface and near-surface Ni atoms, forming a porous structure that has high surface area, increasing SEF. The dissolution of Ni likely created a thin Pt-rich outer layer with a different lattice constant than the Ni-rich core. This structure was shown to have high ORR activity. As dealloying continued, the Pt-rich outer layers may increase somewhat in thickness, leading to decline in area specific current density. However, their thickness must be less than 2 nm, because no evidence for pure Pt was observed in XRD experiments. The Pt-enriched outer layer shell also seems to protect Ni atoms from the deeper bulk regions of the catalyst from dissolution by limiting diffusion of Ni to the surface. This was demonstrated by XRD measurements which showed bulk de-alloying occurred at a relatively slow rate with multiple potential cycles.

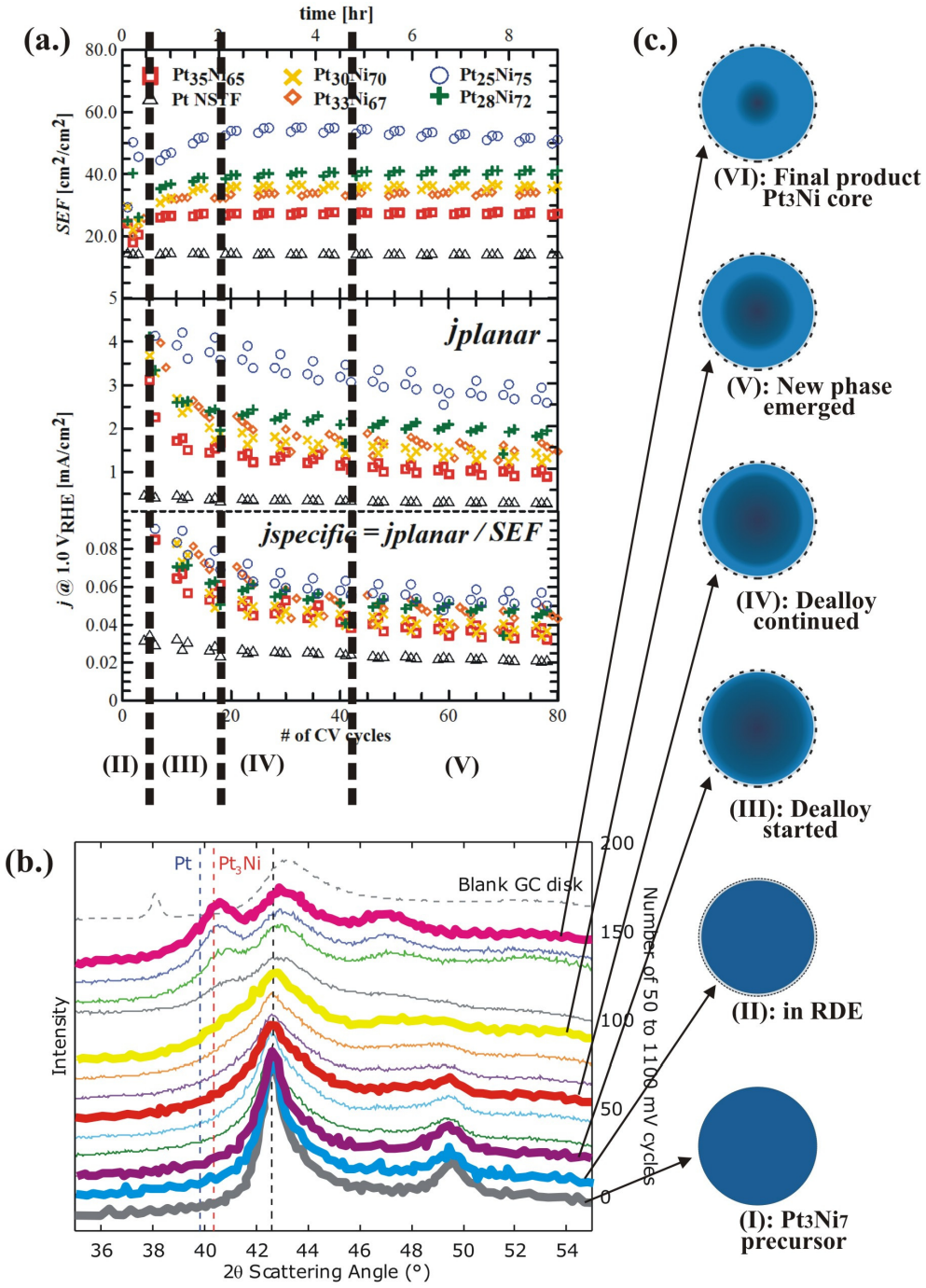

Figure 5-18 A summary of Pt_3Ni_7 dealloying process examined at various points along the continuous RDE protocol. (a) shows all of the electrochemical measurements, (b) shows the XRD measurements and (c) shows a series of diagrams of the likely configurations of the catalyst particles with the dashed lines indicate a rough surface due to dealloying.

A summary of the Pt_3Ni_7 dealloying process examined at various points along the continuous RDE protocol is shown in Figure 5-18. Figure 5-18a shows all of the electrochemical measurements from previous figures (Fig. 5-10 and 5-12). Figure 5-18b shows the XRD measurements (from Fig. 5-11) and Figure 5-18c shows a series of diagrams of the likely configurations of the catalyst particles at various stages. Prior to the RDE measurements, the composition of catalyst particles were Pt_3Ni_7 (Fig. 5-18c part I), shown in the XRD data as a contracted Ni-substituted FCC Pt lattice (first scan in Fig. 5-18b). Once the electrode is placed in the RDE cell, the surface Ni dissolved away, resulted in a thin, Pt-rich shell that was slightly rougher than the original precursor (Fig. 5-18c part II). Although the overall composition did not change (second scan in Fig. 5-18b), the SEF of the material was higher than that of pure Pt (Fig. 5-18a part II). During the first 20 CV cycles of the RDE protocol, the surface and near-surface Ni dissolved and resulted in a rapid increase in SEF (Fig. 5-18a part III) without significant changes in the overall alloy composition (third scan in Fig. 5-18b). As the dealloying process continued, Ni atoms from the core continued to migrate to the surface and dissolved (Fig. 5-18c part IV), shown in the XRD scans as a decrease in the peak intensity (sixth scan in Fig. 5-18b). During this time, the surfaces of the particles were configured into a more stable, Pt-rich and porous structure and therefore the SEF and $j_{specific}$ started to plateau (Fig. 5-18a part IV). After 40 CV cycles, the surface structure and catalytic activity indicators (SEF and $j_{specific}$) had stabilized (Fig. 5-18a part V) while the loss of Ni atoms from the core resulted in a new phase, Pt_3Ni, that can be seen as an emerging "shoulder" in the XRD scans (ninth scan in Fig. 5-18b). In the end, the core composition of the particles

became predominantly Pt_3Ni due to loss of Ni, shown in the thirteenth XRD scan Fig. 5-18b.

RDE testing of $Pt_{1-x}Co_x$ ($0.60 < x < 0.75$) showed that these catalysts had significantly higher catalyst surface areas (calculated from the H_{upd} region of CVs) and, more importantly, much higher ORR catalytic activity than platinum of the same loading, with the half-wave potential shifting ~ 30 mV. The ORR activity and catalyst surface area passed through a maximum around x = 0.66-0.67 in $Pt_{1-x}Co_x$. The maximum activity was recorded after only a few CV-ORR cycles. Ex-situ XRD measurements showed that some of the bulk Co had dissolved away at this time, but much of it was still present. Extended CV-ORR cycling resulted in further Co dissolution until, at the end of the test protocol, the overall bulk Co content as indicated by XRD appeared to be less than 25 % (i.e. < $Pt_{0.75}Co_{0.25}$), consistent with our acid wash studies with similarly deposited binary alloys on the NSTF whiskers [128]. This additional loss of Co did not lead to further enhancement of ORR activity, suggesting that further work would be required to ensure that only as much Co is lost as would be required to obtain maximum ORR activity. The high activity of these high transition metal types of catalysts is very appealing; however, stability of performance is a significant issue that would need to be addressed before they could be of practical use for PEM fuel cells.

Chapter 6

The Impact of Dealloying on Surface Area and Morphology

In this chapter, intermixed $Pt_{1-x}Ni_x$ ($0 < x < 0.8$) films were used to study the dealloying process occuring in Pt-Ni. The dealloying process was examined by comparing the anodic and cathodic current from CV or potential hold methods to determine the amount of charge associated with Ni dissolution.

6.1 Ni Dissolution and Coulombic Calibration

In an acidic aqueous solution with $1.0 < pH < 2.0$ (corresponds to $0.1 > \alpha_{H+} > 0.01$, where α_{H+} is the hydrogen ion activity), pure Ni oxidizes to the Ni^{2+} ion and dissolves readily in an applied potential range between -200 and 1800 mV_{RHE} [129-131]. However, the Ni^{2+} ions at the surface of the sample may form NiO and hinder further Ni oxidation. Both Ni $\rightarrow$ Ni^{2+} oxidation and the passivation processes can be examined in a cyclic voltammogram. Information regarding the Ni oxidation potential, as well as the passivation onset potential, can be determined from the CV plot and used to design experiments to obtain a coulombic calibration for the Ni dissolution process.

Ni was deposited by magnetron sputtering onto mirror polished GC disks and measured in a RDE cell without rotation. Figure 6-1 shows a CV between -25 and 1250 mV_{RHE} taken on a pure Ni film deposited on a mirror polished GC disk. The CV started from 1250 mV_{RHE} at 2.0 mV/s rates for two cycles. A high initial potential would lead to the formation of a passivation layer at the Ni surface and protected the Ni films from

dissolving prematurely. During the first cycle (shown with arrows), the negative sweep towards lower potential produced a high, positive current peak that corresponds to oxidation of Ni in the working electrode. The positive current peaked between 100 and 600 mV_{RHE} and was centered at 300 mV_{RHE}. During the reverse sweep, there was also a positive current peak centered at 230 mV_{RHE}. In the second cycle, there were no current peaks in both sweeps. Once the CV measurement was over, the electrode appeared to be a pristine, mirror-polished, GC disk surface and showed no sign of a metal film.

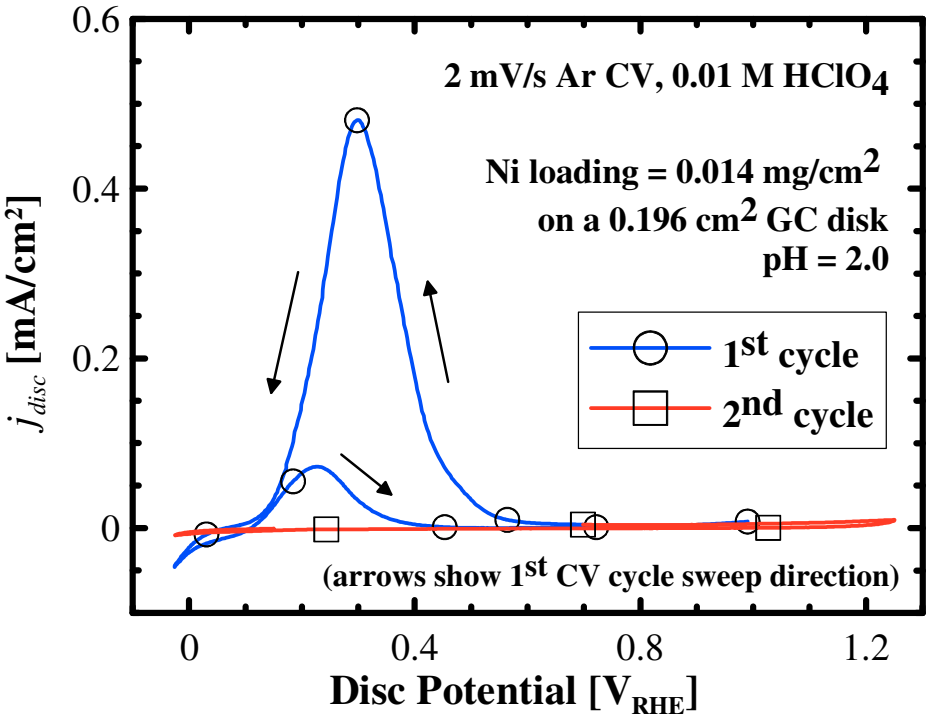

Figure 6-1 2 mV/s CV of a thin Ni film deposited on a mirror-polished GC disk

It is apparent that all of the Ni dissolved in the first CV cycle, resulting in an absence of CV signatures in the second cycle. During the first cycle, the majority of the Ni dissolved in the first sweep towards the lower potential, showing a much higher current peak than the second sweep. The optimum potential for highest Ni → Ni^{2+} oxidation rate appeared

to be between 240 and 300 mV_{RHE}. This agrees with the literature value of the equilibrium potential for $Ni \rightarrow Ni^{2+}$ oxidation being 260 mV_{RHE} [129-131]. At the high potential region ($V > 300\ mV_{RHE}$), the CV showed no oxidation current. This is due to NiO formation at the electrode surface, which passivated any further dissolution at high potential [129], [130].

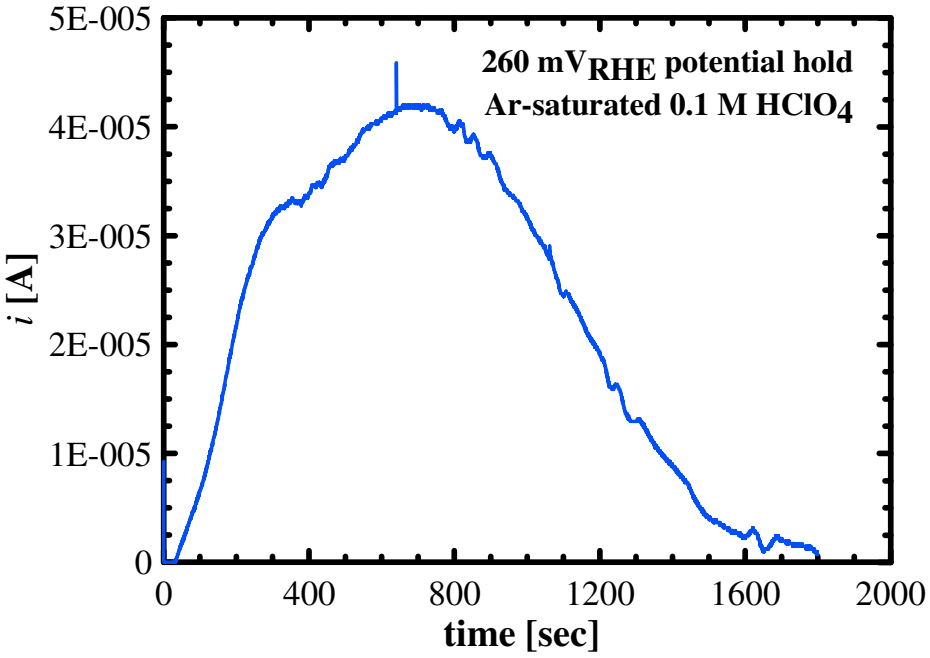

Figure 6-2 Current response during 260 mV_{RHE} potential hold of a thin Ni film

Figure 6-2 shows the measured current plotted as a function of time during a potential hold experiment performed on a thin film Ni sample. The sample was held at 260 mV_{RHE} in the solution cell without rotation. The positive (oxidation) current increased at the beginning of the experiment, signaling an increased rate of Ni oxidation. As the experiment continued, the current reached a peak and decreased to zero within an hour. The Ni was originally sputtered onto a mirror-polished glassy carbon disk with a smooth and, relatively small, surface area. At the beginning of the potential hold experiment, the

surface Ni atoms started to oxidize and dissolve randomly, resulting in an increased roughness of the Ni-electrolyte contacting surface increased. The increase in surface area led to an increase of oxidation reaction rate. As the experiment continued, there was less Ni available for dissolution and the reaction rate eventually decreased to zero. The current vs. time data from the CV and potential hold experiments (PINE system measures time, electrode potential and current) was used to calculate the amount of charge associated with Ni dissolution process. This is shown in Figure 6-3.

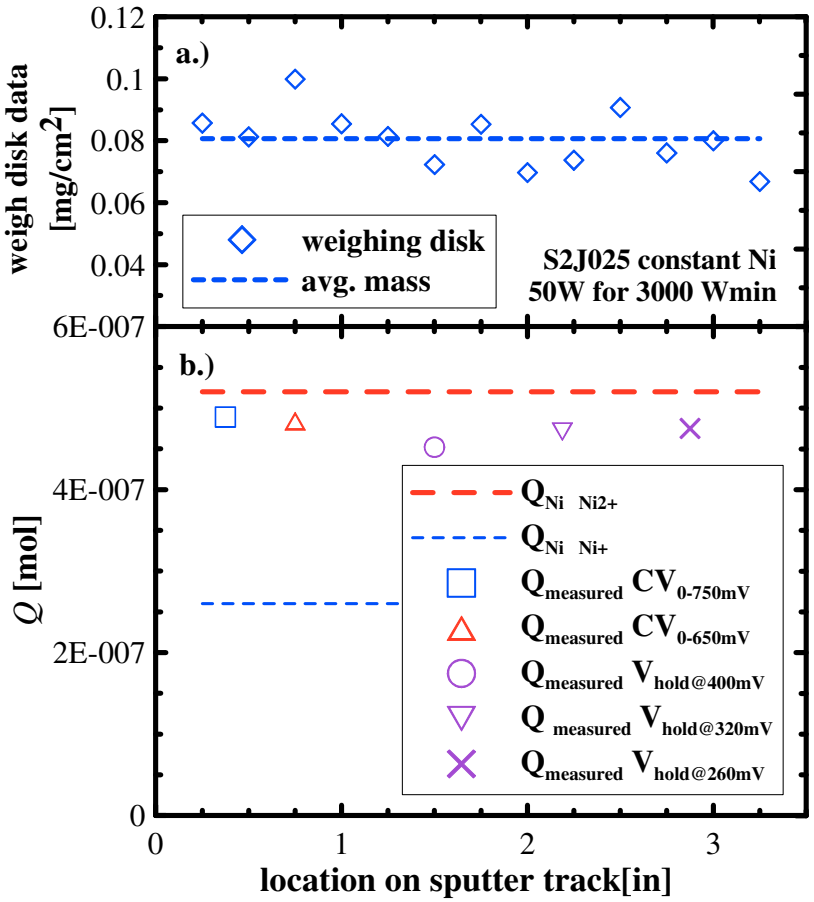

Figure 6-3 Comparison of coulombic collection by CV and V_{hold} method.

Figure 6-3 shows the results of coulombic measurements of Ni dissolution via different methods. In these experiments, a constant Ni film was deposited onto a number of mirror-polished GC disks. The Ni films were then measured by different CV and potential hold schemes. Figure 6-3a shows the sputtered Ni film mass as a function of location along the sputtering track. Ni was sputtered using a power of 50 W in 0.82 mTorr for 3000 W*min. through a constant mask, resulting in a constant deposition of 0.08 mg/cm^2.

The 5.07 mm O.D. GC disks with Ni films were measured by two 5 mV/s CV schemes: 0 ~ 750 mV_{RHE} and 0 ~ 650 mV_{RHE}, and three potential hold schemes: 260 mV_{RHE}, 320 mV_{RHE} and 400 mV_{RHE}. The results of the different measurement schemes are compared in Figure 6-3b. Figure 6-3b shows the charge measured in each scheme compared with the amount of charge expected from $Ni \rightarrow Ni^{1+}$ and $Ni \rightarrow Ni^{2+}$ oxidation reactions in dashed lines. The amount of measured charge was calculated by integrating the measured current over time and converting into moles via Faraday's number. The expected charge for different Ni oxidation states were calculated from the mass data. It is apparent that the Ni films underwent $Ni \rightarrow Ni^{2+}$ during the experiments.

The comparisons of different coulombic measurement schemes above demonstrated that CV between 0 ~ 750 mV_{RHE} at 5 mV/s showed the result that was closest to the predicted values. The next step is to use the 5 mV/s CV to make a calibration curve for Ni dissolution under the same conditions. The results are shown in Figure 6-4.

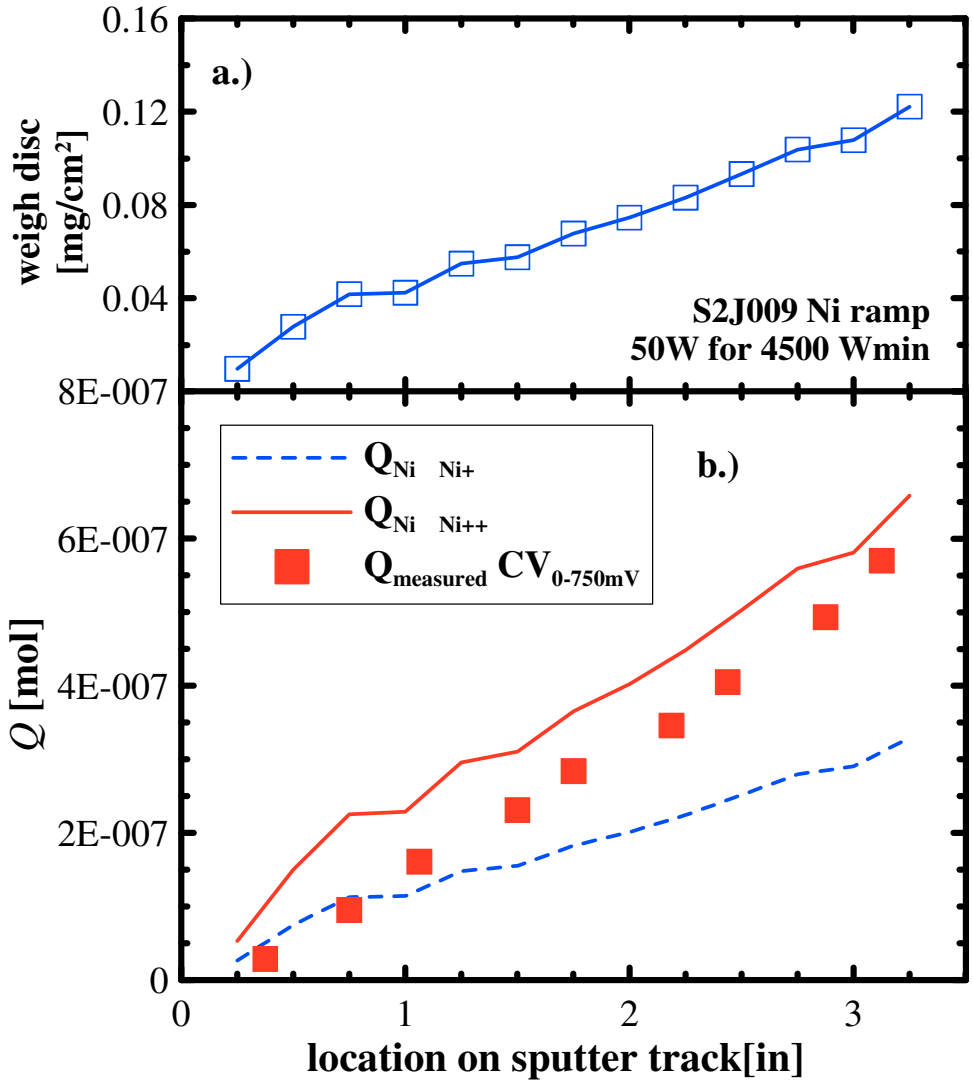

Figure 6-4 Coulombic calibration of a linear Ni thin film ramp.

Figure 6-4a shows the mass data of the sputtering run. The Ni was sputtered through a "linear out" mask using a power of 50 W in 0.82 mTorr of Ar for 4500 W*min. and produced a linear wedge up to 0.12 mg/cm^2. This latter amount is similar to a Ni loading in the dealloying $Pt_{1-x}Ni_x$ catalyst precursors in the previous chapters. For an example, Figure 5-6a shows that a $Pt_{35}Ni_{65}$ catalyst film has 0.15 mg/cm^2 of Pt and 0.16 mg/cm^2 of Ni.

Figure 6-4b shows the results of coulombic measurements during a 0 ~ 750 mV_{RHE} CV at 5 mV/s compared to the calculated values for Ni → Ni^{1+} (dashed line) and Ni → Ni^{2+} (solid line) reaction. The measured data agrees well with the Ni^{2+} oxidation prediction during the CV, as confirmed by the previous coulombic measurements shown in Figure 6-3. Figure 6-4b also shows that the coulombic measurements gave charges associated with Ni dissolution that are lower than the predicted values by a fixed amount, roughly 0.5×10^{-7} moles of electrons. This could be due to either loss of Ni into the solution during the delay between the assembly of the electrode and the start of the measurement, or an over-estimate of the calculated amount due to oxide formation. The "charge loss" could also be the result of charges used to reduce the Ni oxide passivation layers at the beginning of the experiment. The mass data are measured from the weighing disks positioned along the sputtering track. During sputtering, pure Ni is deposited onto the discs. After the sputtering run, the chamber is opened to atmosphere and the top surface of the Ni film would likely form an oxide layer. This would lead to an over-estimate of the mass and higher calculated values associated with Ni dissolution, shown in Figure 6-4.

6.2 Pt_3Ni_7 Dealloying by CV

The coulombic calibration results in previous sections demonstrated little differences between the CV and the potential hold methods in quantifying the Ni dissolution process. The next task was to examine Ni dissolution from a dealloying precursor, Pt_3Ni_7. The Pt_3Ni_7 precursor films were deposited under the same conditions described in section 5.2 with constant masks over both Pt and Ni targets. Both CV and potential hold methods were attempted and are compared in this section.

6.2.1 CV – Low Potential Region (50 ~ 750mV$_{RHE}$)

In the previous CV and potential hold experiments, it was shown that pure Ni oxidized to Ni^{2+} and dissolved readily when a potential of 260 ~ 300 mV$_{RHE}$ was applied. At a higher potential, Ni dissolution was hindered via NiO formation at the electrode surface. A coulombic measurement for the PtNi dealloying process should be tailored using the above information and focus on slow rate (5 mV/s or less) potential sweeps in the low potential regions (less than 750 mV$_{RHE}$). The results for different CV experiments are shown in Figure 6-5.

Figure 6-5 shows CV plots of Pt_3Ni_7 thin catalyst films deposited onto mirror-polished GC disks. Each GC disk has a constant amount of Pt_3Ni_7 film deposited with 0.16 mg/cm^2 of Pt and 0.11 mg/cm^2 of Ni. The details of the sputtering procedures can be found in previous chapters and will not be repeated here. The CV of Pt_3Ni_7 catalyst films were measured in RDE cells without rotation. In each CV experiment, a total of 70 continuous CV cycles were measured and all CV experiments started at the high potential limit. Different potential limits were examined via CV, from 25 mV$_{RHE}$ to 460, 550, 660 and 750 mV$_{RHE}$ with the results that were shown in Figures 6-5a, b, c and d, respectively. It is apparent that none of the Pt_3Ni_7 catalyst films tested underwent the dealloying process during the CV measurements because the hydrogen H_{upd} region did not incur meaningful change, including the formation of high surface area Pt, throughout 70 CV cycles.

In the previous chapter, it was demonstrated that dealloying of the high M content PtM precursor results in a porous surface structure that has high surface area. Therefore, an absence of increasing SEF in Figure 6-5 indicates no dealloying process took place. Visual inspection of the electrode after the CV measurements also confirmed that the electrode still had a smooth, shiny metal film. Performing CV over the lower potential regions (Figures 6-5a and b) reduced the effect of passivation layer formation during higher potential scans and increased the chances of Ni dissolution near ~ 260 mV_{RHE}. Therefore, the data presented in Figure 6-5 are conclusive evidence suggesting that no dealloying took place during the experiment.

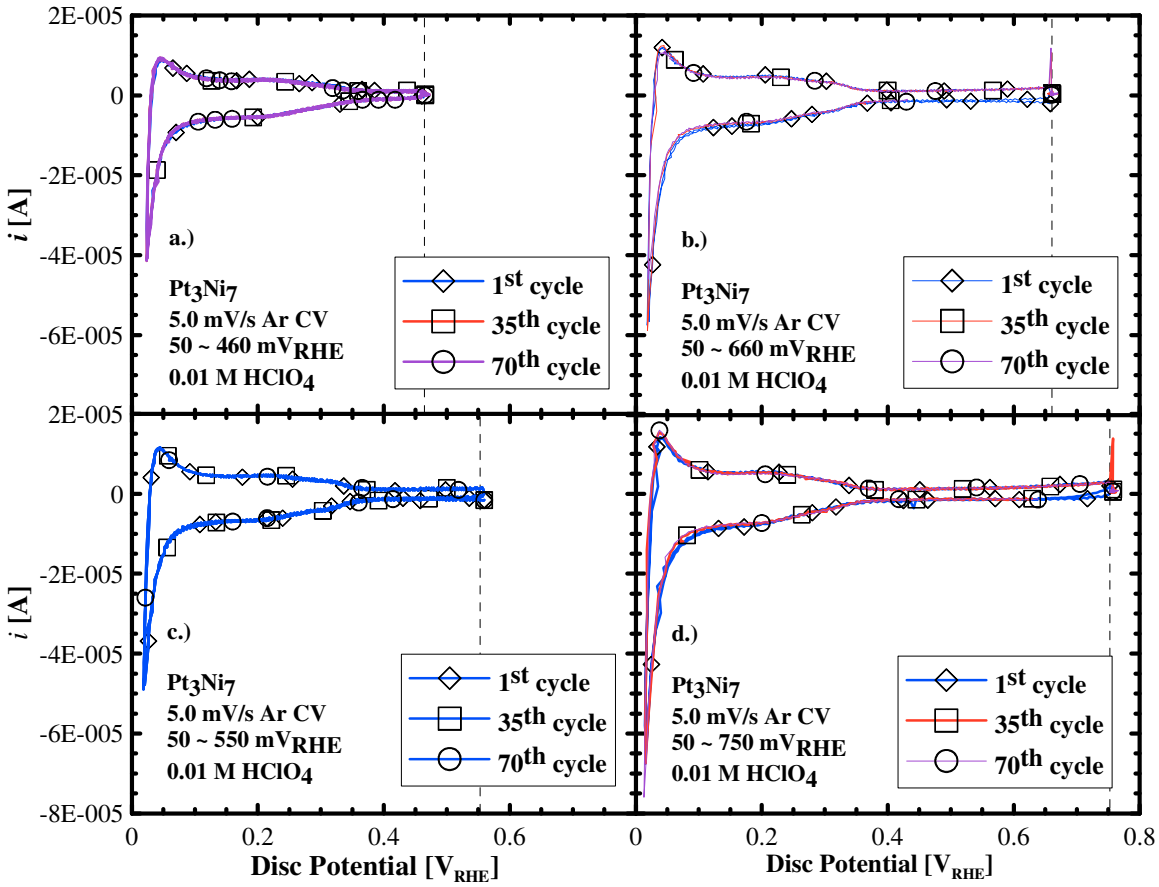

Figure 6-5 5mV/s CV of Pt_3Ni_7 dealloy precursor in the low potential regions shows no signs of SEF increasing.

The lack of dealloying during the low potential region CVs, coupled with the confirmation of pure Ni oxidation / dissolution in the same potential region, signals that Ni is immobile / stabilized by the presence of noble metal, Pt. This notion is in agreement with the concept of a "critical potential", or a "dealloying potential" of alloy-dealloying phenomenon presented in an earlier chapter. The corrosion potential threshold of the alloy material depends on its composition: if the noble (Pt) content is higher, the critical potential for triggering the dealloying process is also higher. With 30% Pt, it is unlikely that the material can undergo Ni oxidation / dissolution at the same potential as pure Ni.

6.2.2 CV – High Potential Region (650 ~ 1250mV$_{RHE}$)

The previous section demonstrated that no dealloying took place during low potential CVs. Next, focus shifted to high potential region CVs. CVs were made between 650 and 1250 mV$_{RHE}$ at 5 mV/s. A continuous protocol was setup to measure CVs of the Pt_3Ni_7 material at the RDE electrode. The protocol used alternating 5 mV/s CVs in the high potential region (650 ~ 1250 mV$_{RHE}$) and fast, 50 mV/s, CVs in the low potential region (50 ~ 650 mV$_{RHE}$). The protocol is shown as a function of electrode potential versus time in Figure 6-6. The five repeats of 5 mV/s CVs in the high potential region (650 ~ 1250 mV$_{RHE}$) were used to trigger the dealloying process, and were followed by a single 50 mV/s CV in the low potential region (50 ~ 650 mV$_{RHE}$) to measure the SEF. This sequence is called a "test block". The protocol then repeated the five 5 mV/s CVs with a single 50 mV/s SEF measurement continuously. The results are shown in Figures 6-7 and 6-8.

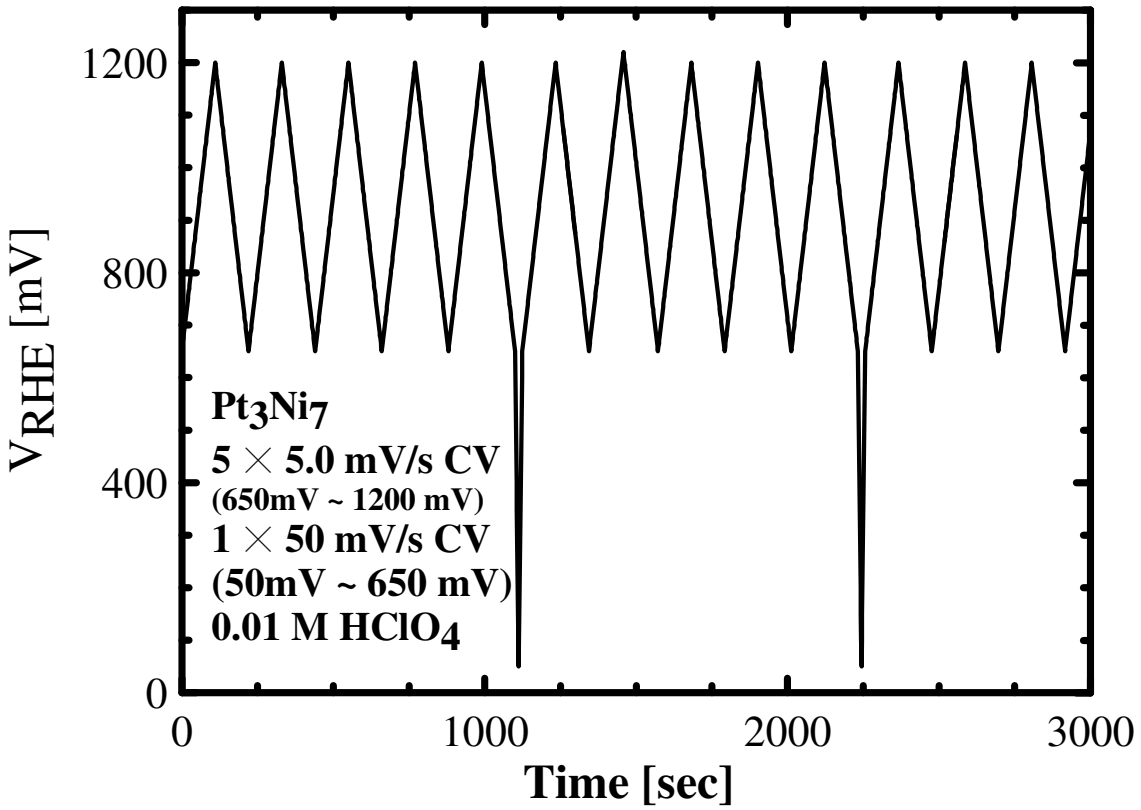

Figure 6-6 CV protocol for scanning high potential regions consisted of five 5 mV/s cycles before a 50 mV/s cycle to check SEF

Figure 6-7 shows the results of 5 mV/s high potential region CVs. In this experiment, the Pt_3Ni_7 catalyst film was examined by 26 continuous test blocks over 9 hours. For clarity, Figure 6-7 only shows every 10^{th} high potential region 5 mV/s CV. The areas of the CV plots increased as the experiment progressed. This corresponds to an increase in electrode roughness and suggests dealloying of the precursor material took place during the experiment.

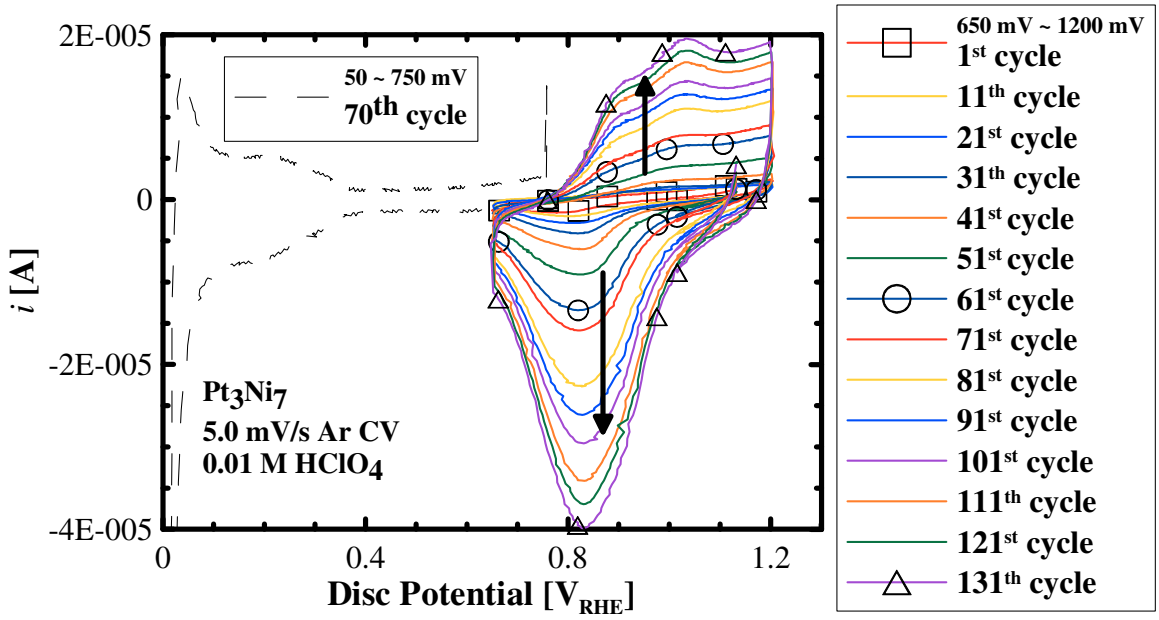

Figure 6-7 Results of high potential region CVs (every 10th cycle is shown here) on Pt_3Ni_7

Figure 6-8 shows the SEF measurements in the lower potential region. All of the 50 mV/s CVs are shown in Figure 6-8a. For clarity, the legend of Figure 6-8a only shows even numbered test blocks (every ten 5 mV/s CVs). The H_{upd} CV area of the catalyst material increased during the experiment. Figure 6-8b shows the SEF calculated from the CV plots in Figure 6-8a as a function of 5 mV/s CV cycle numbers. The SEF values increased continuously from ~ 1.5 cm^2_{Pt}/cm^2_{geo}, at the beginning of the experiment, to ~ 20 cm^2_{Pt}/cm^2_{geo} after 130 cycles. The data from Figures 6-7 and 6-8 suggest that Ni was dealloying from the Pt_3Ni_7 precursor when a potential higher than 650 mV_{RHE} was applied. It was not likely that the dealloying happened during the fast, 50 mV/s CVs that was used to measure the SEF at the end of each test block since it was proved in the previous section that CVs in the H_{upd} potential regions did not trigger the dealloying process. Figure 6-8a also shows slight shifts in the CV features that may correspond to

the Pt(110) surface (at ~ 0.15 V_{RHE}) and the Pt(100) surface (at ~ 0.3 V_{RHE}). However, the shifts in the Pt CV features are likely the results of ohmic contribution, discussed in 5.1.2.

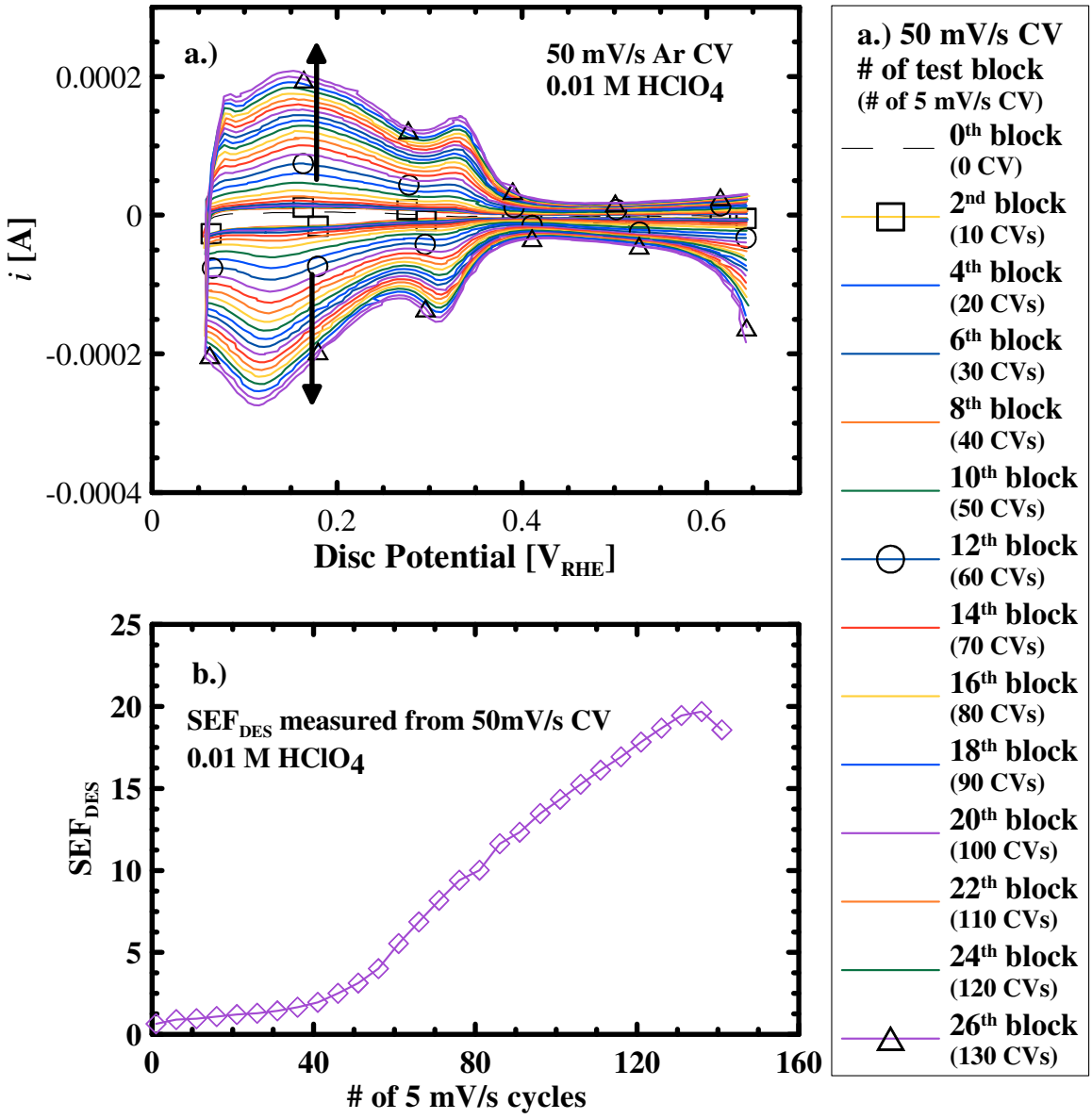

Figure 6-8 Summary of SEF measured in the low potential region CV test blocks. The SEF of the catalyst increased over 130 cycles.

6.3 PtNi Dealloying by Potential Hold

The information gathered from the CV measurements agreed with the dealloying processes described in the earlier chapters. However, in order to accurately measure the charges associated with $Ni \rightarrow Ni^{2+}$ oxidation / dissolution, potential hold methods were used.

Figure 6-9 shows the results of a continuous potential hold experiment on the Pt_3Ni_7 dealloying catalyst electrode. The purpose of this experiment was to obtain preliminary results that would help in designing future potential hold investigations. In this experiment, the electrode underwent 30-minute holds at different potentials ranging from 50 to 1250 mV_{RHE} for over 12 hours. A rapid (50 mV/s) CV in the H_{upd} potential region was used to measure the SEF in the same manner as in the previous section. Not all of the potentials were held for the same duration. The lower potentials that are unable to trigger significant dealloying underwent only one V_{hold} protocol, while higher potentials were measured for multiple V_{hold} cycles.

Figure 6-9a shows the SEF measurements of the preliminary 30-min V_{hold} experiments. It is apparent that no significant increases in SEF were measured for low potential holds ($V < 650mV_{RHE}$). The SEF increase is more apparent with V_{hold} potential greater than 650 mV_{RHE}. This is further confirmed by the %SEF increase for each V_{hold}, shown in Figure 6-9b. Figure 6-9b shows there was little change to the SEF when the applied potential was below 650 mV_{RHE} and that the SEF increased at a higher rate with a higher V_{hold} potential. This finding agrees with earlier CV experiments on the Pt_3Ni_7 material that

showed the dealloying process was only triggered by an applied potential higher than ~ 650 mV_{RHE}. The next set of experiments examines the dealloying with different applied potentials between 750 mV_{RHE} and 1250 mV_{RHE}.

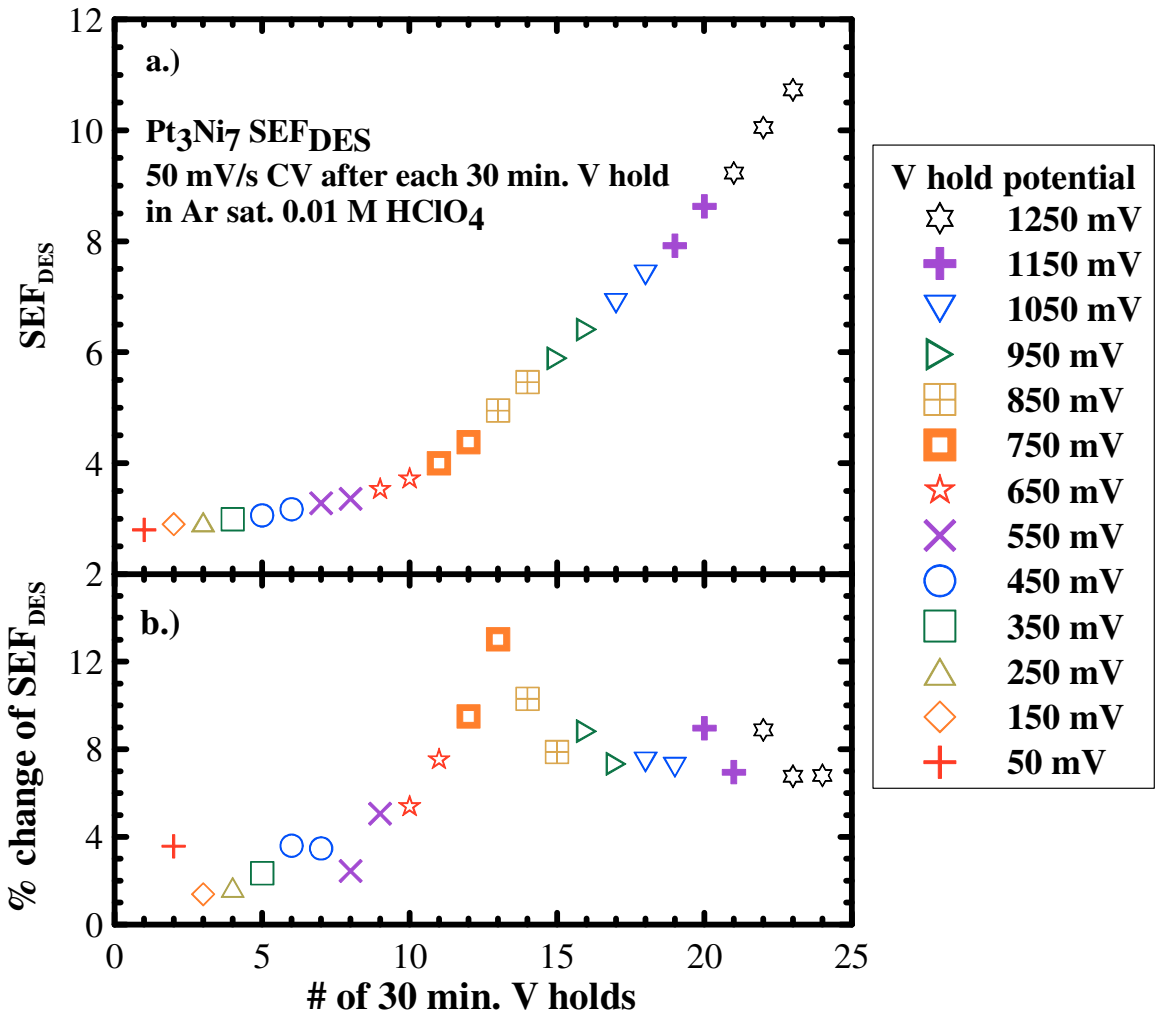

Figure 6-9 *V_{hold} at various low potentials shows no significant change in SEF.*

The information in Figure 6-9 shows an applied 750 mV_{RHE} triggers the dealloying process and is suitable for a coulombic measurement. Figure 6-10 shows a typical potential hold experiment. First, the RDE cell is purged with the Ar for 15 minutes. During the CV-V_{hold} experiment, Ar gas tube was kept flowing above the solution,

effectively forming an "Ar blanket" above the electrolyte solution. At the beginning of the CV measurements, a quick 50 mV/s CV was performed to measure the SEF before the V_{hold} potential was applied for 15 minutes. The CV-V_{hold} protocol was then repeated 140 times over 35 hours. Figures 6-11 and 6-12 show typical current versus time profiles for the repeated CV- V_{hold} measurements.

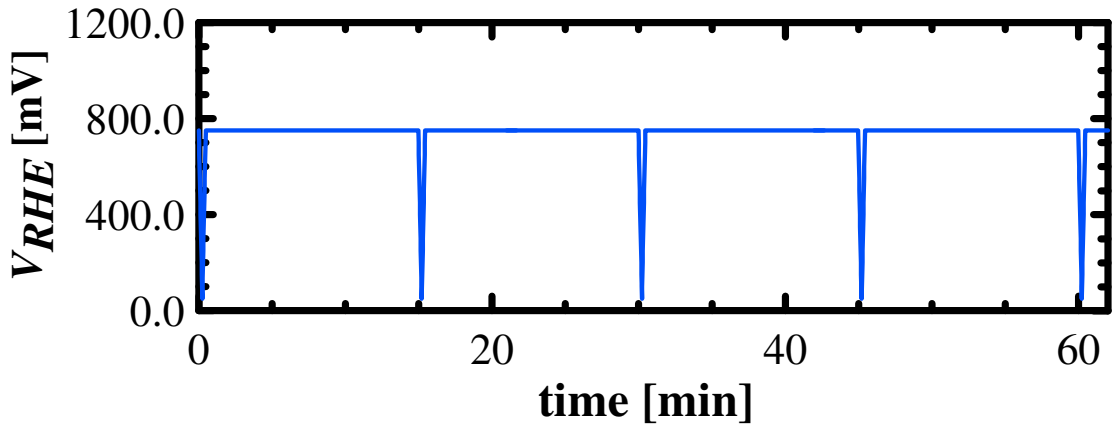

Figure 6-10 A typical potential hold protocol consists of a 50 mV/s CV in the H_{upd} potential region to measure the SEF, then the V_{hold} (750 mV_{RHE} in this case) potential was applied for 15 minutes before the CV-V_{hold} process then repeats.

Figure 6-11 shows the measured current as a function of time for the 750 mV_{RHE} experiments. For clarity, the figure only shows every 10^{th} V_{hold} measurement up to 100^{th} test block, corresponding to roughly every 1.5 hours of V_{hold}, in the main panel of Figure 6-11 while the insert figure shows all measurements. The positive current level associated with Ni oxidation / dissolution is very low at the beginning, shown in Run #1 (solid line with diamond symbol). As the experiment continued, the current level measured during the 750 mV_{RHE} hold increased, reaching 1 μA in Run #40 (solid line with cross symbol) and decreased to near zero around Run #70 (solid line with circle

symbol) and remained zero in the subsequent V_{hold} runs. In between every V_{hold} period is a 50 mV/s CV measured in the H_{upd} region to record the changes in SEF. The results of the 50 mV/s CVs are shown in Figures 6-12 and 6-13.

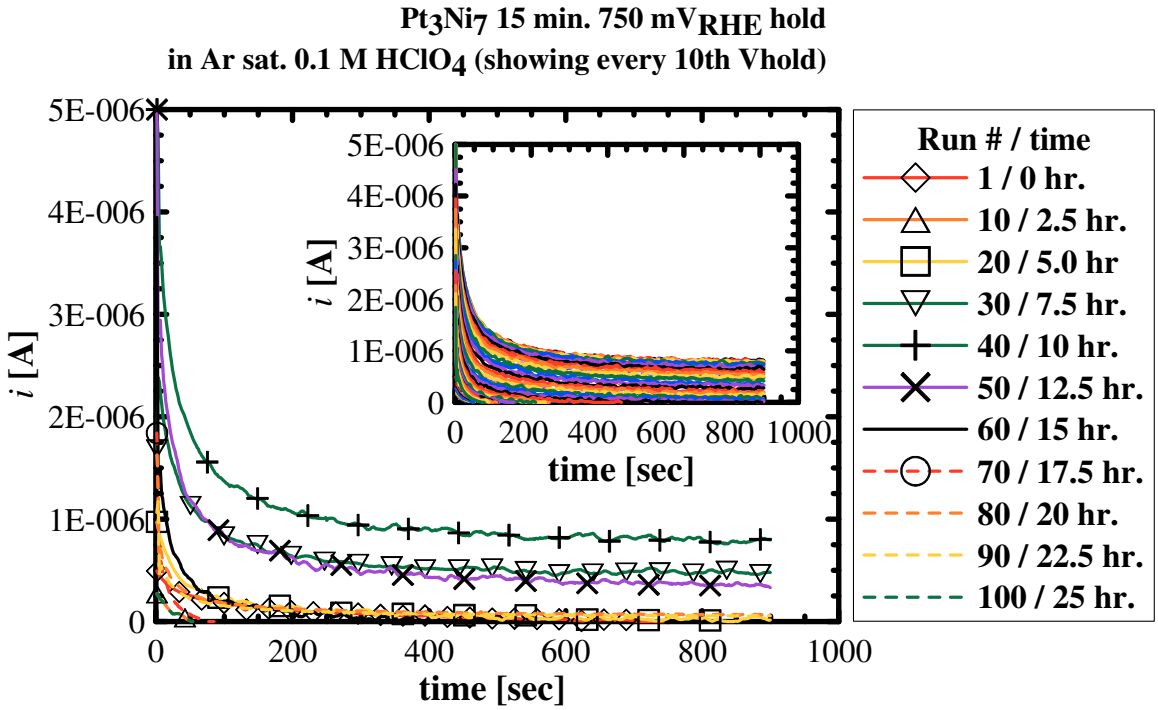

Figure 6-11 I vs. t during the potential hold experiment at 750 mV_{RHE}. For clarity, the figure shows every 10th V_{hold} experiment while the insert shows all measurements.

Figure 6-12 shows 50 mV/s CVs measured between each 750 mV_{RHE} holds. Figure 6-12a shows all 140 CVs. For clarity, Figure 6-12b shows every 10th CV in the same manner as the main panel of Figure 6-11. It is apparent that the H_{upd} region in the CV plots increased significantly as the experiment progressed, reaching a maximum value at ~ Run #50 (solid line with "×" symbol) before declining by a small amount at the end of the experiment, shown in dashed lines. The H_{upd} region in the CV plots for each run was numerically integrated to calculate the SEF values. The SEF value of each 50 mV/s CV

is plotted as a function of cycle number in Figure 6-13. The author also noted that the CV features in Fig. 6-12 are at a slightly different potential than those in of Fig. 6-8. This could be the result of different electrolyte concentration (0.1M and 0.01M for Fig. 6-12 and 6-8).

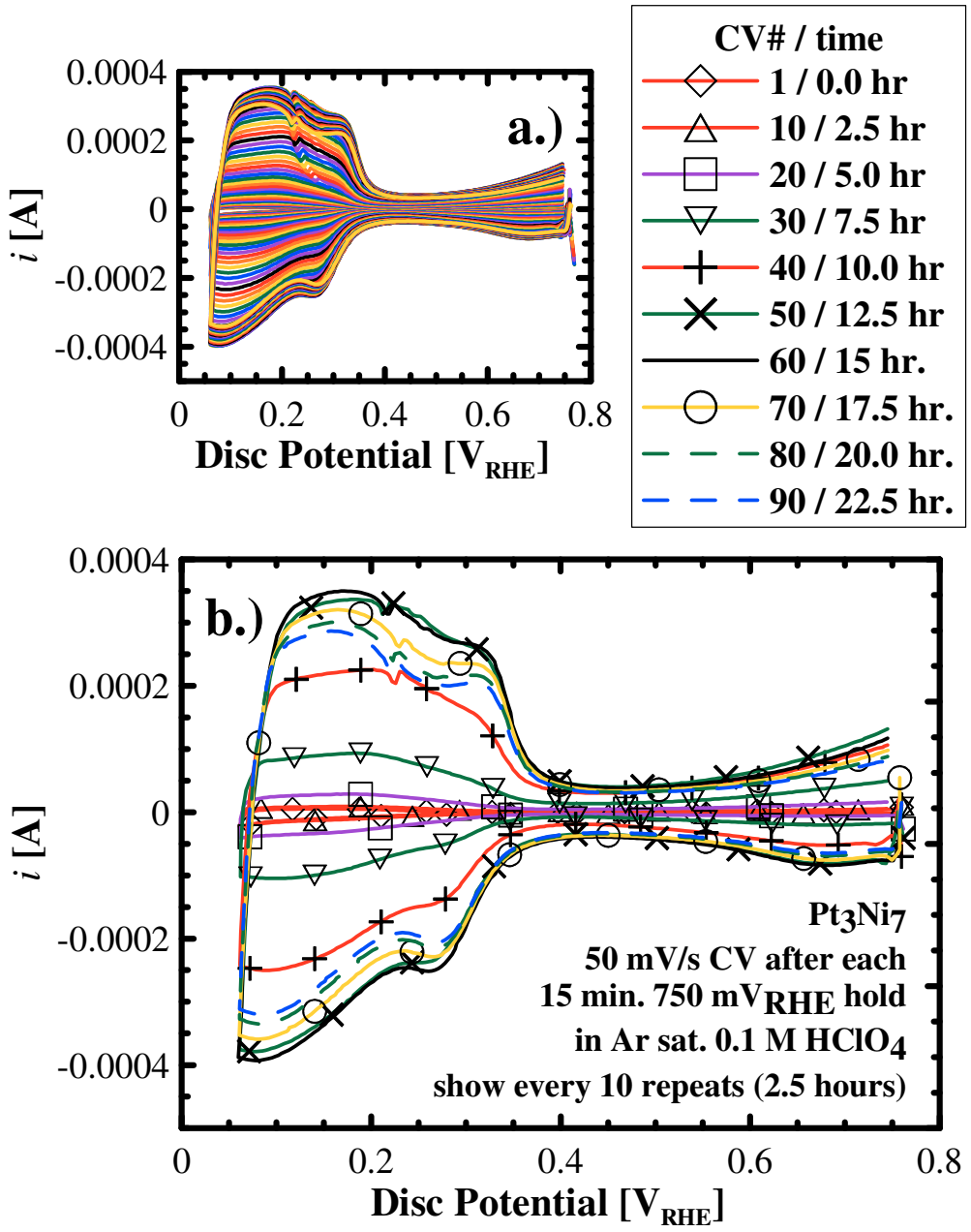

Figure 6-12 SEF check via 50 mV/s CV in H_2 upd region of 750 mV_{RHE} potential hold experiments. For clarity, the figure shows every 10th V_{hold} experiment in (b) while (a) shows all measurements.

Figure 6-13 shows the SEF measured during the 750 mV_{RHE} hold experiment plotted as a function of V_{hold} numbers (bottom axis) and time (top axis), all 140 V_{hold} test blocks are presented in Figure 6-13. The SEF stayed around 2 ~ 3 cm^2/cm^2 at the beginning before increasing steadily, reaching a peak of about ~ 35 cm^2/cm^2 around the 55th potential hold test block (roughly 13 hours). After reaching a peak value, the SEF decreased to ~ 22 cm^2/cm^2. The increase in SEF was likely due to the dealloying process that created a porous surface structure with high surface roughness factor. At the same time, the morphology of the film likely changed as well and could impact the SEF values differently. The morphology changes to the Pt_3Ni_7 films was examined and is discussed in later sections.

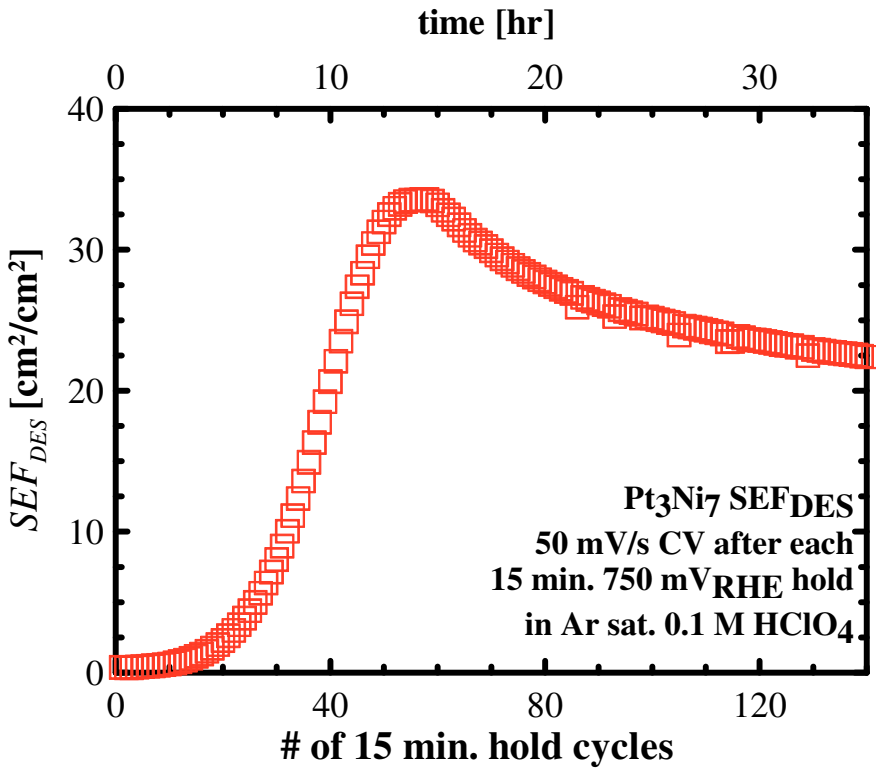

Figure 6-13 SEF trend for V_{hold} experiment on the Pt_3Ni_7 material.

6.4 Impact of the V_{hold} Potential on Dealloying Process

Figure 6-14 shows the results of V_{hold} experiments with various holding potentials between 700 and 1150 mV_{RHE}. The V_{hold} experiments were performed in the same conditions as described in the previous section. The SEF values calculated from the 50 mV/s CVs are plotted as functions of V_{hold}, in the same manner as in Figure 6-13. The data suggested that the degree of dealloying was impacted by the choice V_{hold} potential. The 700 mV_{RHE} hold did not completely dealloy the material because the maximum SEF in the series was ~ 15 cm^2/cm^2 while the rest of the V_{hold} potentials resulted in peak SEF values between 30 to 45 cm^2/cm^2. The effect of different V_{hold} potentials was examined further in Figure 6-15.

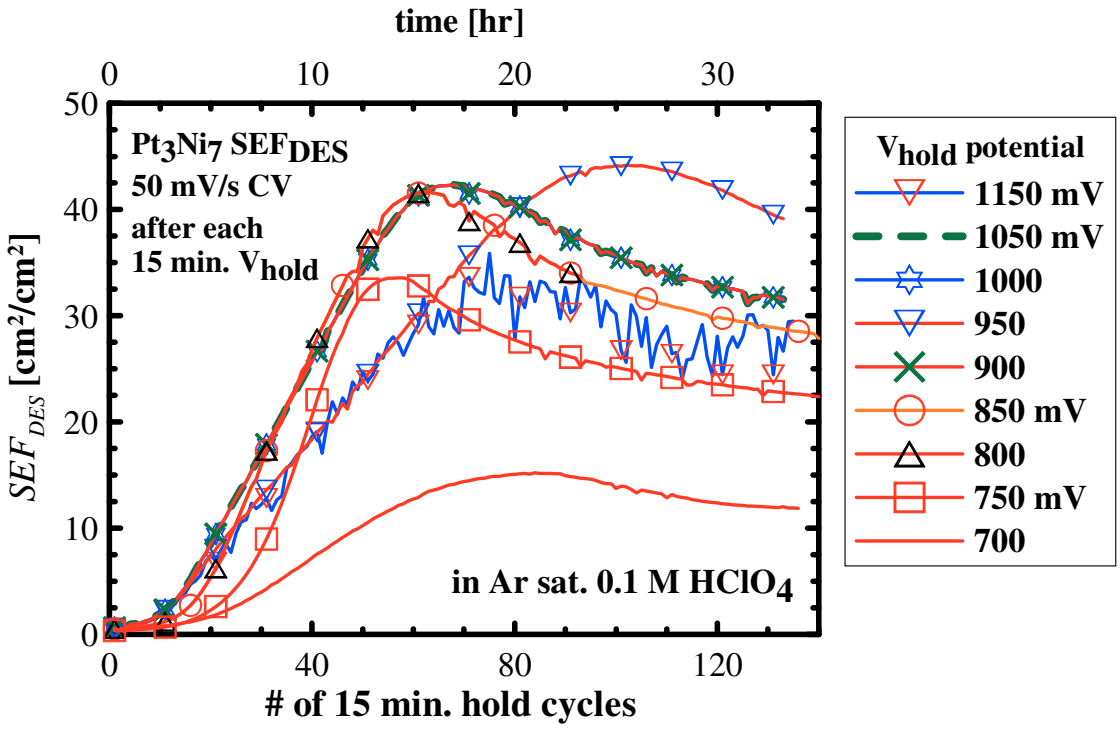

Figure 6-14 SEF trend for all V_{hold} experiments on Pt_3Ni_7 material

Figure 6-15 compares the SEF of the first 60 test blocks of the different V_{hold} experiments. The "onset" (within the first 20 V-hold cycles) of dealloying process changed as the V_{hold} potential increased. Consider the region of Figure 6-15 that is highlighted by the dashed oval. The SEF increased at a much slower rate when V_{hold} = 700 V_{RHE} than the rest of the holding potentials. The 750 mV_{RHE} hold (solid line with square symbol) has an onset that was faster than the 700 mV_{RHE}, where as 800/850 mV_{RHE} curves have onsets that were faster than the 750 mV_{RHE} hold. Once V_{hold} is beyond 900 mV_{RHE}, the onset of dealloying, as represented by the rise of SEF versus time, is very similar.

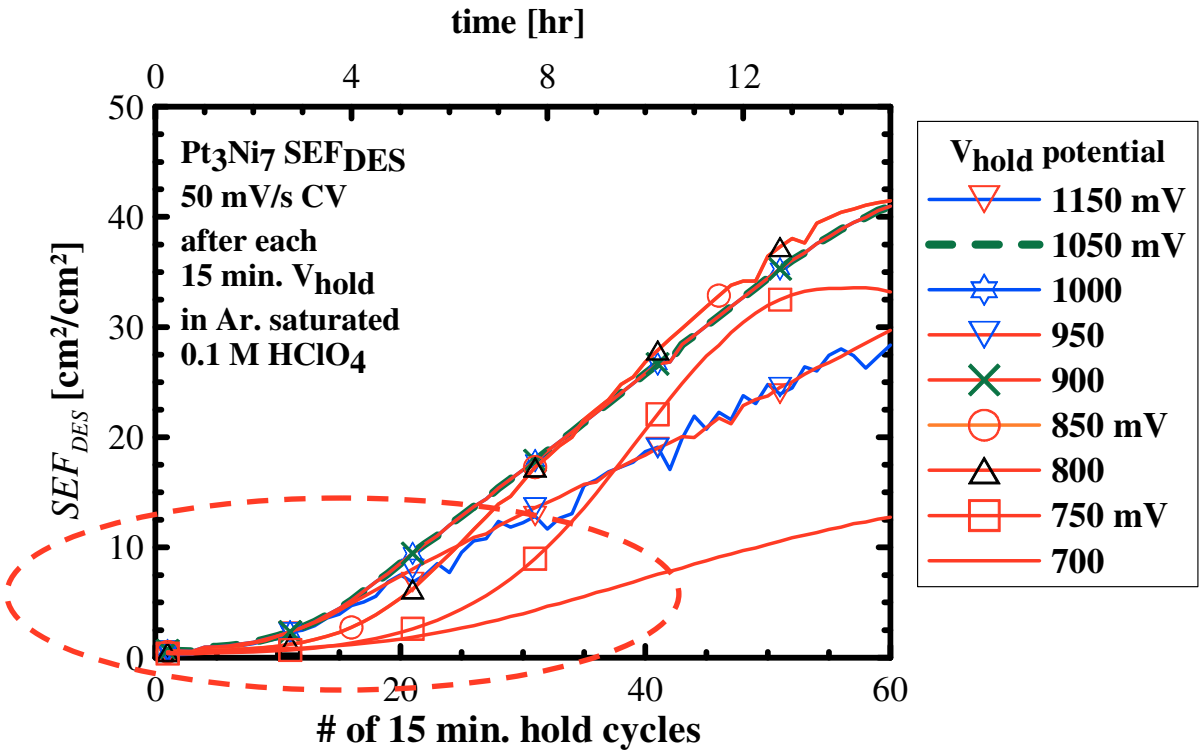

Figure 6-15 SEF trend of all the V_{hold} experiments, focused on the initial V_{hold} periods showing the rate of SEF increase correlates to the V_{hold} potential.

The process of dealloying depends on the precursor composition and the applied potential. In this investigation, the precursor, Pt_3Ni_7, transformed into a structure with high catalytic active area via dealloying. The investigation focused on the relationship between the applied potential and the dealloying process. Dealloying was not triggered in the lower potential region (260 ~ 300 mV_{RHE}), where Ni, the less noble element, oxidized and dissolved readily in its pure state. The subsequent potential hold experiments showed the impact of the applied potential on the onset, as well as the degree of the dealloying process.

A relatively low applied potential, 700 mV_{RHE}, triggered an incomplete dealloying process, signaled by a peak SEF value that was well below those for materials dealloyed at a higher potential. As the applied potential increased, the dealloying process is triggered more quickly and produces peak SEF values as high as ~ 45 cm^2/cm^2 from Pt_3Ni_7 precursor deposited on a mirror-polished glassy carbon disk surface. This should not be confused with the high SEF values obtained in chapter 5, where the Pt_3Ni_7, as well as other high Ni content alloy precursors, were originally deposited onto NSTF-coated disks with a proven geometric SEF of 14 ~ 15 cm^2/cm^2 (chapter 4).

6.5 Morphology Changes of $Pt_{1-x}Ni_x$ Thin Films via Dealloying

Figure 6-16 shows a series of SEM images of fully dealloyed materials, the images were taken at various magnifications. The sputtered Pt_3Ni_7 films were fully dealloyed via 750 mV V_{hold} experiments described in the previous section before they were examined by SEM. The precursor, Pt_3Ni_7, contained a large amount of Ni. Once completely

dealloyed, Ni dissolved away, resulting in a much thinner film that is Pt-rich with a very different morphology compared to the original precursor.

Figures 6-16a ~ 6-16c show the completely dealloyed materials did not resemble the smooth, mirror-polished films, instead, the morphology showed brittle, crumbled and shredded film pieces that did not cover the GC disk surface entirely. Upon closer inspection (Figure 6-16d and 6-16e), parts of the film pieces appeared to be peeled back and rolled up. When examined under high magnification (Figure 6-16f and 6-16g), the surface of the film turned out to form oriented "whiskers". These whiskers are ~ 50 nm in diameter and ~ 500 nm in length, similar in appearance to the NSTF material.

From various literature sources [71], [73], [74], [81], [132], the dealloying process of a binary precursor starts with dissolution of the less noble element, leaving a structure with high porosity that is structurally unstable as the process continues. The structural instability is particularly acute if the precursor material has a very high content of the less noble element. Therefore, upon dissolution of the less noble element, the remaining little amount of noble element would undergo reconstruction to increase the structural stability. Figure 6-16 shows that the Pt_3Ni_7 intermix material dealloyed and restructured itself into a whisker-like morphology that agrees with the current understanding of the dealloying process.

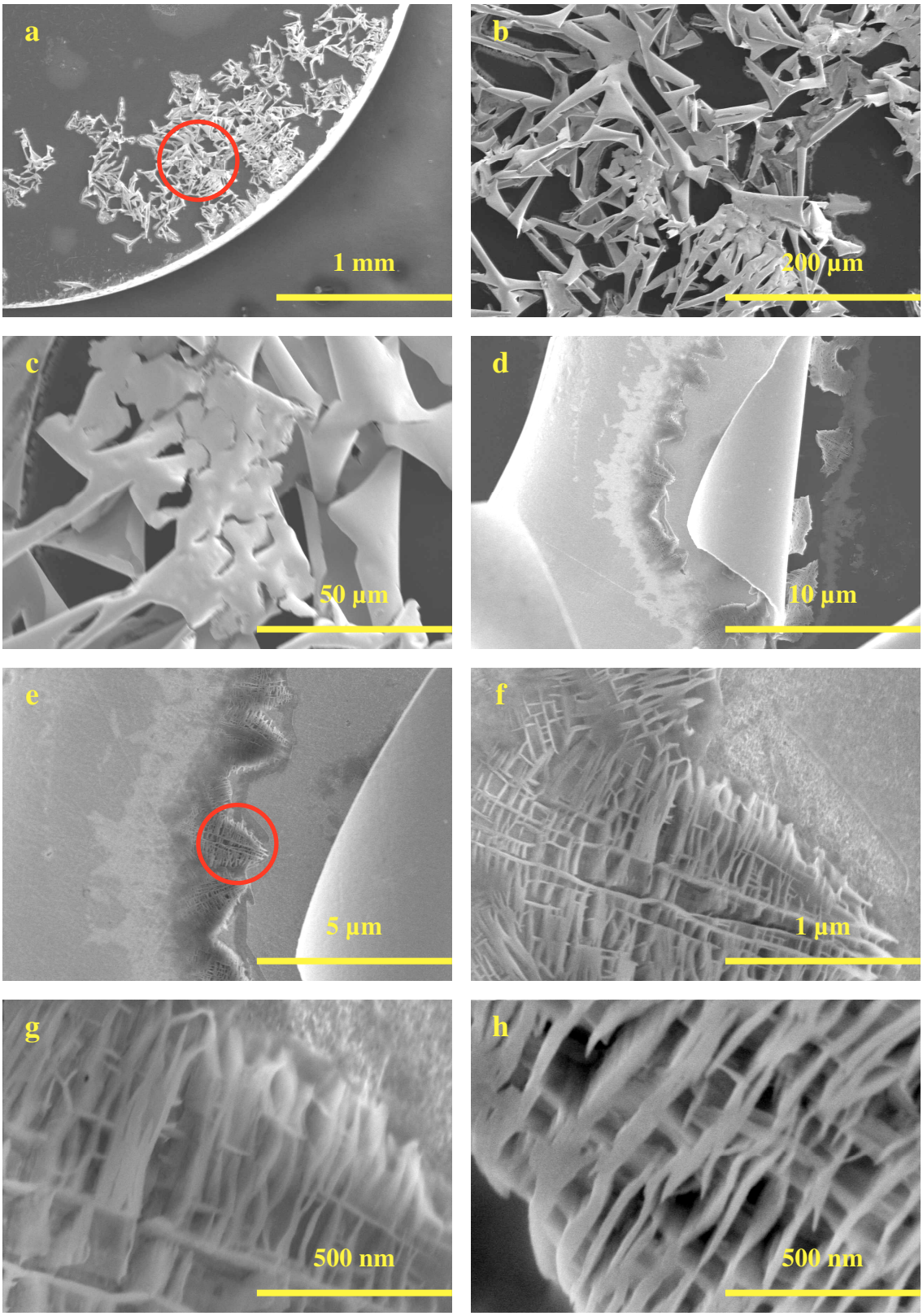

Figure 6-16 SEM images of Pt_3Ni_7 dealloyed at 750 mV_{RHE} for 35 hours. The SEM images taken at different magnification show morphology changes to the thin films.

Chapter 7 Future Work

This thesis presented an improved RDE technique in chapter 4, namely the use of high surface area, NSTF-coated GC disks instead of traditional, mirror-polished, GC disks. With NSTF-coated GC disks, the sputter deposited thin film catalyst material can be tested for both the catalytic activity and the effects of a high-surface area support. As of 2010, most RDE measurements at Professor Jeff Dahn's lab have adopted the NSTF-coated GC disks. Samples prepared on NSTF-coated GC disks have the same morphology, composition and surface structure as the material used in a PEM fuel cell. It is author's opinion that the use of NSTF-coated GC disks is a viable alternative to the traditional, mirror-polished GC disks when testing vapor-deposited thin films. Researchers at Professor Jeff Dahn's lab also adopted NSTF-coated Poco-Graphite (PG) disks as an alternative to NSTF-coated GC disks. PG disks cost less than GC disks and can be manufactured and obtained in much larger quantities. The low cost and abundance of PG disks allows the RDE samples to be stored and archived after RRDE measurements.

Chapter 5 of this thesis examined the ORR activity of two dealloying catalyst libraries: solid-solutions of $Pt_{1-x}Ni_x$ and $Pt_{1-x}Co_x$. The ORR activities were examined with a modified RDE measurement protocol using NSTF-coated GC disks. The modified RDE protocol consisted of repeating Ar/O_2 CV-V_{hold} for up to 8 hours and was well suited to examine the transient, dealloying onset behavior of the catalysts. However, in order to characterize durability-related processes, a much longer protocol is needed with many more Ar/O_2 CV-V_{hold} test blocks repeating up to days or even weeks. Such a prolonged

protocol was not used in this thesis because the catalyst performances showed a significant decline after 4 to 6 hours that is not shown in actual FC MEA testing of identical catalysts at 3M. The origins of the catalytic activity decline during long periods of Ar/O_2 CV-V_{hold} measurement protocol should be investigated and their impact minimized. If contamination is an issue, then perhaps a continuous gravity drip / overflow system can be implemented that cycles dirty electrolyte out of the RDE cell and replaces it with fresh electrolyte. Also, it is likely that a side-reaction of $HClO_4$ breaking down into Cl^- and H_2O occurs during the RDE measurement protocol [108]. The Cl^- ion poisons Pt surfaces and can lead to performance degradation. The poisoned Pt surface can be electrochemically cleaned with a potential bias of 1.3 V_{RHE} applied to the Pt working electrode for 30 seconds.

Chapter 6 offered a quantitative examination of the dealloying process; relatively thick films of Pt_3Ni_7 were deposited onto mirror-polished GC disks and dealloyed in acidic media at various potentials. The series of steps taken in investigating the Pt_3Ni_7 dealloying phenomenon can be a good example for any follow-up work in developing a standard protocol that examines the dealloying process in other Pt-M libraries. Start by examining the electrochemical dissolution potential of the less noble metal, then use slow rate CV at different potential regions to identify the dealloying potential before using continuous "V_{hold} + 50 mV/s CV" to examine the dealloying process at various potentials. Other than the coulometric measurements presented in this thesis, future researchers can examine the dealloying process by a combination of electrochemical solution cells and physical measurements such as XRD, EMP and X-ray photoelectron spectroscopy (XPS).

Although the details of XPS operation are beyond the scope of this thesis, XPS is an excellent technique for measuring the composition of the material at the surface or near-surface. The physical measurements listed above should be used to characterize the catalyst films at different stages of dealloying in the same manner as those presented in chapter 5.

Chapter 8 Conclusions

8.1 $Pt_{1-x}Ir_x$ RDE Measurements with NSTF-coated GC Disks

$Pt_{1-x}Ir_x$ ($0 < x < 0.3$) and pure Pt were sputter-deposited onto mirror-polished and NSTF-coated GC disks and were studied for ORR activity by RRDE. The SEFs of mirror-polished Pt and $Pt_{1-x}Ir_x$ surfaces were around 1.8, depend on the sputtering angle. When the material was deposited onto NSTF-coated GC disks, the SEF were ~14 cm^2_{Pt}/cm^2_{planar}. The SEF of $Pt_{1-x}Ir_x$ films on mirror-polished GC disks were similar to those of pure Pt films on mirror-polished GC disks. By contrast, the SEFs measured for $Pt_{1-x}Ir_x$ catalysts sputtered on NSTF-coated GC disks increased from 15 to 23 cm^2_{Pt}/cm^2_{planar}, reaching a maximum at $x = 0.25$ (in $Pt_{1-x}Ir_x$).

During the ORR measurements, all of the catalyst / support combinations reached the theoretical diffusion-limited current densities. However, NSTF-supported catalysts reached these diffusion-limited current densities at a much higher potential than did mirror-polished supported catalysts. After normalizing the data for active Pt surface area, the specific current densities were all the same, regardless of support, and showed the same Tafel slopes. This implied that all of the catalyst / support combinations shared the same active catalytic ingredient, likely Pt. The high SEF measured on NSTF-supported catalysts on GC disks was due to the surface area enhancement (area about 14 ~15 times the planar surface area) provided by the NSTF support and the whiskerette growth mode. The post-RRDE SEM measurements of the GC disks showed that the NSTF structures

remained intact and that the catalyst whiskerettes were clearly visible along the NSTF whiskers. All of this suggests that NSTF-coated GC disks are a viable alternative to the regular mirror-polished GC disks in screening catalyst activities because both the catalytic activities and the effects of the high-surface area support can be examined in a single measurement. In many ways this is a better measurement than using mirror-polished GC disks because the material being measured has the same morphology, composition and surface structure as the material that would be used in a PEM fuel cell.

8.2 ORR Activity of Dealloyed $Pt_{1-x}M_x$ (M = Ni, Co) Catalyst

A series of $Pt_{1-x}Co_x$ and $Pt_{1-x}Ni_x$ dealloy catalyst precursor films were deposited onto a range of substrates, including NSTF-coated GC disks, by high throughput sputter deposition techniques. The composition ratio of M (M = Co, Ni) was selected to be high in order to examine the dealloying process. The catalyst films were examined by a RDE protocol that foregoes electrochemical cleaning in order to track the performance indicators (SEF and ORR current densities) over a number of CV cycles. Both libraries showed similar ORR performance trends that indicated dealloying was taking place. The SEF of $Pt_{1-x}M_x$ material showed a rapid increase during the first few test blocks before plateauing. Catalysts with higher M content showed higher SEF plateau values, with $Pt_{25}Ni_{75}$ being the highest, showing a SEF of ~ 50 cm^2/cm^2 at the end of 14^{th} test block while the SEF for sputtered Pt showed a steady level around 14 cm^2/cm^2 throughout the experiment. The area-specific ORR activity, $j_{specific}$ at 1000 mV_{RHE}, was shown to be as high as ~ 0.15 mA/cm^2 for catalysts at the beginning of the test sequence and dropped steadily as the tests continued for 9 hours.

The trends in SEF and $j_{specific}$ of the $Pt_{1-x}M_x$ material agreed with the current understanding of the dealloying process and its impact on catalytic performance. In a corrosive environment, the less noble metal of the $Pt_{1-x}M_x$ alloy should dissolve easily. The dissolution of M atoms probably started with surface and near-surface M atoms, forming a porous structure that had high surface area, increasing SEF. The dissolution of M atoms likely created a thin Pt-rich outer layer with a different lattice constant than the M-rich core. This structure was shown to have high ORR activity. As dealloying continued, the Pt-rich outer layers may increase somewhat in thickness, leading to a decline in area-specific current density. However, their thickness must be less than 2 nm, because no evidence for pure Pt was observed in XRD experiments. The Pt-enriched outer layer shell also seems to protect M atoms in the deeper bulk regions of the catalyst from dissolution by limiting diffusion of M to the surface. This was demonstrated by XRD measurements which showed bulk de-alloying occurred at a relatively slow rate with multiple potential cycles.

8.3 Impact of Dealloying on Surface Morphology

Ni and Pt_3Ni_7 dealloying precursors were sputtered onto mirror-polished GC disks and examined via various CV and potential hold experiments in order to quantitatively characterize the dealloying process. First, a coulometric calibration of the pure Ni dissolution process showed that Ni selectively dissolved near 260 mV_{RHE}. At a higher potential, the formation of the passivation layer hinders and terminates any further dissolution. The coulometric calibration also showed that Ni dissolves as Ni^{2+} ions.

Electrochemical dealloying of sputtered Pt_3Ni_7 thin films showed that no dealloying took place when the applied potential was less than 700 mV_{RHE}. Considering that pure Ni dissolves readily with a 260 mV_{RHE} applied potential, Pt_3Ni_7's 700 mV_{RHE} dealloying threshold agrees with the concept of dealloying: noble (Pt) and less noble (Ni) metal solutions have a higher dissolution potential due to the noble element holding the alloy structure together until a "critical potential" is reached. The "critical potential" increases as the atomic ratio of the less noble metal (Ni) decreases. A combination of V_{hold} and rapid 50 mV/s CVs were used to dealloy the Pt_3Ni_7 precursor at different applied potentials. The rapid 50 mV/s CVs were used to measure the SEF as the dealloying process took place.

As the dealloying process continued, a porous structure, enriched with noble metal (Pt), with a high surface area was created. This process was tracked by the SEF. During dealloying, the SEF of the planar Pt_3Ni_7 precursor films was as high as 40 ~ 50 cm^2/cm^2. At a lower V_{hold} potential, the rate of SEF increase was relatively slow and increased as the V_{hold} potential increased. This agrees with the concept of "critical potential", below which the material does not participate in dealloying process. The post-dealloying SEM examination of the material showed that after the majority of Ni dissolved away, the surface structure shows an oriented, high aspect ratio, "whisker-like" structure similar to that of NSTF.

In 2011, the dealloying catalysts mentioned in this thesis were tested in fuel cells by researchers at the 3M Company. Debe et. al. recently reported that $Pt_{1-x}Ni_x$ was found to

be unique in showing an extraordinarily sharp peak in ORR activity as a function of the as-made composition around x = 0.69 $\pm$ 0.02 [133]. This composition gave a corresponding fcc lattice parameter of 3.71 Angstroms and a grain size of 7.5 nm. Both surface area and specific activity increases contribute to the increased mass activity of the resultant dealloyed films. By contrast, $Pt_{1-x}Co_x$ shows a diminished but still sharply peaked mass activity in 50 cm^2 tests near x = 0.62 by electron microprobe.

In the 2011 Debe et al. report [133], the $Pt_{0.31}Ni_{0.69}$ catalyst precursor material, supported on NSTF, was tested in a 50 cm^2 fuel cell at various operating conditions and compared with that of $Pt_{0.7}Co_{0.25}Mn_{0.05}$, a standard catalyst material. The $Pt_{0.31}Ni_{0.69}$ catalysts showed a higher current density at 900 mV_{RHE} (35 ~ 40 mA/cm^2) than the $Pt_{0.7}Co_{0.25}Mn_{0.05}$ catalyst (20 ~ 30 mA/cm^2). However, when the materials were compared at a lower potential (600 mV_{RHE}), the PtNi catalyst showed 1.2 A/cm^2 while the standard PtCoMn catalysts showed 1.4~1.6 A/cm^2. It was clear that the PtNi dealloy catalyst performed better at a higher potential but did not maintain the advantages at a lower potential. This could be the result of "flooding" in the nano-size pores during the high current operating condition. When the $Pt_{0.31}Ni_{0.69}$ catalyst was used in a PEMFC, the material had a nano-porous, high surface area surface structure that showed higher activity in the 900 mV_{RHE} test results. At 900 mV_{RHE}, the current and the rate of ORR reaction was low enough for the timely removal of H_2O from the nano-size pores. At 600 mV_{RHE}, the FC operating current and the H_2O production rate were orders of magnitude higher than at 900 mV_{RHE} and thus the nano-size pores could be flooded and this lowered the overall activity.

In 2011, Wagner et al. reported the TEM and SEM comparisons of PtMnCo catalyst supported on NSTF at various stages of a PEMFC operating life cycle [134]. The PtMnCo whiskerettes were examined by SEM and TEM before the PEMFC was "aged" by 30,000 potential cycles between 0.6 and 1.0 V. The SEM and TEM images, as well as SEF and $j_{specific}$ of the NSTF-supported catalysts and Pt/C catalysts were compared to see the impact of aging on the catalyst material. At the end of aging, the SEF of NSTF-supported catalyst showed a 20% reduction while the Pt/C catalyst showed 70% reduction. When comparing the TEM images, both types of catalysts showed signs of Ostwald ripening after 30,000 cycles of aging. This suggested that, although better than conventional Pt/C in SEF retention, the catalysts supported on NSTF material are susceptible to conventional Ostwald Ripening mechanisms nonetheless. This suggests that the benefit of the dealloying catalysts may be lost as Ostwald ripening occurs over the lifetime of a fuel cell.

As demands for better PEMFC catalysts increases, the high ORR activities of core-shell PtNi and PtCo catalysts, enhanced by the dealloying process, are good candidates for fuel cell commercialization. However, many challenges remain including the durability of the catalyst and flooding of dealloyed nano-porous structures in the FC MEA during high current output operations.

References

[1] R. O'Hayre, S.-W. Cha, F. B. Prinz, and W. Colella, *Fuel Cell Fundamentals*, 1st ed. Wiley, 2005.

[2] J. Larminie and A. Dicks, *Fuel Cell Systems Explained*. John Wiley & Sons Canada, Ltd., 2000.

[3] W. Vielstich, A. Lamm, and H. A. Gasteiger, *Handbook of Fuel Cells: Fundamentals, Technology, Applications*, 1st ed. Wiley, 2003.

[4] C. E. Thomas, "Fuel cell and battery electric vehicles compared", *International Journal of Hydrogen Energy*, **34** (15), 6005-6020 (2009).

[5] A. Arce, A. J. del Real, and C. Bordons, "MPC for battery/fuel cell hybrid vehicles including fuel cell dynamics and battery performance improvement", *Journal of Process Control*, **19** (8), 1289-1304 (2009)

[6] C. E. Sandy Thomas, "Transportation options in a carbon-constrained world: Hybrids, plug-in hybrids, biofuels, fuel cell electric vehicles, and battery electric vehicles", *International Journal of Hydrogen Energy*, **34** (23), 9279-9296 (2009).

[7] G. J. Offer, M. Contestabile, D. A. Howey, R. Clague, and N. P. Brandon, "Techno-economic and behavioral analysis of battery electric, hydrogen fuel cell and hybrid vehicles in a future sustainable road transport system in the UK", *Energy Policy*, **39** (4), 1939-1950 (2011).

[8] "Production, leasing begin for Honda FCX Clarity," *Fuel Cells Bulletin*, **2008** (7), 1 (2008).

[9] "Honda unveils FCX Clarity, 4th-gen home station," *Fuel Cells Bulletin*, **2008** (1), 1 (2008).

[10] "FCX Clarity Specifications - Honda Worldwide." [Online]. Available: http://world.honda.com/FCXClarity/specifications/index.html. Last Accessed: 15-May-2011.

[11] "FCX Clarity News - Honda Worldwide." [Online]. Available: http://world.honda.com/FCXClarity/index.html. Last Accessed: 15-May-2011.

[12] "US DOE Hydrogen Program 2010 Annual Merit Review and Peer Evaluation Report." United State Department of Energy, Dec-2010.

[13] Y. Wang, K. S. Chen, J. Mishler, S. C. Cho, and X. C. Adroher, "A review of polymer electrolyte membrane fuel cells: Technology, applications, and needs on fundamental research," *Applied Energy*, **88** (4), 981-1007 (2011).

[14] J. Milliken et al., "Hydrogen Posture Plan: An Integrated Research, Development and Demonstration Plan." United State Department of Energy, Dec-2006.

[15] J. Li, F. Ye, L. Chen, T. Wang, J. Li, and X. Wang, "A study on novel pulse preparation and electrocatalytic activities of Pt/C-Nafion electrodes for proton exchange membrane fuel cell," *Journal of Power Sources*, **186** (2), 320-327 (2009).

[16] V. Stamenkovic, T. J. Schmidt, P. N. Ross, and N. M. Markovic, "Surface segregation effects in electrocatalysis: kinetics of oxygen reduction reaction on polycrystalline Pt_3Ni alloy surfaces," *Journal of Electroanalytical Chemistry*, **554**, 191-199 (2003).

[17] J. X. Wang et al., "Oxygen Reduction on Well-Defined Core−Shell Nanocatalysts: Particle Size, Facet, and Pt Shell Thickness Effects," *Journal of the American Chemical Society*, **131** (47), 17298-17302 (2009).

[18] A. Garsuch et al., "Alternative Catalyst Supports Deposited on Nanostructured Thin Films for Proton Exchange Membrane Fuel Cells," *J. Electrochem. Soc.*, **157** (2), B187-B194 (2010).

[19] D. S. II, J. J. Spivey, and D. A. B. I, *Fuel Cells: Technologies for Fuel Processing*, 1st ed. Elsevier Science, 2011.

[20] A. Weber, R. Darling, J. Meyers, and J. Newman, "Chapter 7: Mass transfer at two-phase and three-phase interfaces," in *Handbook of Fuel Cells: Fundamentals, Technology, Applications*, vol. 1, W. Vielstich, A. Lamm, and H. A. Gasteiger, Eds. John Wiley & Sons, Ltd., 2003, pp. 47-69.

[21] T. Uma and M. Nogami, "Fabrication and performance of Pt/C electrodes for low temperature H_2/O_2 fuel cells," *Journal of Membrane Science*, vol. 302, no. 1-2, pp. 102-108, Sep. 2007.

[22] C. A. Reiser et al., "A Reverse-Current Decay Mechanism for Fuel Cells," *Electrochem. and Solid-State Letters*, 8 (6) A273 (2005).

[23] D. A. Stevens, M. T. Hicks, G. M. Haugen, and J. R. Dahn, "Ex Situ and In Situ Stability Studies of PEMFC Catalysts," *J. Electrochem. Soc.*, **152** (12) A2309-A2315 (2005).

[24] S. Koh, M. F. Toney, and P. Strasser, "Activity-stability relationships of ordered and disordered alloy phases of Pt3Co electrocatalysts for the oxygen reduction reaction (ORR)," *Electrochimica Acta*, **52** (8), 2765-2774 (2007).

[25] M. Watanabe, K. Tsurumi, T. Mizukami, T. Nakamura, and P. Stonehart, "Activity and Stability of Ordered and Disordered Co-Pt Alloys for Phosphoric Acid Fuel Cells," *J. Electrochem. Soc.*, **141** (10), 2659-2668 (1994).

[26] P. Stonehart, "Development of alloy electrocatalysts for phosphoric acid fuel cells (PAFC)," *J. Appl. Electrochem.*, **22** (11), 995-1001 (1992).

[27] A. Nilsson, L. G. M. Pettersson, B. Hammer, T. Bligaard, C. H. Christensen, and J. K. Norskov, "The electronic structure effect in heterogeneous catalysis," *Catalysis Letters*, **100** (3), 111-114 (2005).

[28] J. K. Norskov, T. Bligaard, J. Rossmeisl, and C. H. Christensen, "Towards the computational design of solid catalysts," *Nat. Chem.*, **1** (1), 37-46 (2009).

[29] F. H. B. Lima et al., "Catalytic Activity−d-Band Center Correlation for the O2 Reduction Reaction on Platinum in Alkaline Solutions," *J. Phys. Chem. C*, **111** (1), 404-410 (2007).

[30] J. Zhang, M. B. Vukmirovic, K. Sasaki, A. U. Nilekar, M. Mavrikakis, and R. R. Adzic, "Mixed-Metal Pt Monolayer Electrocatalysts for Enhanced Oxygen Reduction Kinetics," *Journal of the American Chemical Society*, **127** (36), 12480-12481 (2005).

[31] V. Stamenkovic et al., "Changing the Activity of Electrocatalysts for Oxygen Reduction by Tuning the Surface Electronic Structure," *Angewandte Chemie International Edition*, **45** (18), 2897-2901 (2006).

[32] E. Antolini, J. R. C. Salgado, and E. R. Gonzalez, "The stability of Pt–M (M=first row transition metal) alloy catalysts and its effect on the activity in low temperature fuel cells," *Journal of Power Sources*, **160** (2), 957-968 (2006).

[33] Y. Zhang, Z. Duan, C. Xiao, and G. Wang, "Density functional theory calculation of platinum surface segregation energy in Pt_3Ni (111) surface doped with a third transition metal," *Surface Science*, **605** (15), 1577-1582 (2011).

[34] O. A. Baturina, B. D. Gould, Y. Garsany, and K. E. Swider-Lyons, "Insights on the SO_2 poisoning of Pt_3Co/VC and Pt/VC fuel cell catalysts," *Electrochimica Acta*, **55** (22), 6676-6686 (2010).

[35] F. Maillard, L. Dubau, J. Durst, M. Chatenet, J. André, and E. Rossinot, "Durability of Pt_3Co/C nanoparticles in a proton-exchange membrane fuel cell: Direct evidence of bulk Co segregation to the surface," *Electrochemistry Communications*, **12** (9), 1161-1164 (2010).

[36] H. Schulenburg, J. Durst, E. Müller, A. Wokaun, and G. G. Scherer, "Real surface area measurements of Pt_3Co/C catalysts," *Journal of Electroanalytical Chemistry*, **642** (1), 52-60 (2010).

[37] H. Wu, D. Wexler, and G. Wang, "Pt_xNi alloy nanoparticles as cathode catalyst for PEM fuel cells with enhanced catalytic activity," *Journal of Alloys and Compounds*, **488** (1), 195-198 (2009).

[38] B. Fowler, C. A. Lucas, A. Omer, G. Wang, V. R. Stamenkovic, and N. M. Markovic, "Segregation and stability at $Pt_3Ni(111)$ surfaces and $Pt_{75}Ni_{25}$ nanoparticles," *Electrochimica Acta*, **53** (21), 6076-6080 (2008).

[39] Y. Ma and P. Balbuena, "Pt surface segregation in bimetallic Pt_3M alloys: A density functional theory study," *Surface Science*, **602** (1), 107-113 (2008).

[40] G. Wang, G. Sun, Q. Wang, S. Wang, H. Sun, and Q. Xin, "Effect of carbon black additive in Pt black cathode catalyst layer on direct methanol fuel cell performance," *International Journal of Hydrogen Energy*, **35** (20), 11245-11253 (2010).

[41] M. Kim, J-N Park, H. Kim, S. Song and W-H Lee, "The preparation of Pt/C catalysts using various carbon materials for the cathode of PEMFC", *Journal of Power Sources*, **163** (1), 93-97 (2006)

[42] R.-B. Lin and S.-M. Shih, "Kinetic analysis of the hydrogen oxidation reaction at Nafion film covered Pt-black rotating disk electrodes," *Journal of the Chinese Institute of Chemical Engineers*, **39** (5), 475-481 (2008).

[43] Z. Paal, X. L. Xu, J. Paallukacs, W. Vogel, M. Muhler, and R. Schlogl, "Pt-Black Catalysts Sintered at Different Temperatures: Surface Analysis and Activity in Reactions of n-Hexane," *Journal of Catalysis*, **152** (2), 252-263 (1995).

[44] H. J. Kim et al., "Highly improved oxygen reduction performance over Pt/C-dispersed nanowire network catalysts," *Electrochemistry Communications*, **12** (1), 32-35 (2010).

[45] P. K. Shen and Z. Tian, "Performance of highly dispersed Pt/C catalysts for low temperature fuel cells," *Electrochimica Acta*, **49** (19), 3107-3111 (2004).

[46] H.-W. Wang, R.-X. Dong, H.-Y. Chang, C.-L. Liu, and Y.-W. Chen-Yang, "Preparation and catalytic activity of Pt/C materials via microwave irradiation," *Materials Letters*, **61** (3), 830-833 (2007).

[47] M. Kim, J.-N. Park, H. Kim, S. Song, and W.-H. Lee, "The preparation of Pt/C catalysts using various carbon materials for the cathode of PEMFC," *Journal of Power Sources*, **163** (1), 93-97 (2006).

[48] W. Xu, X. Zhou, C. Liu, W. Xing, and T. Lu, "The real role of carbon in Pt/C catalysts for oxygen reduction reaction," *Electrochemistry Communications*, **9** (5), 1002-1006 (2007).

[49] M. S. Wilson and S. Gottesfeld, "Thin-film catalyst layers for polymer electrolyte fuel cell electrodes," *Journal of Applied Electrochemistry*, **22** (1), 1-7 (1992).

[50] N. M. Rodriguez, P. E. Anderson, A. Wootsch, U. Wild, R. Schlögl, and Z. Paál, "XPS, EM, and Catalytic Studies of the Accumulation of Carbon on Pt Black," *Journal of Catalysis*, **197** (2), 365-377 (2001).

[51] T. Sato, K. Kunimatsu, H. Uchida, and M. Watanabe, "Adsorption/oxidation of CO on highly dispersed Pt catalyst studied by combined electrochemical and ATR-FTIRAS methods: Part 1. ATR-FTIRAS spectra of CO adsorbed on highly dispersed Pt catalyst on carbon black and carbon un-supported Pt black," *Electrochimica Acta*, **53** (3), 1265-1278 (2007).

[52] J. C. Vidal, E. Garcia-Ruiz, and J. R. Castillo, "Strategies for the improvement of an amperometric cholesterol biosensor based on electropolymerization in flow systems: use of charge-transfer mediators and platinization of the electrode," *Journal of Pharmaceutical and Biomedical Analysis*, **24** (1), 51-63 (2000).

[53] Z.-B. Wang, P.-J. Zuo, X.-P. Wang, J. Lou, B.-Q. Yang, and G.-P. Yin, "Studies of performance decay of Pt/C catalysts with working time of proton exchange membrane fuel cell," *Journal of Power Sources*, 184 (1), 245-250 (2008).

[54] K. Promislow and B. Wetton, "PEM Fuel Cells: A Mathematical Overview," *SIAM Journal on Applied Mathematics*, **70** (2), 369 (2009).

[55] I. C. Halalay, S. Swathirajan, B. Merzougui, M. P. Balogh, G. C. Garabedian, and M. K. Carpenter, "Anode Materials for Mitigating Hydrogen Starvation Effects in PEM Fuel Cells," *J. Electrochem. Soc.*, **158** (3), B313-B321 (2011).

[56] A. Ohma, S. Suga, S. Yamamoto, and K. Shinohara, "Membrane Degradation Behavior during Open-Circuit Voltage Hold Test," *J. Electrochem. Soc*, **154** (8), B757-B760 (2007).

[57] S. Chen, H. A. Gasteiger, K. Hayakawa, T. Tada, and Y. Shao-Horn, "Platinum-Alloy Cathode Catalyst Degradation in Proton Exchange Membrane Fuel Cells: Nanometer-Scale Compositional and Morphological Changes," *J. Electrochem. Soc.*, **157** (1), A82-A97 (2010).

[58] I. A. Schneider and S. von Dahlen, "Start-Stop Phenomena in Channel and Land Areas of a Polymer Electrolyte Fuel Cell," *Electrochem. Solid-State Lett.*, **14** (2), B30-B33 (2011).

[59] D. A. Stevens, M. T. Hicks, G. M. Haugen, and J. R. Dahn, "Ex Situ and In Situ Stability Studies of PEMFC Catalysts," *J. Electrochem. Soc.*, **152** (12), A2309-A2315 (2005).

[60] M. K. Debe and R. J. Poirire, "Postdeposition growth of a uniquely nanostructured organic film by vacuum annealing," *Journal of Vacuum Science & Technology A*, **12** (4), 2017 (1994).

[61] M. K. Debe and A. R. Drube, "Structural characteristics of a uniquely nanostructured organic thin film," *Journal of Vacuum Science & Technology B*, **13** (3), 1236 (1995).

[62] M. K. Debe, K. K. Kam, J. C. Liu, and R. J. Poirire, "Vacuum vapor deposited thin films of a perylene dicarboximide derivative: Microstructure versus deposition parameters," *Journal of Vacuum Science & Technology A*, **6** (3), 1907 (1988)

[63] M. K. Debe, "Chapter 45: Novel catalysts, catalysts support and catalysts coated membrane methods," in *Handbook of Fuel Cells: Fundamentals, Technology, Applications*, vol. 3, W. Vielstich, A. Lamm, and H. A. Gasteiger, Eds. John Wiley & Sons, Ltd., 2003, pp. 576-589.

[64] M. K. Debe, A. K. Schmoeckel, G. D. Vernstrom, and R. Atanasoski, "High voltage stability of nanostructured thin film catalysts for PEM fuel cells," *Journal of Power Sources*, **161** (2), 1002-1011 (2006).

[65] A. Bonakdarpour, R. Lobel, S. Sheng, T. L. Monchesky, and J. R. Dahn, "Acid Stability and Oxygen Reduction Activity of Magnetron-Sputtered $Pt_{1-x}Ta_x$ ($0 \leq x \leq 1$) Films," *J. Electrochem. Soc.*, **153** (12), A2304-A2313 (2006).

[66] A. Garsuch et al., "Alternative Catalyst Supports Deposited on Nanostructured Thin Films for Proton Exchange Membrane Fuel Cells," *J. Electrochem. Soc.*, **157** (2), B187-B194 (2010).

[67] D. A. Stevens et al., "Assessing the Pt_{upd} Surface Area Stability of $Pt_{1-x}M_x$ (M = Re, Nb, Bi) Solid Solutions for Proton Exchange Membrane Fuel Cells," *J. Electrochem. Soc.*, **157** (5), B737-B743 (2010).

[68] D. A. Stevens et al., "Characterization and PEMFC Testing of $Pt_{1-x}M_x$ (M = Ru, Mo, Co, Ta, Au, Sn) Anode Electrocatalyst Composition Spreads," *J. Electrochem. Soc.*, **154** (6), B566-B576 (2007).

[69] A. Bonakdarpour, R. Lobel, S. Sheng, T. L. Monchesky, and J. R. Dahn, "Acid Stability and Oxygen Reduction Activity of Magnetron-Sputtered Pt1-xTax ($0 \leq x \leq 1$) Films," *J. Electrochem. Soc.*, **153** (12), A2304-A2313 (2006).

[70] A. Bonakdarpour et al., "Dissolution of Transition Metals in Combinatorially Sputtered $Pt_{1-x-y}M_xM_y$' (M, M' = Co, Ni, Mn, Fe) PEMFC Electrocatalysts," *J. Electrochem. Soc.*, **153** (10), A1835-A1846 (2006).

[71] K. Sieradzki, "Dealloying," in *Encyclopedia of Materials - Science and Technology*, 11 vols., K. H. Buschow, R. W. Cahn, M. C. Flemings, B. Ilschner, E. J. Kramer, and S. Mahajan, Eds. Elsevier, 2011, pp. 1984-1985.

[72] H. W. Pickering and P. J. Byrne, "On Preferential Anodic Dissolution of Alloys in the Low-Current Region and the Nature of the Critical Potential," *J. Electrochem. Soc.*, **118** (2), 209-215 (1971).

[73] K. Sieradzki, "Curvature Effects in Alloy Dissolution," *J. Electrochem. Soc.*, **140** (10), 2868-2872 (1993).

[74] H. W. Pickering, "Electrolytic Dissolution of Binary Alloys Containing a Noble Metal," *J. Electrochem. Soc.*, **114** (7), 698-706 (1967).

[75] H. W. Pickering, "The Surface Roughening of a Cu-Au Alloy during Electrolytic Dissolution," *J. Electrochem. Soc.*, **115** (7), 690-694 (1968).

[76] J. D. Fritz and H. W. Pickering, "Selective Anodic Dissolution of Cu-Au Alloys: TEM and Current Transient Study," *J. Electrochem. Soc.*, **138** (11), 3209-3218 (1991).

[77] J. S. Chen, M. Salmeron, and T. M. Devine, "Intergranular and transgranular stress corrosion cracking of Cu---30Au," *Corrosion Science*, **34** (12), 2071-2097 (1993).

[78] B. G. Ateya, G. Geh, A. H. Carim, and H. W. Pickering, "Selective Dissolution below the Critical Potential and Back Alloying in Copper-Gold Alloy," *J. Electrochem. Soc.*, **149** (2), B27-B33 (2002).

[79] X. Lu, E. Bischoff, R. Spolenak, and T. J. Balk, "Investigation of dealloying in Au-Ag thin films by quantitative electron probe microanalysis," *Scripta Materialia*, **56** (7), 557-560 (2007).

[80] X. Lu, T. J. Balk, R. Spolenak, and E. Arzt, "Dealloying of Au-Ag thin films with a composition gradient: Influence on morphology of nanoporous Au," *Thin Solid Films*, **515** (18), 7122-7126 (2007).

[81] J. Erlebacher and K. Sieradzki, "Pattern formation during dealloying," *Scripta Materialia*, **49** (10), 991-996 (2003).

[82] J. Rugolo, J. Erlebacher, and K. Sieradzki, "Length scales in alloy dissolution and measurement of absolute interfacial free energy," *Nat Mater*, **5** (12), 946-949 (2006).

[83] K. Wagner, S. R. Brankovic, N. Dimitrov, and K. Sieradzki, "Dealloying below the Critical Potential," *J. Electrochem. Soc.*, **144** (10), 3545-3555 (1997).

[84] J. Erlebacher, M. J. Aziz, A. Karma, N. Dimitrov, and K. Sieradzki, "Evolution of nanoporosity in dealloying," *Nature*, **410** (6827), 450-453 (2001).

[85] K. Sieradzki, N. Dimitrov, D. Movrin, C. McCall, N. Vasiljevic, and J. Erlebacher, "The Dealloying Critical Potential," *J. Electrochem. Soc.*, **149** (8), B370-B377 (2002).

[86] H. W. Pickering and P. J. Byrne, "Partial Currents During Anodic Dissolution of Cu-Zn Alloys at Constant Potential," *J. Electrochem. Soc.*, **116** (11), 1492-1496 (1969).

[87] D. E. Williams, R. C. Newman, Q. Song, and R. G. Kelly, "Passivity breakdown and pitting corrosion of binary alloys," *Nature*, **350** (6315), 216-219 (1991).

[88] R. Li and K. Sieradzki, "Ductile-brittle transition in random porous Au," *Physical Review Letters*, **68** (8), 1168 (1992).

[89] P. Mani, R. Srivastava, and P. Strasser, "Dealloyed binary PtM3 (M = Cu, Co, Ni) and ternary PtNi3M (M = Cu, Co, Fe, Cr) electrocatalysts for the oxygen reduction reaction: Performance in polymer electrolyte membrane fuel cells," *Journal of Power Sources*, **196** (2), 666-673 (2011).

[90] S. Koh and P. Strasser, "Dealloyed Pt Nanoparticle Fuel Cell Electrocatalysts: Stability and Aging Study of Catalyst Powders, Thin Films, and Inks," *J. Electrochem. Soc.*, **157** (4), B585-B591 (2010).

[91] P. Mani, R. Srivastava, and P. Strasser, "Dealloyed Pt–Cu Core–Shell Nanoparticle Electrocatalysts for Use in PEM Fuel Cell Cathodes," *The Journal of Physical Chemistry C*, **112** (7), 2770-2778 (2008).

[92] P. Strasser et al., "Lattice-strain control of the activity in dealloyed core–shell fuel cell catalysts," *Nat Chem*, **2** (6), 454-460 (2010).

[93] J. R. Dahn et al., "Economical Sputtering System To Produce Large-Size Composition-Spread Libraries Having Linear and Orthogonal Stoichiometry Variations," *Chemistry of Materials*, **14** (8), 3519-3523 (2002).

[94] A. Bonakdarpour, K. C. Hewitt, T. D. Hatchard, M. D. Fleischauer, and J. R. Dahn, "Combinatorial synthesis and rapid characterization of $Mo_{1-x}Sn_x$ ($0 \leq x \leq 1$) thin films," *Thin Solid Films*, **440** (1), 11-18 (2003).

[95] T. D. Hatchard et al., "The amorphous range in sputtered Si-Al-Sn films," *Thin Solid Films*, **443** (1), 144-150 (2003).

[96] D. A. R. Barkhouse, A. Bonakdarpour, M. Fleischauer, T. D. Hatchard, and J. R. Dahn, "A combinatorial sputtering method to prepare a wide range of A/B artificial superlattice structures on a single substrate," *Journal of Magnetism and Magnetic Materials*, **261** (3), 399-409 (2003).

[97] W. J. Walecki, F. Szondy, and M. M. Hilali, "Fast in-line surface topography metrology enabling stress calculation for solar cell manufacturing for throughput in excess of 2000 wafers per hour," *Measurement Science and Technology*, **19** (2), 025302 (2008).

[98] C. Giacovazzo et al., *Fundamentals of Crystallography*, 3rd ed. Oxford University Press, USA, 2011.

[99] R. Jenkins and R. Snyder, *Introduction to X-Ray Powder Diffractometry*, 1st ed. Wiley-Interscience, 1996.

[100] B. E. Warren, *X-Ray Diffraction*. Dover Publications, 1990.

[101] J. Goldstein et al., *Scanning Electron Microscopy and X-ray Microanalysis*, 3rd ed. 2003. Corr. 4th printing ed. Springer, 2003.

[102] V. R. Stamenkovic et al., "Changing the Activity of Electrocatalysts for Oxygen Reduction by Tuning the Surface Electronic Structure," *Angewandte Chemie*, **45** (18), 2897-2901 (2006).

[103] V. R. Stamenkovic et al., "Improved Oxygen Reduction Activity on $Pt_3Ni(111)$ via Increased Surface Site Availability," *Science*, **315** (5811), 493-497 (2007).

[104] H. A. Gasteiger and N. M. Markovic, "Just a Dream—or Future Reality?," *Science*, **324**, 48-49 (2009).

[105] A. Bard and L. R. Faulkner, *Electrochemical methods : fundamentals and applications*, 2nd ed. New York: Wiley, 2001.

[106] K. Oldham, *Fundamentals of electrochemical science*. San Diego: Academic Press, 1994.

[107] C. Brett, *Electrochemistry : principles, methods, and applications*. Oxford; New York: Oxford University Press, 1993.

[108] C. Hamann, *Electrochemistry*. Weinheim; New York: Wiley-VCH, 1998.

[109] D. R. Lide, *CRC Handbook of Chemistry and Physics, 86th Edition*, 86th ed. CRC Press, 2005.

[110] A. J. Bard and L. R. Faulkner, *Electrochemical Methods: Fundamentals and Applications*, 2nd ed. Wiley, 2000.

[111] C. M. A. Brett and A. M. O. Brett, *Electrochemistry: Principles, Methods, and Applications*, 1st ed. Oxford University Press, 1993.

[112] "Pine Research Instrumentation," *Pine Research Instrumentation*. [Online]. Available: http://www.pineinst.com/echem/productsubcats.asp?categoryID=3.

[113] F. C. Nart and W. Vielstich, "Chapter 21: Normalization of porous active surfaces," in *Handbook of Fuel Cells: Fundamentals, Technology, Applications*, vol. 2, W. Vielstich, A. Lamm, and H. A. Gasteiger, Eds. John Wiley & Sons, Ltd., 2003, pp. 302-315.

[114] T. J. Schmidt and H. A. Gasteiger, "Chapter 22: Rotating thin-film method for supported catalysts," in *Handbook of Fuel Cells: Fundamentals, Technology, Applications*, vol. 2, W. Vielstich, A. Lamm, and H. A. Gasteiger, Eds. John Wiley & Sons, Ltd., 2003, pp. 316-333.

[115] G. C. Liu et al., "RDE Measurements of ORR Activity of $Pt_{1-x}Ir_x$ ($0<x<0.3$) on High Surface Area NSTF-Coated Glassy Carbon Disks," *J. Electrochem. Soc.*, **157** (2), B207-B214 (2010).

[116] D. A. Stevens et al., "Assessing the Pt_{upd} Surface Area Stability of $Pt_{1-x}M_x$ (M = Re, Nb, Bi) Solid Solutions for Proton Exchange Membrane Fuel Cells," *J. Electrochem. Soc.*, **157** (5), B737-B743 (2010).

[117] A. Bonakdarpour, M. D. Fleischauer, M. J. Brett, and J. R. Dahn, "Columnar support structures for oxygen reduction electrocatalysts prepared by glancing angle deposition," *Applied Catalysis A: General*, **349** (1), 110-115 (2008).

[118] J. J. Steele and M. J. Brett, "Nanostructure engineering in porous columnar thin films: recent advances," *Journal of Materials Science: Materials in Electronics*, **18** (4), 367-379 (2006).

[119] K. Robbie, "Sculptured thin films and glancing angle deposition: Growth mechanics and applications," *Journal of Vacuum Science & Technology A: Vacuum, Surfaces, and Films*, **15** (3), 1460 (1997).

[120] W. Vielstich, "Chapter 14: Cyclic voltammetry," in *Handbook of Fuel Cells: Fundamentals, Technology, Applications*, vol. 2, W. Vielstich, A. Lamm, and H. A. Gasteiger, Eds. John Wiley & Sons, Ltd., 2003, pp. 153-162.

[121] G. C. Liu et al., "Oxygen Reduction Activity of Dealloyed $Pt_{1-x}Ni_x$ Catalysts," *Journal of Electrochemical Society*, **158** (8), B919-B926 (2011).

[122] D. van der Vliet, D. S. Strmcnik, C. Wang, V. R. Stamenkovic, N. M. Markovic, and M. T. M. Koper, "On the importance of correcting for the uncompensated Ohmic resistance in model experiments of the Oxygen Reduction Reaction," *Journal of Electroanalytical Chemistry*, **647** (1), 29-34 (2010).

[123] J. E. Harrar and I. Shain, "Electrode Potential Gradients and Cell Design in Controlled Potential Electrolysis Experiments.," *Analytical Chemistry*, **38** (9), 1148-1158 (1966).

[124] P. He and L. R. Faulkner, "Intelligent, automatic compensation of solution resistance," *Analytical Chemistry*, **58** (3), 517-523 (1986).

[125] J. Newman, "Resistance for Flow of Current to a Disk," *J. Electrochem. Soc.*, **113** (5), 501 (1966).

[126] A. Bonakdarpour et al., "Studies of Transition Metal Dissolution from Combinatorially Sputtered, Nanostructured $Pt_{1-x}M_x$ (M = Fe, Ni; $0 \leq x \leq 1$) Electrocatalysts for PEM Fuel Cells," *J. Electrochem. Soc.*, **152** (1), A61-A72 (2005).

[127] K. C. Neyerlin, R. Srivastava, C. Yu, and P. Strasser, "Electrochemical activity and stability of dealloyed Pt-Cu and Pt-Cu-Co electrocatalysts for the oxygen reduction reaction (ORR)," *Journal of Power Sources*, **186** (2), 261-267, (2009).

[128] D. A. Stevens et al., "A combined Rotating Disk Electrode/X-Ray Diffraction study of Co Dissolution from Pt1-xCox alloys," *Journal of Electrochemical Society*, **158** (8), B899-B904 (2008).

[129] E. Deltombe, N. de Zoubov, and M. Pourbaix, "Nickel," in *Atlas of Electrochemical Equilibria in Aqueous Solutions*, National Association of Corrosion, 1974, p. 330.

[130] A. Arvia and D. Posadas, "Nickel, Palladium, and Platinum," in *Standard Potentials in Aqueous Solution*, 1st ed., CRC Press, 1985, p. 321.

[131] K. F. Khaled, "Electrochemical behavior of nickel in nitric acid and its corrosion inhibition using some thiosemicarbazone derivatives," *Electrochimica Acta*, **55** (19), 5375-5383 (2010).

[132] K. Sieradzki, J. S. Kim, A. T. Cole, and R. C. Newman, "The Relationship Between Dealloying and Transgranular Stress-Corrosion Cracking of Cu-Zn and Cu-Al Alloys," *J. Electrochem. Soc.*, **134** (7), 1635-1639 (1987).

[133] M. K. Debe et al., "Extraordinary Oxygen Reduction Activity of Pt3Ni7," *J. Electrochem. Soc.*, **158** (8), B910-B918 (2011).

[134] A. Kongkanand, Z. Liu, I. Dutta and F. T. Wagner, "Electrochemical and Microstructural Evaluation of Aged Nanostructured Thin-Film Fuel Cell Electrocatalyst", *J. Electrochem. Soc.*, submitted